Multiscale ice and snow friction

Luca Canale

THÈSE DE DOCTORAT

de l'Université de recherche Paris Sciences et Lettres
PSL Research University

Préparée à l'Ecole Normale Supérieure de Paris

Friction multi-échelles sur la glace et la neige

École doctorale n°564

PHYSIQUE EN ÎLE DE FRANCE

Spécialité PHYSIQUE DE LA MATIÈRE MOLLE ET NANOSCIENCES

COMPOSITION DU JURY :

M Lydéric Bocquet
ENS Paris, Directeur de thèse

M Lionel Bureau
Univ. Grenoble-Alpes, Rapporteur

Mme Juliette Cayer- Barrioz
Ecole Centrale de Lyon, Examinatrice

M Christophe Clanet
Ecole Polytechnique, Invité

M Eric Clément
ESPCI, Invité

M Benjamin Cross
Univ. Grenoble-Alpes, Rapporteur

M Guillaume Ovarlez
Univ. de Bordeaux, Président

M Frederic Restagno
Univ. Paris XI, Examinateur

M Alessandro Siria
ENS Paris, Directeur de thèse

Soutenue par **Luca Canale**
le 12 Septembre 2019

Dirigée par **Lydéric Bocquet**
et par **Alessandro Siria**

ENS ÉCOLE NORMALE SUPÉRIEURE | PSL RESEARCH UNIVERSITY PARIS

Remerciements

Cette thèse m'a fait connaitre plein de personnes, ainsi je voudrais commencer par remercier tous ceux et celles qui m'ont aidé pendant ces trois années. Vous êtes nombreux et j'espère que je n'oublierai personne !

Naturellement, je voudrais remercier mes deux directeurs de thèse, Lydéric et Alessandro, qui m'ont encadré pendant ces trois années. Merci pour avoir toujours été bienveillants et positifs, malgré les difficultés rencontrées. Lydéric, ta force de volonté, ton dévouement et ton goût pour la science m'ont profondément marqué. Alessandro merci pour ta franchise, ton équilibre et ton support dans les moments plus difficiles. Avec Antoine (que je remercie aussi vivement !), vous m'avez appris comment aborder un problème expérimental et comment faire face aux difficultés. J'espère que je saurai reproduire cette démarche même si dans un autre contexte.

Un grand merci à Frédéric Restagno, pour m'avoir suivi et soutenu pendant ces trois années. Ton investissement, ta passion pour la science et ta rectitude sont vraiment une source d'inspiration pour moi.

Je voudrais maintenant remercier tous ceux qui ont travaillé avec moi, en commençant par Axel et Quentin. Merci pour votre engagement et votre enthousiasme, déjà rentrer dans un container à -20 avec tant d'envie est une chose rare, et en plus, une bonne partie de mes résultats sont dus à votre travail exemplaire. J'ai particulièrement apprécié de pouvoir travailler avec vous tout en discutant dans la bonne humeur. Merci Jean pour m'avoir accompagné sur les mesures AFM et m'avoir transmis un peu de ton savoir-faire. Merci aussi Pierre-Louis, pour ton énergie sans égal, ton investissement et ta générosité, j'espère que tu vas t'éclater dans ta nouvelle aventure autant qu'à l'ENS. Merci à Caroline et Christophe de m'avoir accueilli à l'X avec bienveillance et avoir fait tout le possible pour que je m'acclimate sur le plateau. Merci aussi à tous les doctorants du Ladhyx qui m'ont toujours invité pour un café ou un gâteau !

Cette thèse n'aurait pas été possible sans le travail des équipes administratives et techniques de l'ENS. Merci à Dounia, Nora, Annie, Benoit et Fabienne de m'avoir aidé dans les commandes, missions et autres avec le sourire ! Merci à Zaire, Yann et Frédéric pour le support informatique, merci (dans le désordre) à Jean-Michel, Arnaud, Allan, Mathieu, Georges, Jules, Richard, Laurent, Toufik (et tous ceux que j'ai oublié, désolé) de m'avoir aidé dans la conception et réalisation de mes manips. Merci à Aurélie, Jose et Michael de m'avoir accueilli en salle blanche et aidé pour des scans.

C'est au tour maintenant de remercier l'équipe Micromegas où j'ai passé la plupart de mon temps. Merci aux anciens : Eleonora, Elisa, Benoit, Vojtech, Hiroaki de m'avoir

accueilli avec bienveillance. Merci Adrien de m'avoir encadré en stage, mais surtout de m'avoir appris à faire du ski de fond et de la luge ! Merci Sophie de m'avoir nourri pendant ta thèse avec toute sorte de gâteaux et pâtisseries. Merci Laetitia d'apporter toujours de l'enthousiasme et du positif, quel que soit le projet ou la question. Merci Antoine d'avoir partagé tous les bonheurs du diapason (des sphères à Grenoble jusqu'aux interactions avec Guillaume et la plage à Tel Aviv), toujours avec le sourire. C'était un plaisir d'échanger et collaborer avec toi. Merci Timothée d'être toujours aussi disponible et m'avoir fait manger des sushis. Merci Nikita, de ta disponibilité et d'avoir tenté de m'apprendre le rock et m'avoir fait connaitre tous les morceaux de viande qui existent dans ce monde. Merci Anthony d'avoir toujours détruit tout ce qui était politiquement correct par tes blagues et ton ironie. Merci Théo de m'avoir accompagné à la piscine et de m'avoir appris des sains préceptes de vie : mes enfants feront 10 tractions tous les jours avant d'aller à l'école ! Merci Alice d'avoir cru que je jouais en National, pour un petit instant, j'y ai presque cru aussi ! Merci Amin pour ta bonne humeur et ton investissement dans l'équipe. J'adore nettoyer chez moi maintenant ! Merci Paul pour les croissants, bon courage pour la suite ! Merci à tous ceux qui étaient à Edimbourg, c'était la folie et j'espère qu'on se retrouvera dans un parking Carrefour, cette-fois ci à savourer du cognac plutôt que du whisky. Bref, j'espère qu'on restera tous en contact ! Promis, je vous réinviterai après mon cours de cuisine !

Je voudrais aussi remercier mes amis et amies qui m'ont aussi accompagné pendant ces trois ans. Une pensée spéciale aux autres thésards (Jérôme, William, Guillaume, Manu, Jacques, Mathilde, Ph et Marti) avec qui on a partagé les mêmes galères (ou pas, certains étant trop brillants). Merci aussi à ceux qui travaillaient et me rappelaient aussi qu'il y avait un autre monde dehors. Merci à Adelchi, Emile, Ph, Guigui, Jacques et Hadrien qui ont même renoncé à un jour de travail pour venir m'écouter blablater.

Merci à Golosino et au Libanais de la place Monge d'avoir illuminé mes mercredis et vendredis midi.

Un grand merci à mes parents, qui m'ont toujours poussé à faire mieux et m'ont toujours soutenu dans mes projets avec tendresse. J'espère avoir été en partie à la hauteur de leurs sacrifices. Merci à Elena et Teresa qui me supportent depuis presque trop longtemps.

Infine, grazie Franci per avermi voluto e saputo sempre ascoltare in questi tre anni, aver sopportato lamenti e brontolii e condiviso momenti di felicità. Senza di te non ce l'avrei mai fatta!

Contents

Introduction

Energy loss due to sliding friction is an old problem, that still has significant implications today. It has been estimated that 23% of the world's total energy consumption originates from tribological contacts [1]. Of that, 20% is used to overcome friction and 3% is used to remanufacture worn components. Standard fields of application involve transportation and power generation, but managing friction is also a necessity for moving extremely small components without wear in many technological devices. Indeed, the world could strongly benefit from the implementation of efficients tribological systems that reduce friction: it has been estimated that taking advantage of the new processes and technologies for friction reduction and wear protection could potentially reduce energy losses due to friction and wear by 40% in the long term (15 years)[1]. But while those efficient tribological systems are often taken for granted, many aspects of sliding friction are not well understood yet.

The first attempts to assess the rules of friction were undertaken by the pioneering works of Da Vinci and Amonton who gave a first rationalization of the macroscopical contact between two objects: they stated that the friction force is linear with the imposed normal load and independent of the contact area. In the last decades, the rise of new experimental devices such as atomic force microscopes and surface force apparati that allow for extremy small resolutions (up to few $\mathring{A}$ in space and piconewtons in force) has led to many advances in explaining how this macroscopical empirical observation is linked to the local contact mechanics.

Despite the relative slow fundamental understandings, a solution to reduce friction has been found early on, and consists in adding liquid lubricants between the solid frictioning interfaces. Indeed, the first findings of the application of oil or grease for heavy objects transportation date back to 2400BC. The corresponding physical theory developed later by Reynolds (1886) and based on the *hydrodynamics* of viscous fluids is still applied for designing many machineries. A distinct form of lubrication has been later introduced by Hardy [2] and coined *boundary lubrication*: the friction reduction is not given by the viscosity of the intermediate fluid but rather by its chemical composition. The lubricant molecules adsorb at the interface changing the actual contact surface, thereby enhancing slip. Perhaps the most striking feature of this phenomenom is that extremely thin adsorbed layers, in the nanometric scale, are sufficient to cause the lubricating effect.

Notwithstanding these findings, today many situations involving lubricating friction have yet to be rationalized, and ice and snow friction are two striking examples of this. They both have a long scientific history because of their broad relevance in a number of fields. The first report of leveraging sliding on ice comes from Scandinavia around 7000 B.C.

when carved rocks were used to transport heavy goods[3]. Today, 70% of the power consumption of an ice breaker ship is used to overcome ice friction [4]. The peculiarity of friction on ice and snow is its very low value. This fact, can be an advantage to transport high loads but also a danger, for example, for vehicles traffick in winter roads. Hence, understanding the mechanisms behind the low friction of ice and snow is fundamental in order to match the underlying needs of each of these different applications. A more mundane use of the low friction of ice and snow is for competitive sports such as speed skating or cross country skiing. Nonetheless, the need for faster speeds has been one of the main reasons to push scientific research on the topic and most of the available works are suited for sports interest (studies on speed skating [5, 6, 7], friction of polyethylene on ice and snow[8, 9, 10]). As a result, it is interesting to remark the steady increase of speed skating world records in the past century (see Fig.1-A).

Nevertheless, the fundamental mechanisms behind ice and snow friction are not understood yet. One blatant example to justify this statement comes from the actual methods used to reduce friction in cross country skiing: athletes put different waxes on their skis before each race. Depending on the temperature, humidity and track conditions, a huge number of waxes is available (see Fig.1-B): different wax combinations are tested in situ a few hours before the race, with the decision on which combinations to test coming from "empirical expertise". As a matter of fact, not only each federation has a waxing team for its athletes, but also, there was a huge wax gate after the 2014 Sochi Olympic games, when the norwegian wax chief was hold responsible for his team not winning a single medal!

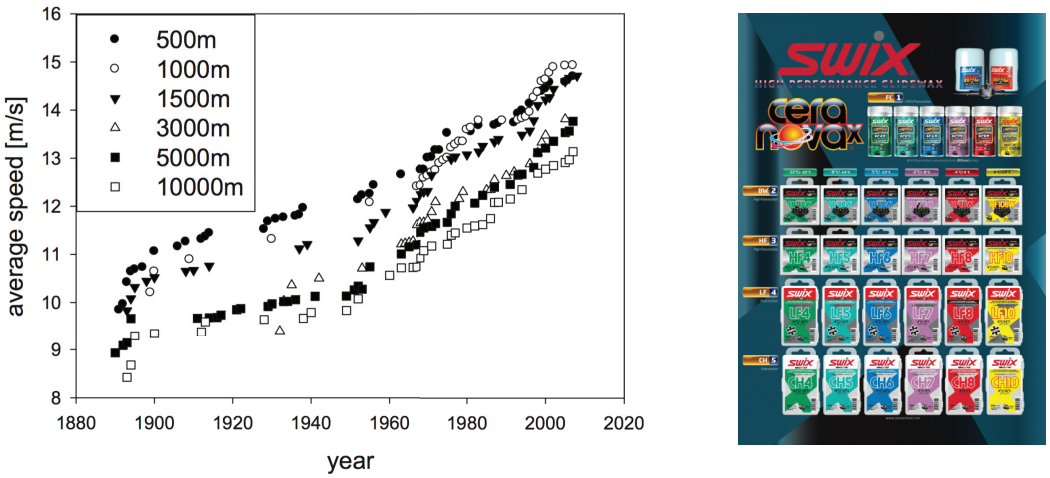

Figure 1: **(A)** World record evolution in ice skating taken from [11] **(B)**. Example of the different wax typologies available for a single wax brand.

In this thesis, we have evidenced some macroscopic features of ice and snow friction and linked them (for ice) to the microscopic interfacial properties. The manuscript is organized as follows:

Chapter 1: Macroscopic friction on ice and snow

In this Chapter, we present the main findings on ice and snow friction at the macro-level: a solid-like behavior with distinctive particularities such as a strong temperature and velocity dependence. While the existing literature consistently tends to attribute these specificities to the existence of a lubricating liquid layer, we show that not only experimental proof of this film is still lacking but also that the macroscopic findings do not allow for safely claiming the existence of such film. We illustrate these findings by presenting the results obtained about ice and snow friction with an in-house macroscopic tribometer.

Chapter 2: Bridging the gap between nano and macroscale, the Micromegascope

To understand ice and snow friction, it is necessary to have an instrument capable of measuring both macroscopic forces (typically in the mN) and nanoscale features. In this Chapter, we introduce a new such measuring apparatus called Micromegascope, based on the quartz tuning fork. This apparatus has an excellent mechanical stability coupled with an extremely large resolution (from hundreds of mN to μN). We stress that with this instrument it is possible to measure separately and quantitatively with unprecedented ease the dynamic response of solids and fluids via frequency modulation techniques. In particular, it is possible to determine the properties of a liquid film such as its thickness and viscosity under nanometric confinement, a capability necessary for the understanding of ice and snow friction.

Chapter 3: Applications to contact mechanics

In this Chapter, we test that the Micromegascope capabilities for contact mechanics purposes: we first tackle the question of the contact mechanics between two rough glass spheres. Then, we show that it is also possible to measure simultaneously and independently the normal and tangential mechanical response of a system under shear with the Micromegascope. Bearing in mind the original question of ice, we look at the frictional behaviour of a solid lubricant, polyethylene glycol, which might undergo a phase transition under shear at room temperature. We indeed measure a lubricating layer of few micrometers, which accounts for the extremely low friction coefficients measured. Interestingly, we find that the melting process generates very high viscosities, which we speculate might be due to a suspension of polymer fragments.

Chapter 4: Nanorheology of ice

Now, we come back to the original problem and probe the rheological properties of ice under shear with our tuning fork. We show that the observed macroscopical frictional properties are indeed due to a nanometric film of meltwater. Surprisingly, this liquid is not bare water but rather a complex viscoelastic fluid with a higher viscosity. In particular, friction is strongly correlated to that viscosity variations. Furthermore, we show that hydrophobic coatings reduce friction, hence that nanometric surface changes can strongly impact macroscopic ice friction. We speculate that the meltwater may be a supension of molten water and ice debris, whose properties are determined by the external factors (such as temperature and speed) and the surface properties.

Chapter 5: Outlooks on snow friction

Finally, after a brief sum up of the main conclusions, we address the differences between ice and snow and propose other mechanisms which might occur in snow friction. In particular, we focus on frictional processes which could arise from the granular structure of snow and suggest that capillary pumping might here play an important role that should be thoroughly quantified in future experiments.

Chapter 1

Macroscopic ice and snow friction

Contents

1.1 State of the art

1.1.1 Solid friction with extremely low friction coefficients

The main feature of ice and snow is their extremely small friction coefficient ($\mu \sim 0.01 - 0.08$) and this was corroborated by many experiments [12, 13, 14, 15, 9]. In practice, this specificity translates its slipperiness and is definetely the reason why winter sports could flourish: just imagine for one second how painful a cross-country ski race on sand would be. Now, a first important comment must be made about the definition itself of a friction coefficient. This definition makes sense when friction is ruled by the Amonton law which sets proportionality between the friction force F_T and the normal load F_N. The proportionality term is the friction coefficient. This is particularly true when macroscopic solid friction is involved. For ice and snow, a solid-like behaviour has been shown by macroscopical experiments [12, 13, 14, 15, 9]. Nonetheless, it is also important to note that in many other experiments people have found a dependence of the friction coefficient with the normal load: in ice on ice friction experiments, Oksanen et al have shown that the friction coefficient decreased with the normal load [13], while even more surprisingly, Akkok found that it depended upon the slider material: with a glass slider, they observed the same trend as Oksanen, but with aluminium or chrome/nickel sliders they had no dependency [16]. In these situations where there is no linear dependence between the friction force and the applied load, speaking about a friction coefficient can be misleading and induce to errors. Indeed, the literature about ice and snow friction must be evaluated carefully to avoid errors of interpretation or comparisons between phenomena that are intrinsically different.

Experimentally, the behavior of the friction coefficient is complex, depending strongly on temperature and velocity. Basically, the friction is high at low temperature, say below -20, then decreases towards a minimum (low) value in a temperature range between -20°C and -3°C and then increases again. The dependence on velocity may be split roughly in two different regimes [5, 20, 21]:

- for low temperatures, various experiments show consistently that the friction coefficient decays with velocity as $\mu \sim U^{\alpha}$ with $\alpha \approx -0.5$;
- for larger temperatures, close to the melting point, it increases with temperature as $\mu \sim U^{\alpha}$, with $\alpha \sim 0.5 - 1$, depending on materials and experiments. However one should emphasize that very large variations between experiments are usually reported.

We note that experimental measurements at low temperatures appear to be more reproducible and consistent for various sliding materials, as compared to friction measured at higher temperatures, for which experimental data varies greatly.

1.1.2 A liquid film at the origin of this behaviour?

The extreme slipperiness of ice and snow along with the other features that we listed above have traditionally been attributed to the presence of a tiny liquid film which would lubricate the frictional contact region and enhance slip. In this section, we will review the advances that have been made in trying to measure this liquid film and point towards two

contraddictory points: while there is strong consensus about its existence, experimental proof is still lacking.

Premelting film

Faraday has been the first to postulate that a quasi liquid like layer (QLL) or premelting film sits on top of ice at rest [17]. After 160 years of intense debate, many aspects of this QLL have been elucidated. In general, premelting starts from the surface and propagates towards the bulk as the surface layers are more weakly bound. An excellent summary of the physical and thermodynamic foundations of the QLL is given by Dash [18], but in in a more simple way, we can say that intuitively in order to lower its surface energy a crystal can wet its surface with its melt. Depending on the vapour pressure, the ice can either be covered by a thin film layer or a set of droplets. At equilibrium the Young relation sets the contact angle between the liquid and the solid $\gamma_{sv} = \gamma_{sl} + \gamma_{lv} \cdot \cos\theta$ [19] (see Fig.1.1-A). Traditionally, the main questions related to the premelting film concern the temperature at which premelting starts and the equilibrium thickness. A multitude of different experimental (x-ray[20], AFM [21], ellipsometry [22]...) and numerical (molecular dynamics [23], Monte Carlo [24]...) techniques have been used to try to answer these questions but the answers continue to be extremely dispersed (Fig.1.1-B). Nonetheless, we can say that the order of magnitude to keep in mind is -70°C to -13°C for the onset of premelting and 1 to 100nm for the thickness [19].

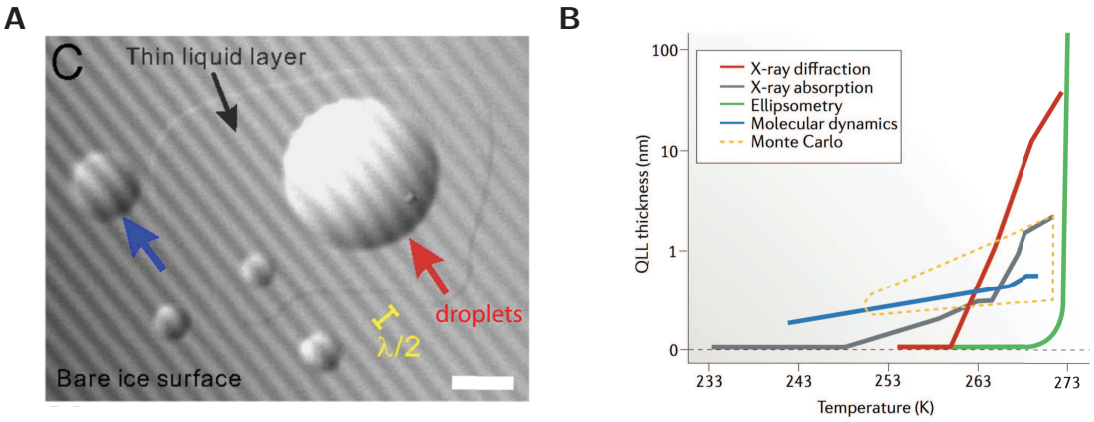

Figure 1.1: **(A)** Observation of different types of QLL [25].**(B)** Variations of the QLL thickness as a function of temperature [19].

Frictional heating

In contrast, the evolution of the premelting film when macroscopic sliding is involved is not very known. Historically, the fact that a larger film was growing under the slider was attributed to pressure melting. However, it has been later suggested that the pressure required to melt the ice was too high for this phenomenom to occur [26, 11]. Now, as in every frictional problem, it is important to keep in mind that the real contact area is much smaller than the apparent one because of the suface roughness and asperities, so one may argue that very locally, extremely high pressure could be achieved leading to pressure melting. The main issue with this argument is that in this case, there would also be

strong squeeze-out effects which would expulse the liquid and cause high wears and friction coefficients, but those are not observed experimentally. Furthermore,when looking at the water phase diagram, one realizes that pressure melting may occur only above -20°C, but one may ski below that limit. The pioneering works of Bowden [27, 12] and later Colbeck [28] have discarded pressure-melting mechanisms in ice friction and suggested frictional-melting: viscous dissipation generates heat which rises the temperature in the contact region up to the melting point, hereby creating a water lubricating film. The film thickness governs then the friction: when it is very small, rough contacts between asperities cause hard contacts and high friction coefficients; when it is too large, hydrodynamic friction becomes predominant and can cause an additional friction because of capillary effects. There, liquid bridges form between the ice and the slider, increasing the adhesion and resulting in an additional resistance to motion. The friction coefficient variations with temperature might be interpretated in this sense: at very low temperature, there is no melting and we have solid friction, then as the temperature increases, a lubricating film diminishes the friction coefficient. When the temperature is too high, capillary effects become predominant and the friction increases again. According to this understanding, researchers have come up with the idea that an optimal thickness should exist for which the friction is minimum [11, 28] (see Fig.1.2-A).

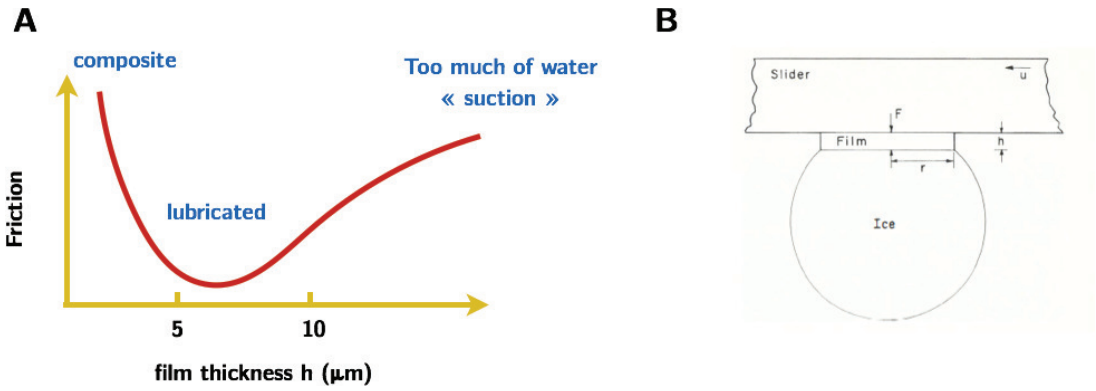

Figure 1.2: **(A)** Friction regimes believed to be relevant for ice friction. **(B)** Sketch of the contact between ice and the slider from [28].

This theory is also partially corroborated by the macroscopic dependences observed for the friction coefficient in ice. Indeed, one can balance the viscous heating produced by the flow with the energy associated with heat loss. Putting aside geometrical factors and following the notations of Fig.1.2-B, we find that:

$$r^2 h \times \eta \left(\frac{U}{h}\right)^2 \approx L_w \times rhU + \kappa r^2 \frac{\delta T_0}{\sqrt{\frac{\kappa}{\rho c_w} \times \frac{r}{U}}} \tag{1.1}$$

where κ,ρ, c_w are an effective thermal conductivity, density and heat capacity of the interface with excess temperature δT_0. η is the water viscosity and L_w the latent heat per volume. The latter term corresponds to the heat flux dissipated by thermal diffusion over the time-scale of the contact $t \sim r/U$.

This simple toy model gives two extreme cases depending on the dominant term in the right hand side: for low temperatures, which correspond also to small films, the heat loss

dominates and one finds that the film thickness scales like $h \sim U^{3/2}$. As $F_T \propto \eta \frac{U}{h}$ one retrieves a power law dependence for the friction force $F_T \propto U^{-1/2}$. In the opposite case, one finds that the film thickness scales like $h \sim \sqrt{U}$ and then $F_T \sim \sqrt{U}$. These predictions for the velocity dependences reproduce, at least qualitatively, the experimental observations for friction in both cold and warm temperature regimes. This model has been developed first by Evans [5], then some more sophisticated models have been put forward which take into account the number of contact points, the solid roughness or the ice softening [13, 29, 30].

Those models are all based on frictional heating and yield the same dependences. However, this relative consistency should not hide the fact that the arguments above all suffer from many uncontrolled assumptions and shortenings. They constitute an idealized view, which lacks strong experimental support. For instance, the contact between the ice and the slider is most probably mixed, with both lubricated regions and direct solid- solid contacts and a full description should take this composite nature into account. These models also put on the side other aspects which could be involved in the friction process such a squeeze flow at high loads or speeds, or capillary effects in the case of very large films. Often in the literature, this toy model is infered to even when it does not accurately reflect the data that it is associated with.

Actual measurement of the liquid film

In the literature, almost all the comments on the friction properties on ice are put in the perspective of a lubricating liquid film. Making such argument is a strong assumption and it would certainly need experimental proof. However, it is astonishing to discover that actually only two experimental measurements of the film thickness exist until now.

The first one has been done by Ambach and Mayr in 1981 [31]: they developed a capacitive probe to measure the dielectric constant of the contact region between a ski and snow. As water has a higher dielectric constant than dry snow, it is possible to retrieve the film thickness. They have found a film thickness in the range of the tens of microns, slightly varying with temperature or gliding speed. But at least two objections can be done about this experiment: the first one regards the calibration method. Indeed, they cover their probe with water and then use a stamp to impose the thickness from the top and measure the voltage. They repeat the same procedure with air instead of water and so obtain two curves from which they extrapolate the zero thickness as it was not possible to completely remove water or air from the interface. In fact, the extrapolated part corresponds exactly to the thicknesses measured with snow which makes the measurements extremely sensitive to this extrapolation. Second, in such a macroscopic setup, one may expect to have not only areas where a film separates the probe from snow but also other areas where air separates them. It is not clear how the average measurement coming from those two situations can be separated and analysed.

The second experiment was conducted by Strausky et al [32] and gave a completely different answer: there, they attempted to use fluorescent spectroscopy to try to measure the liquid film. They made an ice ring out of a solution of water and dye. When a transparent plexiglass (PMMA) slider glides over the rotating ring, the fluorescence in the contact zone is collected via an objective by a fiber and transferred to a spectrometer.

The intensity peak of a liquid layer or of solid ice does not occur at the same wavelength and it is possible to retrieve an estimate of the thickness from the intensity. But after calibration with a liquid solution, Strausky et al have not measured any liquid film with the PMMA slider at -2°C within their experimental resolution of 50nm! Nonetheless, the friction coefficient they found was still extremely low ($\mu \sim 0.03$). Finally, in a very recent experiment, Weber et al have also claimed that there is actually no ice melting. Instead, they attribute the frictional properties of ice to the mobility of surface ice molecules [14]. They assess that weakly bonded molecules diffuses over the surface in a rolling motion making ice smooth and slippery. This diffusion increases with temperature which leads to a decrease of the friction coefficient. Close to the melting point though, another mechanism would intervene: the ice deformation becomes plastic which leads to higher friction coefficients. While at high loads, indeed, marks can be seen on ice after skating, hence testifying for a plastic deformation, the diffusion theory lacks some arguments: for example, the authors claim that the ice shear strength is changing with temperature, but they do not explain the link with the molecules mobility.

To sum up, very contrasting results can be found in the literature, and at this stage, there is no direct proof in favor nor against the presence of a liquid film lubricating the contact. Hence, we first built a macroscopic tribometer, to have some initial insights about ice friction.

1.2 Experimental setup

1.2.1 The tribometer

Various experimental setups have been used to measure friction on ice and snow. A first idea that always comes to mind quite naturally is to conduct real life tests with skiers/skaters [6] or sliders models [12] for getting a first snapshot of the phenomenon at hand. But the main issue with this kind of measurements is that they lack experimental control (unpredictable human factor, uncontrolled trajectory of the slider, difficulty to monitor ice and air temperature...). For these reasons, many have rather developed linear [33, 34, 35, 10] and rotational devices where a small slider is guided through the track [29, 8, 32, 14] to allow control of most of the experimental variables (track, load, slider speed...). The advantage of a linear device is that the friction is always measured on fresh ice, which is not the case in a rotational one where the slider passes constantly over its marks. But on the other hand, a linear device would require a very long track to reach a steady state at high constant speeds. To have comparables speeds with data from literature, we conducted experiments on a rotational device designed ad-hoc to measure the friction force on ice and snow.

Pin on disk geometry

The setup of this experiment consists in a circular aluminium disk of radius 15cm, mounted on top of a servomotor from CNCservocontrol, allowing rotations up to 2000rpm. The disk has a 5cm depth and can be filled with ice or snow. On top of it, a slider is held by a metallic arm attached to a strain gauges Futek 1N.m^{-1} torque sensor and allowed to glide when the disk rotates (see Fig.1.3-A,B). We picked a slightly higher resolution than the needed one (measurements in general do not exceed 0.2N.m^{-1}) because such sensors

are extremely fragile and it could suffer from stronger torques. We measure directly the torque on the arm and retrieve the friction force on the slider. The slider has a semi-circular shape in order to ensure that the ring velocity is parallel to it and orthogonal to the holding arm. It is 4cm large, 10 cm long and 5mm thick (Fig.1.3-D). Masses can be screwed on top of it in order to change the normal load. A very important point was to ensure a constant contact between the slider and the track. Initially, although we took care of keeping as flat a track as possible, small unevenesses as well as a non perfect rotation of the motor would provoke small oscillations and avoid a constant contact, perturbing the measurement. To fix this, the connection between the slider and the arm is done via two pivoting links bound by two bicycle hubs which have almost zero friction (Fig.1.3-C). In this way, when the slider encounters some instability, say for example, a change of slope in the track, it will not jump but rather move forward or backward, being always in contact with the track.

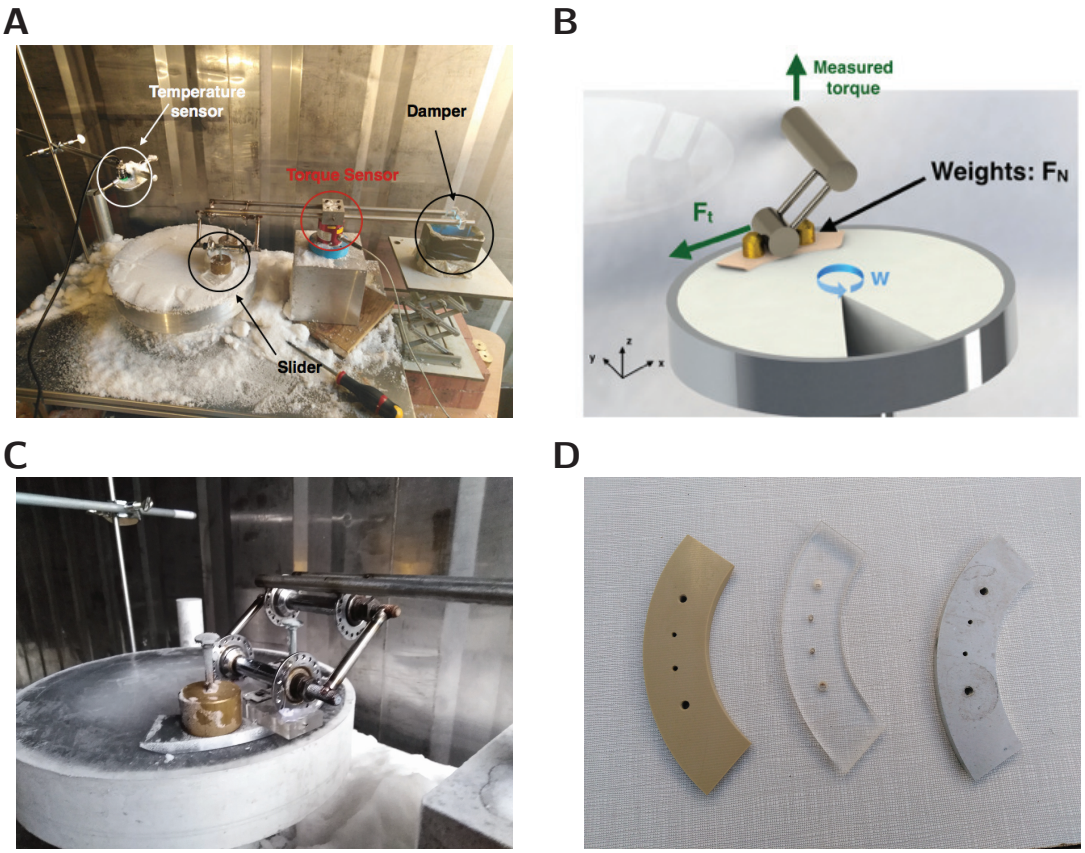

Figure 1.3: **(A)** Tribometer placed in the refrigerated container at the ecole Polytechnique. **(B)** Sketch of the setup. **(C)** Zoom on the system allowing to keep a constant contact on the track. **(D)** Examples of sliders made of different materials (from left to right: peek, pmma and aluminium).

Raw data

The data is acquired at a frequency of 150Hz and directly amplified with a Futek IPM650. An example of the raw data is shown in Fig.1.4-A : as it can be seen, the data is quite noisy and the noise increases with the motor angular speed. The reason is that the ring oscillations also increase with the angular speed. To verify that this was not detrimental to our measurements, we made a first calibration by measuring solid friction. We replaced the aluminium ring with a PolyMethylMethacrylate (PMMA) ring in order to measure PMMA on PMMA friction. In the case of solid friction, the friction force F_T is directly proportional to the normal load F_N. Therefore, we can define a friction coefficient $\mu = \frac{F_T}{F_N}$ which accounts for the tribological properties of two materials in frictional interaction. As shown, in Fig. 1.4-B, we find a friction coefficient which does not vary with the angular speed, as expected for such kind of friction. We also made measurements with a positive (in red) and negative (in blue) sense of rotation to push the verification further and we do not observe any significant difference. The value of $\mu \sim 0.16$ is in the expected order of magnitude, although slightly smaller than the friction coefficient for two clean PMMA surfaces (around 0.5 [36]). The reason is probably related to the surface preparation and the presence of some dirt. Indeed, in tribological measurements, the cleanness of the substrates is essential, as a few layers of contaminating molecules can strongly change the friction coefficient. But in this specific experiment, we were not interested in the value of the friction coefficient itself and hence, we disregarded the issue relating the substrate and slider cleanness. In conclusion, this experiment enabled us to validate the tribometer for the purpose of our experiment proving that the noise caused by dynamical instabilities was not harmful for our measurements.

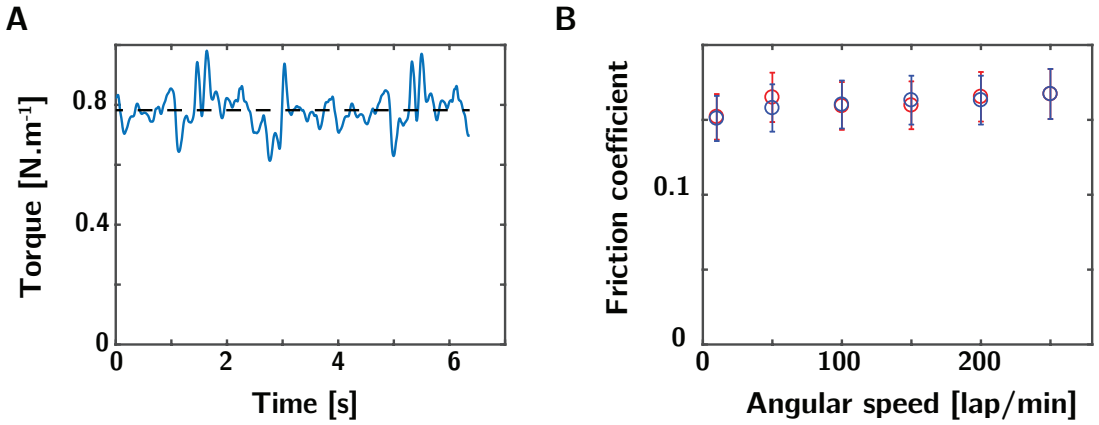

Figure 1.4: **(A)** Raw data for a measurement of a PMMA slider on a PMMA disk at the angular speed of 50 laps per minute. The dashed lines correspond to the average.**(B)** Friction coefficient (deduced from the measured torque, the arm length and the applied weight) variations with the angular speed for a slider of PMMA moving on a PMMA disk. The blue and red points correspond to clockwise and counter clockwise rotation of the disk respectively.

1.2.2 The cold chamber at the Ecole Polytechnique

The tribometer is placed in a refrigerated container at the ecole Polytechnique as shown in Fig. 1.5. In such container the temperature can be controlled between 0°C and -30 °C. Snow is also prepared in this container.

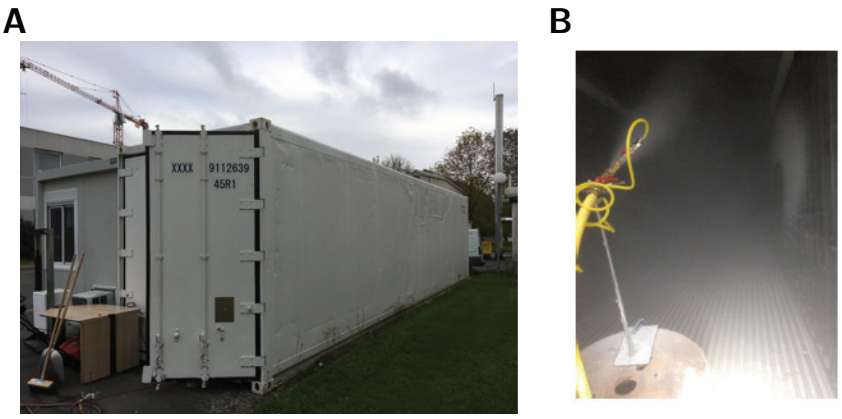

Figure 1.5: **(A)** Refrigerated container at the Ecole Polytechnique. **(B)** Water diatomisation to make snow.

Ice and snow preparation

Ice is made out of distilled water (Milli-Q IQ7003/05/10/15, resistivity 18MΩ.cm, pH ∼5.5), placed directly in the tribometer. The surface is then repeatedly shaved with a hot blade to even it. Snow is either collected during winter snowfalls (the ecole Polytechnique is on a hill, it happens) and stored in the container or directly fabricated in it. For the fabrication, we use a home made "snowmaking gun" made of an air-compressor, a pipe to mix water and air. When the mixture is propelled out of the nozzle, water is atomized. At -30°C, the small droplets freeze instantaneously and then grow while falling in the container. This procedure yields an artificial snow made of spherical ice particles of 100μm size (see Fig.1.6).

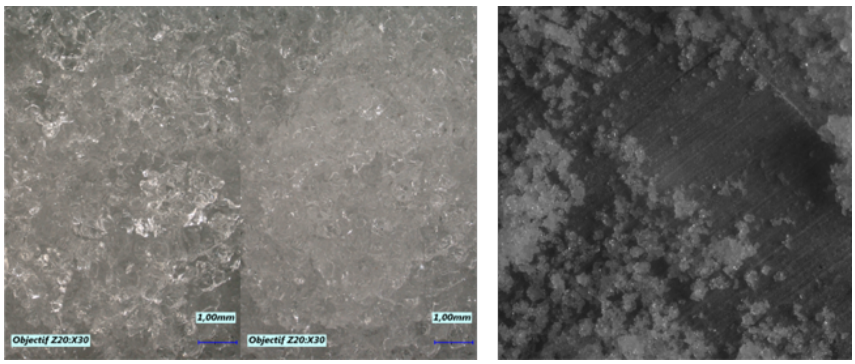

Figure 1.6: Different microscope images of snow prepared at different moments

1.3 Ice friction

1.3.1 Methodology

As previously explained, ice is made out of distilled water. Before each experiment (one set of measurements at different rotational speeds), we iron the track to flatten it as much as possible and then wait for it to refreeze completely. The ice temperature is monitored via an infrared sensor placed on top of the disk (see Fig.1.3-A). For ice, we do not observe a temporal change in the friction measurement which suggests that a stationary state is reached as soon as the measurement starts (Fig.1.7-A). For a given temperature, we make 5 consecutive measurements at a given angular speed or a given load before changing it. Each measurement consists in taking the mean torque over 5 laps. In the following, we will present the results as a function of the slider speed which is simply $U = R * \omega$ where R is the distance of the slider from the ring center (typically 10cm) and ω the angular speed. We varied it between 5 and 80 laps per minute. When performing measurements at different speeds, we always proceed from smaller to higher ones. Indeed, we observe an hysteresis in the opposite case (Fig.1.7-B): the friction found for U=0.055m.s^{-1} after one measurement at high speeds is consistently smaller than if we did the measurement at low speed directly. It is necessary to wait several minutes before we retrieve the inital measured value. This seems to suggests that a phase change is occuring at the surface (if it were a plastic deformation as suggested by Weber[14], the change in friction would be irriversible).

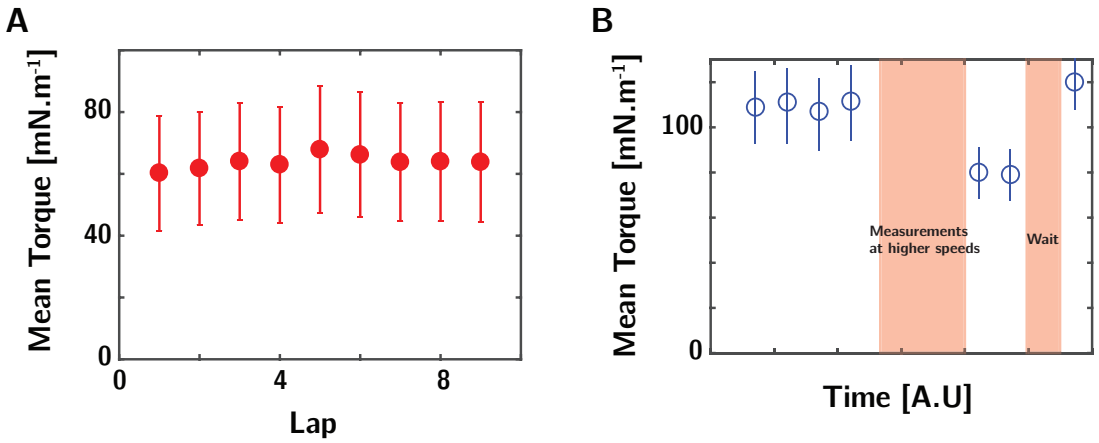

Figure 1.7: **(A)** Mean torque measured over each lap from the beginning of one measurement. **(B)** Evolution of the mean torque measured over several laps in different consecutive experiments for U=0.05m.s^{-1}.

1.3.2 A solid like behaviour with exotic features

Linear relation between tangential and normal forces

The first interesting feature to test is whether there is a linear relation between the normal load and the friction force on ice. As shown in Fig.1.8-A, we retrieve such relation with an extremely small friction coefficient $\mu \sim 0.02$ at T=-3°C. This value translates the well known slipperiness of ice as there is a factor 10 as compared to the friction coefficient

between two usual solids. In the following, as we observe a linear relation, we will define a friction coefficient and describe its variations as a function of various physical parameters.

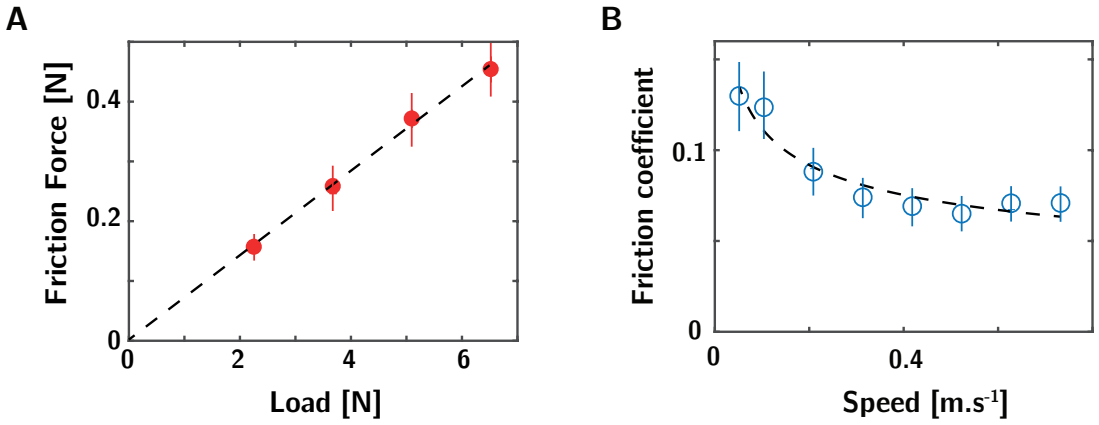

Figure 1.8: **(A)** Linear relation between the imposed normal load and the measured friction force on ice for a PMMA slider at T=-17°C. **(B)** Variations of the friction coefficient as a function of speed at T=-1.5°C for a slider of aluminium.

Velocity dependence

The first parameter which can be varied is the slider velocity. In this case, we set a constant load (F_N=5.5N) for all measurements. For a slider made of aluminium, we find a decrease of the friction coefficient as the velocity increases (Fig.1.8-B). This decrease is characterized by a weak powerlaw ($F_T \propto U^{-\alpha}$ with $\alpha \sim 0.3 - 0.5$). This result is not new and corroborates those of many other experiments [13, 16, 9]. However, it is important to note that at very high temperatures (close to the melting point), researchers have traditionally observed a regime where the friction force increases slightly with speed [9, 11]. We did not observe such regime even when we reached our highest temperature with measurements at -1°C. We could not indeed reach higher temperatures because we were limited by the container: it is difficult to control the temperature close to the melting point as it alternates continually periods of cooling and defrosting, making it complicated to have consistent measurements in the same conditions.

Temperature dependence

Next, we have investigated the implications of temperature for the friction coefficient. We have made a set of measurements at the speeds U=0.1m.s^{-1} and U=0.4m.s^{-1} while varying the temperature between -17°C and -1°C. We observe a U shape dependence with a minimal friction around T=-6°C (Fig.1.9). This shape has also been observed in other experiments, although the minimum friction has been found at different temperatures depending on the slider material. For example, De Koening with a steel speed-skater found a minimum friction around -8 °C [6], while Baurle with a polyethylene slider, found it at -3°C [9]. We have not been able to go below -20°C because controlling the container temperature was difficult below that limit. Nevertheless, with another setup (rheometer with a steel bead sliding on ice), Weber has been able to go down to -100 °C and has shown that temperature has a dramatic effect on the friction coefficient, finding a value in line with solid friction ($\mu \sim 0.5$)at very low temperature [14].

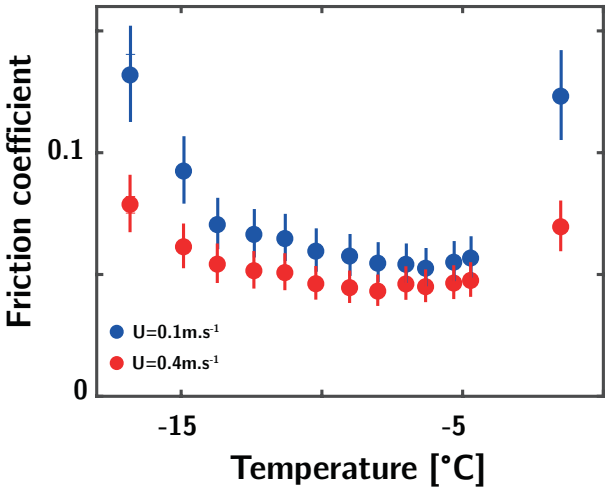

Figure 1.9: Evolution of the friction coefficient with temperature at two different speeds.

1.3.3 Thermal conductivity and hardness

To gain a better understanding of the mechanism at stake, we compared the frictional properties of three sliders made of different materials on ice : PMMA (plexiglass), peek and aluminium. While peek and plexiglass are thermal insulators, aluminium is an excellent thermal conductor (see Table 1.1). As these sliders were polished differently, we used glass paper to scratch them and obtain the same roughness for the three of them (around 1μm Ra). Indeed, although only few studies have looked at the effect of surface roughness on ice friction, these few ones suggest that smoother surfaces lead to lower friction [37, 35].

Parameter	Plexiglass	Peek	Aluminium
Thermal conductivity [W.m^{-1}.K^{-1}]	0.18	0.25	237
Specific heat [J.Kg^{-1}.K^{-1}]	1.5·10^3	1.5·10^3	900

Table 1.1: Thermal properties of the three sliders

In Figs.1.10A-B, we show the friction coefficient evolution for each slider in two extreme cases, ie at very low (-17°C) and very high (-1.5°C) temperature. We observe very different behaviors depending on the temperature and material, nonetheless some observations and rationalizations can be made: a first point is that at high temperature, the three sliders have the same weak powerlaw behavior. This is not the case at low temperatures, where the two insulators have an almost constant friction coefficient.

These results may seem quite contradictory: indeed, if we consider the metallic slider, then we are tempted to say that there is a velocity dependence and invoke the toy model that was described early on (section 1.1.2). But when comparing the peek and the plexiglass, one would be tempted to say that we have solid friction behavior as the velocity dependence seems weak enough to state that friction is independent of speed. In fact, this latter argument should be pushed further: in case of solid friction, then the friction force is simply equal to $F_T = \tau * A_c$ where τ is the the shear strength of the less resistant material and A_c the real contact area. Furthermore, the normal load is related to the contact area by $F_N = H \cdot A_c$ where H is the hardness of the softer material. Thus, the

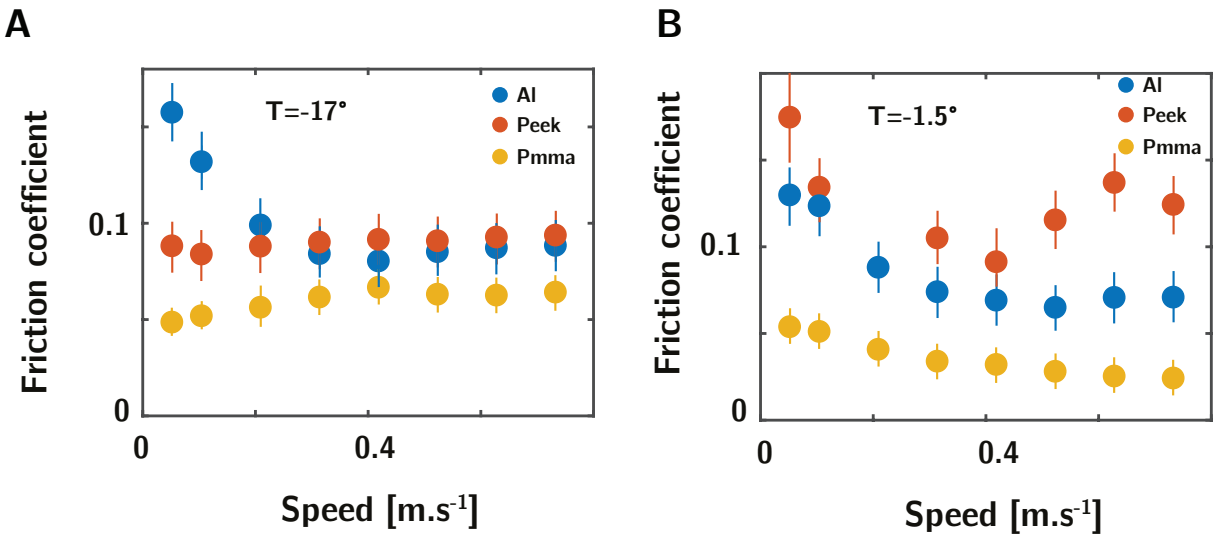

Figure 1.10: Variations of the friction coefficient as a function of speed for the three sliders at T=-17°C **(A)** and T=-1.5°C **(B)**.

friction force is proportional to the normal load and the friction coefficient is simply given by $\mu = \tau/H$. From Table 1.2 below [38, 39], the friction coefficients of peek, ice and plexiglass can be predicted at T=-17°C. We compare in Fig.1.11 the predicted $\mu = \tau/H$ to the experimental data for the friction of these materials on ice. They are compared to the measured ones in Fig.1.11. It is quite striking that the theoretical values for PMMA and peek are well above the measured ones. This means that the ice should yield plastically, and indeed ice has the lower hardness and yield strength. Still though, the theoretical friction coefficient for ice is higher than the measured one, and furthermore does not explain why we measure a difference between the two materials.

This indicates that the underlying mechanism must be more complicated: those contraddictory results underline that it is not possible to infer a microscoscopic behaviour directly from the macroscopic observations and that there is a fundamental need for a microscopic characterization of the interface.

Parameter	Plexiglass	Peek	ice
Hardness [MPa]	115	270	70
Shear strength [MPa]	40	55	7.8

Table 1.2: Mechanical properties of the thermal insulators and ice

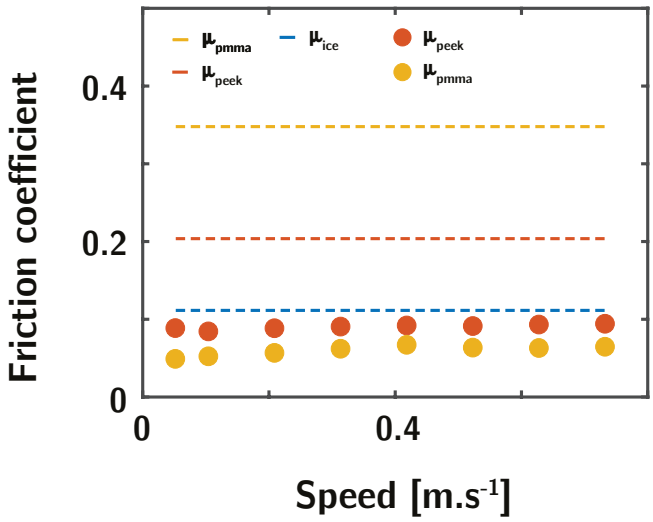

Figure 1.11: Measured friction coefficients (dots) along with the theorical values (dashed lines) for solid friction.

1.4 Snow friction

In this section, we will detail the experiments made on snow. Snow is an even more complex material as compared to ice: it is a multiscale assembly of small ice crystals or grains. Depending on the conditions (temperature, humidity, ageing) those grains have different shapes and properties (plates, dendrites, needles... hard facetted crystals versus wet grains) leading to very different kind of snows. In general, snow has a small resistance to plough, associated with a small macroscopic hardness ($H \sim 50kPa$ with large variations depending on the environmental conditions). This implies that the contact between the slider and snow is usually quite good, with a real contact area which is a large fraction of the apparent one. At the same time though, the local properties of the grains are those of ice and so differ from the macroscopic ones. Therefore, we should expect to retrieve some of the features of ice friction.

The specific interplay between the very different macroscopic and microscopic properties of snow makes snow friction even more complex to understand than ice friction. The goal of our measurements was indeed to try to compare what happens on snow to what we observed on ice, to highlight different properties. In addition, because of our collaboration with the French Biathlon federation, we wanted to quantify the effect of waxes on the friction force on snow and try to see if new solutions for reducing friction could be found.

1.4.1 Methodology and first observations

As for ice, we performed measurements at different speeds and normal loads for each tested temperature. Between each run, new snow is put on the tribometer and then flattened with a hammer and a scraper. Because we always add new snow, we did not observe any hysteresis depending on the order of the measurements (low to high speeds or the opposite). For each speed or normal load, we conducted 5 independent measurements. Contrarily to ice, we observed a decrease of the friction coefficient during the first laps (see Fig.1.12-A). Therefore, we waited for a longer time (typically at least 10 laps) before recording a measurement. The first observation is that once again friction is apparently 'solid-like': we have a linear relation between the normal load and the friction force and can define a friction coefficient μ. Its value, typically μ below 0.1 as for friction on ice, is much smaller than the friction coefficient between two standard solids (Fig.1.12-B). In the following, all the measurements presented are taken with a constant normal load $F_N = 5.5N$.

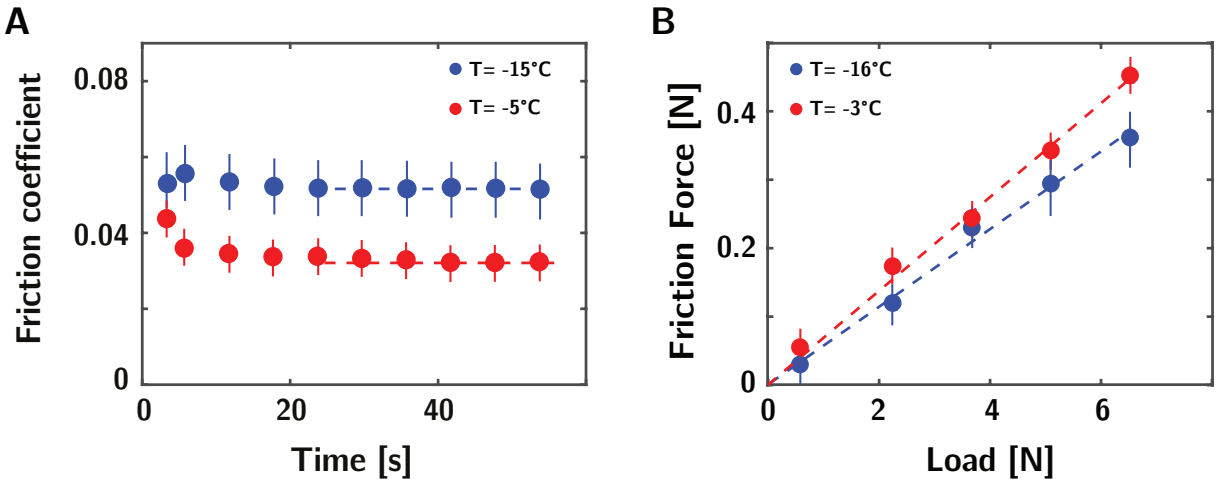

Figure 1.12: **(A)** Variations of the friction coefficient with time in two experiments at T=-15°C (blue) and T=-5°C (red) for a slider with a polythylene sole. **(B)** Linear relation between the normal load and the friction force for the PMMA slider.

1.4.2 Dependence on the snow type

Hard snows

For snow, we observe different behaviours depending on the type of snow. Hard snows are obtained by packing snow in the disk with weights (approximatively 40kg) on top of it for at least a day. Then, when the slider passes over such snow, we observe almost no trace on it as for ice. This means that ploughing is negligible and the contact is very similar to the one with ice. Indeed, for very hard snow, we observe the same speed dependences as for ice (Fig.1.13. We have a power law behaviour both at low and high temperatures. Interestingly, this behaviour remains valid for all the tested materials even at -15°C (Fig.1.13-A). At -3°C though, peek is the more slippery material. This difference is quite strong (almost a 50% decrease at low speeds) but vanishes at low temperatures (-15°C).

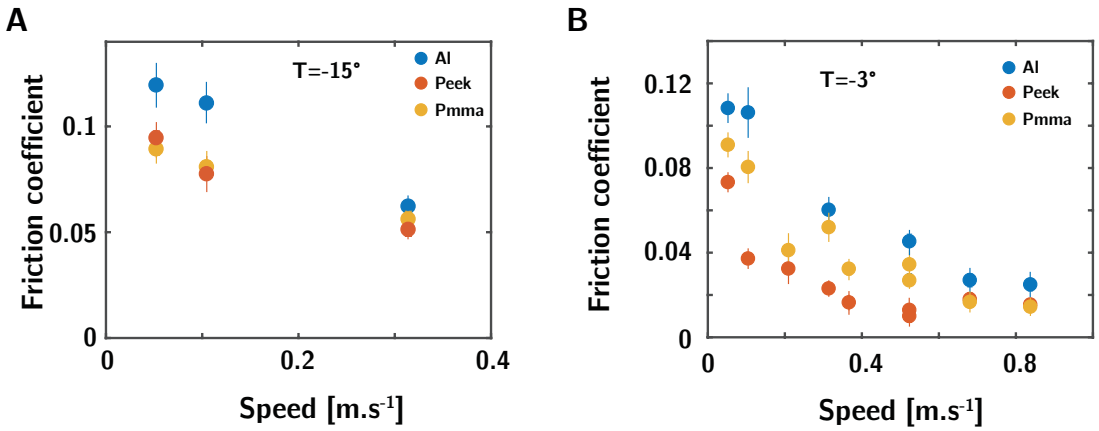

Figure 1.13: Friction variations for the three sliders at T=-15°C **(A)** and -3°C **(B)**.

Soft snows

As a reminder, soft snow correponds to snow taken directly after fabrication, without any compaction. For such snows, the trends are extremely dispersed (see Figs.1.14-B,C). The order of magnitude is still in the same range as for hard snows. However, there is not a clear trend emerging: if for peek, the friction coefficient seems to have a non monotonous shape as a function of velocity, for plexiglass, it seems rather constant and for aluminium, it seems to overall decrease with speed. Furthermore, the different curves crosses each other at different points, making it difficult to decide which material would be the most slippery. This also highlights the strong variability of friction on snow and might be due to the joint effect of different physical mechanisms. We will come back on this aspect later. For the moment we can nonetheless say that for these snows, ploughing is an important phenomenon as we observe that the slider systematically leaves a noticeable trace on the track (typically 1cm deep, see Fig. 1.14-A). In a first approximation, this can be calculated as follows: when the slider moves forward, the work that the slider has to pay corresponds to the work needed to compact the snow below. If we consider that the snow is compacted over the slider length l by the height h, then the compaction force F_{comp} corresponds to $F_{comp} \cdot l = F_N \cdot h$ where F_N is the normal force on the ski. Therefore, the friction coefficient is the geometrical ratio $\mu = h/l$. For our slider, which is 10cm long,

we observe typical ploughs of few mm on soft snows, which yields a ploughing friction coefficient of few 10^{-2}. Therefore, this contribution to friction should be also taken into account.

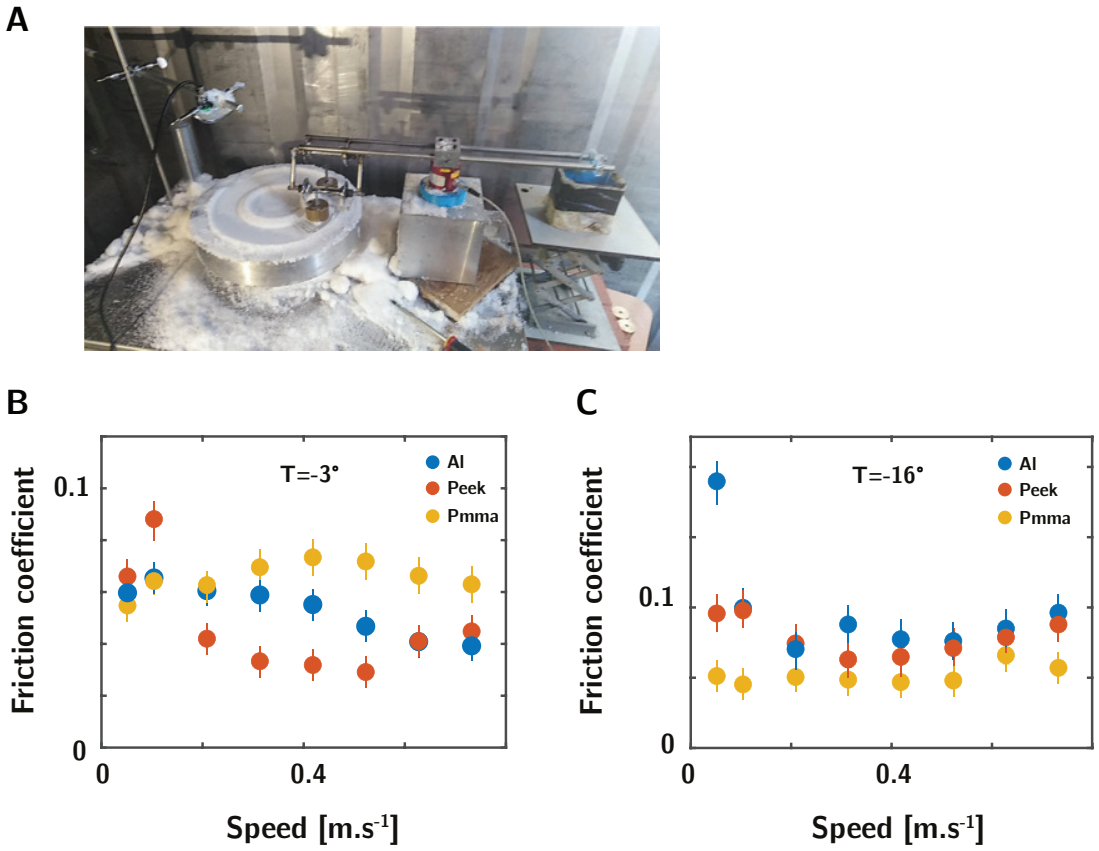

Figure 1.14: **(A)** Snapshot of the setup with soft snow: we observe a strong ploughing. **(B-C)** Friction variations for the three sliders at T=-3°C **(B)** and -16°C **(C)**.

1.4.3 Wax effects

Waxes and sliders preparation

Next, we tested the effect of wax on the friction force. In general, very few informations are available on the chemistry of ski waxes [40]. The basic constituents of all ski waxes are petrolatum (petroleum jelly) varieties of paraffin waxes, microwaxes and Fischer Tropsch wax. These different waxes consist of hydrocarbon molecules with different molecular weights which determine their hardness. For example, microwax is significantly harder than the other waxes. While every industrial wax is composed of these waxes, their precise composition of course remains confidential. It is also known that the most expensive waxes contain fluor additives to make the sole hydrophobic as this is supposed to reduce friction. On the applicative side, as skis polyethylene sole is porous, a first layer of melted wax is spread over the ski base for impregnating the surface. Then, the base is buffed in order to create a smooth surface. Before a race, multiple layers of different waxes are applied on top of each other following the same procedure. Further investigations on the wax effects on the wetting properties of the sole are given in Annexe B.

Since so much importance is given to waxes in cross country skiing races, we were keen to quantify their effect: does it affect the friction coefficient by 10% or 200%? To this end, we prepared sliders on which we glued a polythylene ski sole on the bottom (Fig.1.15-A). Some of the sliders are treated with two waxes: both chosen Vola race waxes containing High Fluor especially suited for competitions (Fig.1.15-B). These two waxes are respectively advised for very low temperatures below -10°C (blue one) and high temperatures (above -2°C).

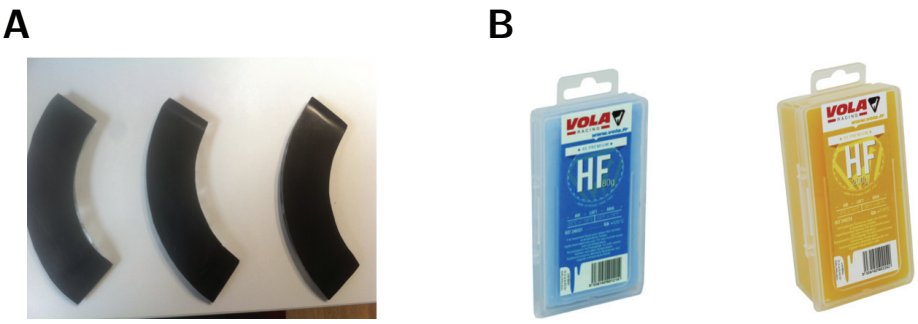

Figure 1.15: **(A)** Sliders with a polyethylene sole. **(B)** High and low temperature wax that we used for the experiments.

Friction reduction

As shown below in Fig.1.16-A, waxing has indeed a dramatic impact on friction: when varying the temperature, we observed that at U=0.1 m.s^{-1} the friction coefficient is consistently smaller for the waxed sliders than for the bare ones. Furthermore, depending on the temperature, this effect can be truly huge, with the friction coefficient being reduced by as much as 50% at T=-10°C. Note however that this effect does not increase at higher temperatures. This is somewhat surprising since the hydrophobic effect would be expected to be stronger when the snow is more wet, hence closer to the melting point. The effect of the appropriate wax is more nuanced though: for a given temperature, we measured only a very small difference between the effects of waxes advised at low and high temperature. It seems that the wax for low temperatures (cyan points) gives indeed a minimal friction at a lower temperature than the wax for high high temperatures (dark blue points) but more measurements with higher accuracy would be needed to quantify this effect properly.

Development of new low friction solutions

Even if from these measurements it is complicated to exhaustively explain the origin of the observed frictional properties on snow, the tribometer remains a very easy plug and play tool for quantitative friction tests. Therefore, it is an excellent and efficient instrument that could be used to develop and test new waxes suited for ski races in the future. For the moment, we have developed a new material which, when applied on the ski sole, yields even lower fricion coefficients at higher temperatures than the tested waxes Fig.1.16-B. This new coating is still at a test stage since its efficiency must also be verified at high speeds and after a long race. We will not discuss further this material in the present document.

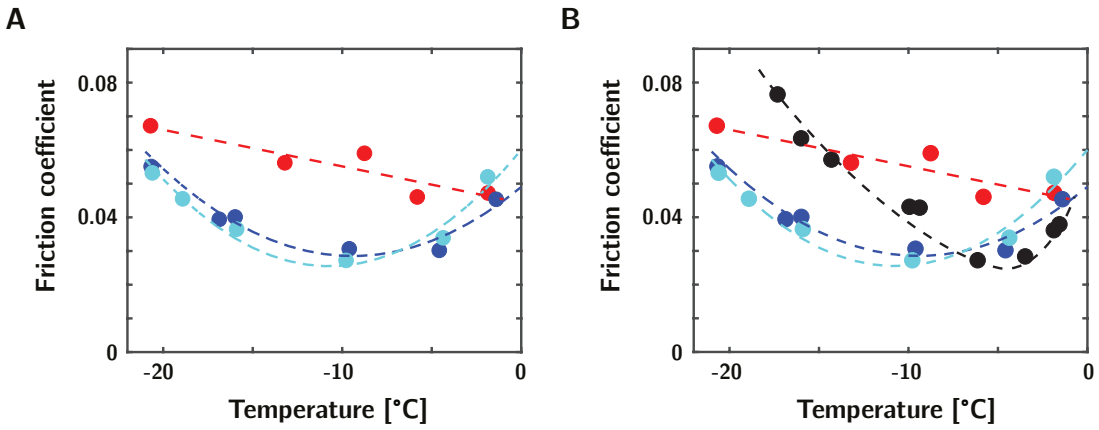

Figure 1.16: **(A)** Comparison at U=0.1m.s^{-1} of the frictional properties between a standard ski slider (red) and waxed sliders for cold (cyan) and hot(blue) temperatures **(B)** Development of a new coating (black) which exhibits lower friction coefficients close to the meting point.

1.5 Conclusion

In this chapter, we have presented a macroscopic tribometer which allows to characterize properly the macroscopic frictional properties of different materials on ice and snow.

For ice, we observe an apparent solid friction with some peculiar features such as the existence of a temperature for which the friction is minimal and a dependence with the sliding speed. We also showed that from these findings it is not possible to understand easily the underlying microscopic mechanisms. While most of the scientific community attributes the frictional behavior of ice to the existence of a liquid film, some of our observations may also be attributed to a solid contact between asperities. Therefore, there is a fundamental need to explore the nanoscale to more satisfactorily understand what is happening at the interface between ice and the slider. In the following, we will focus on ice friction and present a new instrument developed to study the ice interface at the nanoscale during friction.

The situation for snow is more complicated since we observed that phenomena at different scales couple together in friction: macroscopically, the snow can be soft and can plough under the slider pressure; the grains can be entrained and roll on each other and finally, locally, if the grains are more compact we may also have the same interaction between the grain and the slider as the one for ice. Somehow, the different waxes reflect the interplay between all these scales: indeed, as the wax adjusts both the hardness of the ski base to the snow as well as the hydrophobicity, it suggests a specific interplay between elasticity, wear and hydrodynamics. We will come back later on snow friction to give some insights about the possible phenomena occuring such as granular and capillary effects.

Chapter 2

Measuring forces at the nanoscale: the Micromegascope

Contents

In the last few decades, the interest towards the properties of matter at the nano-scale has increasingly drawn attention. To explore effects at those scales, a strong force sensistivity is required. Two main classes of instruments have been developed for such scope: atomic force microscopes (AFM) and surface force apparati (SFA). In this chapter, we will briefly discuss the working principles of these systems and explain why they are not suited for measuring the mechanical properties of ice. Instead, we introduce a new apparatus, the Micromegascope, which allows more versatility. We will stress that its nanometric sensitivity coupled with its strong mechanical stability make it a perfect tool for measuring the local properties of the interface in ice friction.

2.1 Standard AFMs and SFAs

2.1.1 AFM

Static force measurements

Atomic force microscopy was introduced for the first time by Binnig in 1986 [41] and is based on the optical measurement of the deflection of a cantilever. A sharp tip is attached to the cantilever free end and its interaction with a substrate causes the deflection. A laser is reflected on the cantilever tip and the signal is acquired by a photodiode (see Fig.2.1-A). In a static measurement, the interaction force F_{int} is then directly proportional to the deflection δl by $F_{int} = k * \delta l$ where k is the stiffness of the cantilever. Measuring forces at the nanoscale involves two requirements: a very small spatial resolution and a high force resolution. In practice, spatial resolution is resolved by the tip apex (tenths of nanometers). To measure forces of the order of pN, as the maximal displacement detection is of the order of the nanometer, one must use flexible cantilevers with stiffnesses in the order of hundredths of N.m^{-1}. As the stiffness is set by the geometrical proportions of the cantilever, standard AFMs have a typical length of the order of 100μm. The corresponding stiffnesses lie from 0.01 to 10 N.m^{-1}. With such dimensions, it is possible to achieve nanometric resolution and perform topographic surface scans or measure forces.

In a typical approach-retract experiment, the tip approaches the substrate until it reaches contact. During the approach, the cantilever deflection increase until the gradient of the attractive forces (typically electrostatic, Vand der Waals...) becomes higher than the cantilever stiffness. At that point, an instability occurs causing a jump in the force profile (snap-in). Very close to the surface and on the surface, the deflection changes because the forces become repulsive. During the retract, we generally have an hysteresis because of adhesive forces which retain the tip in contact with the substrate. It is in the last part of the approach (when the repulsive forces become predominant) or during the retract, that it is possible to make a topographic scan of the surface (contact mode in Fig.2.1-B). Indeed, in that region, the force is linear with displacement and no instability can occur. Therefore, when the cantilever scans the substrate surface, a feedback loop allows to maintain the interaction constant by adjusting the cantilever distance from the substrate, thereby retrieving the substrate topography. As at the end of the retract phase, another mechanical instability can occur because of the breakdown of adhesive

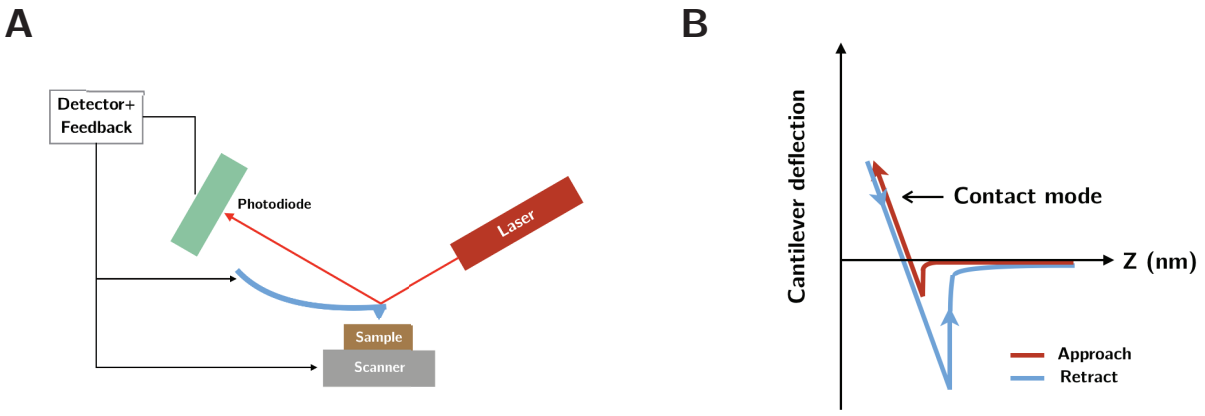

Figure 2.1: **(A)** Sketch of the AFM principle and example of an approach-retract curve **(B)**.

forces, scans are usually performed at the end of the approach.

Dynamic measurements

AFMs can be used in a dynamic mode: in such case, the cantilever is excited mechanically to vibrate. The main advantage of this technique is that it allows to scan fragile substrates that could otherwise be damaged by the contact with the tip. For dynamic measurements, there are two different techniques: amplitude modulation (AM) and frequency modulation (FM). Both AM and FM techniques were initially meant for non contact mode (far from the substrate), but different technical adjustments [42] such as the use of stiff tuning forks instead of soft cantilevers enable the use of these techniques also in contact mode today.

In AM-AFM, the cantilever is driven by the mechanical excitation at a frequency f_{driv} which is close to the resonant frequency f_0 of the cantilever [43]. When the tip is close to the substrate, interaction forces modify the amplitude and the phase of the oscillation with respect to the excitation. In a scan, the topography is directly extracted from these informations. Typically, the height is adjusted to keep the oscillation constant. From these changes, it is also possible to retrieve quantitative informations about the forces at stake. The calculation is nevertheless tedious and the amplitude change is not instantaneous but occurs on the time scale of the transient regime of oscillations which scales typically like $\tau \sim Q/f_0$ where Q is the quality factor of the cantilever (see definition below). For cantilevers, the quality factor is between 100 and 1000 in the air, limiting the measurement speed.

In FM, the cantilever is controlled via a positive feedback on the external driving force making it vibrate at a constant amplitude A and at its resonant frequency f_0. The response time is given here by the time necessary to measure the change in the resonant frequency, which is simply proportional to $1/f_0$ [44]. Therefore, this technique is much faster and in fact, the interaction forces can be deduced more easily. During a scan, the distance from the substrate is adjusted in order to keep a constant frequency shift, which corresponds to constant force gradient. We use it for our measurements and we

will further develop its characteristics later.

Unconventional oscillators

Other types of AFMs have been developed to probe nanoscale properties. In particular, quartz tuning forks have been introduced in 1995 by Karrai [45]. Because they are excellent oscillators (Q∼15000) and have an excellent mechanical stability (stiffness k ∼10s kN.m^{-1}), they are used in different home made setups for hard condensed matter or in surface science measurements [46, 47, 48], generally in frequency modulation mode. For example, atomic resolution has been achieved with such resonators [49] and the desire to achieve ultra high force sensitivities has pushed to the development of alternative kinds of probes such as nanowires and nanotubes [50, 51] or suspendend membranes made of graphene and other 2D materials[52], leading to sensitivities up to the zepto-Newton[53]. These probes however present important constraints due to the challenges in detection and working conditions, and cannot be easily used out of some specific laboratory applications.

2.1.2 SFA

Because of the cantilever size, with a conventional AFM, it is not possible to achieve nanometric resolution with macroscopic probes. For such scope, surface force apparati have been developed even early in the late 60's[54]. They consist in two smooth perpendicular cylinders which are brought close to each other by a positioning piezo element fixed to one cylinder. The other cylinder is attached to a spring to measure the interacting force between the surfaces. The force is computed by measuring the difference between the imposed confinement and the actual one [55]. For such scope, various techniques have been developed such as interferometric [56] or capacitives [57, 58] methods that achieve typically sub nanometric accuracy (1 Å) up to sub-molecular level [59, 60, 61]. If in the beginning, SFA were meant to measure equilibrium surface forces [55], nowadays several updates have led to the possibility to probing frictional properties [62, 63, 64] or measuring the rheological properties of confined liquids [65]. Recently, dynamic SFA also enabled hydrodynamic force measurements superimposed on the static response [65]. Nonetheless, the deflection of mechanical parts along with the imperative need of confinement distance measurement brings experimental complexity and imposes constraints on the surface design and environment.

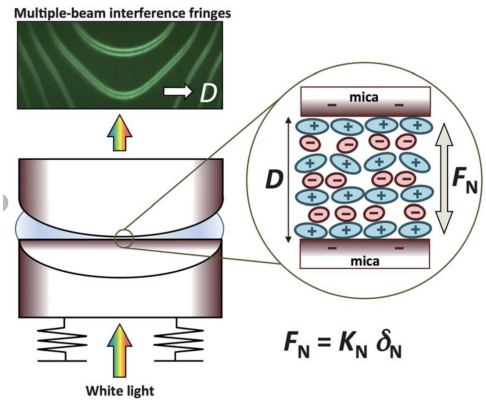

Figure 2.2: Schematic of a surface force apparatus taken from [66].

2.2 The Micromegascope

As discussed early in the chapter, with an AFM, one is limited by the size/mass of the sample glued to the cantilever, which should be small in order to allow the cantilever oscillation, while SFA lacks versatility. On the contrary, to measure the local properties of the interface in ice friction, it is important to have a force apparatus which combines nanoscopic and macroscopic sensitivity with versatility. With this aim in mind, we have developed a new atomic sensor, the Micromegascope, based on a centimetric tuning fork as sketched in Fig.2.3. In the group, quartz tuning forks have alread been used for AFM and force measurement purposes, for example to investigate the capillary freezing of ionic liquids [67] or the origin of shear thickening [68]. Our new tuning fork is directly inspired by the quartz one but is almost twenty times bigger.

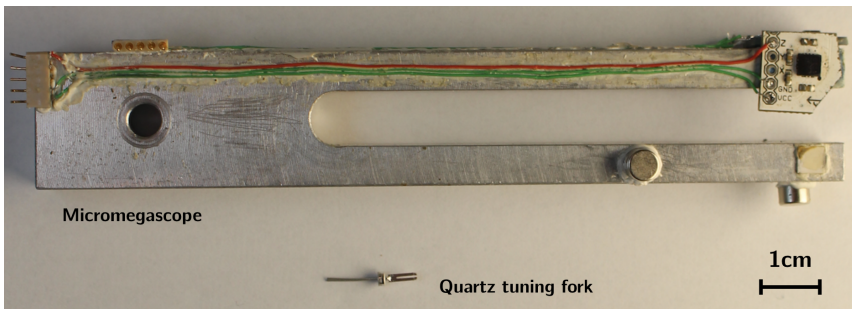

Figure 2.3: Photograph of a quartz tuning fork and an example of Micromegascope.

2.2.1 Mechanical properties

Resonant frequencies

The tuning fork has several resonant frequencies (or modes) which correpond to symmetrical and antisymmetrical motion of the two prongs. For a cantilever, the theoretical expression of the n-th mode is given by:

$$2\pi f_n = (n + \pi/2)\,\frac{t}{L^2}\left(\frac{E}{\rho}\right)^{1/2} \tag{2.1}$$

where E and ρ are the material Young modulus and volumetricic mass, and t and L the cantilever thickness and length. In general, it is possible to adjust the tuning fork design in order to obtain the desired resonant frequencies: indeed, a numerical finite element simulation (we used Comsol) allows to deduce directly the resonant frequencies from the tuning fork characteristics.

In this work, we only used the first two antisymmetric modes in two perpendicular directions as sketched in Fig.2.4. When a probe is glued on the tuning fork prong, one mode oscillation leads to a motion parallel to the surface, while the other mode to a perpendicular one. In the following, we will refer to them as the tangential and normal mode, respectively.

Stiffness and added mass

The tuning fork resonance can be related to the spring constant (or stiffness) K along the direction of motion and the effective mass m_{eff} by:

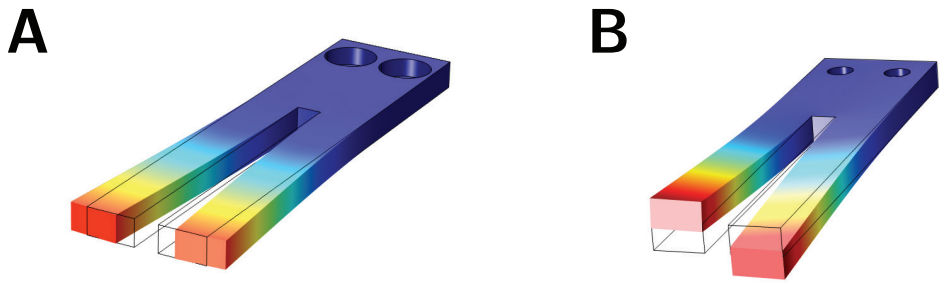

Figure 2.4: Sketch of the two dynamical modes of the tuning fork used for this thesis to have a probe oscillation tangential to the substrate **(A)** and perpendicular to the substrate **(B)**.

$$f_0 = \frac{1}{2\pi}\sqrt{K/m_{eff}} \tag{2.2}$$

Both parameters can be computed theoretically. The stiffness can be derived by considering the motion of two cantilevers fixed in parallel with the dimensions of the tuning fork prongs. Indeed, the stiffness of one cantilever is given by $K = \frac{Ew}{4}\left(\frac{t}{l}\right)^3$ where E is the Young modulus, w the width, l the length and t the thickness. Then for two cantilevers, we just need to multiply this expression by 2. For a centimetric tuning fork such as our, the theoretical value lies in the order of hundreds of kN.m^{-1}. As compared to standard AFMs and SFAs, the Micromegascope has therefore an extremely large stiffness, which allows an excellent mechanical stability. Indeed, even in configurations where strong attractive or repulsive interactions occur (like when the tip is immersed in a liquid or indented into a solid surface), the tip position will be perfectly controlled. The theoretical value for the first mode along one direction of the added mass is m_{eff}=0.2427M where M is the mass of one prong. This value is computed directly from the theoretical value of the resonant frequency and stiffness [45]. For the Micromegascope, it lies in the order of tenths of grams. Because of this large effective mass, it is possible to glue rather big probes (millimetric beads for example) to the Micromegascope without perturbing its motion.

For more precision, we have experimentally calibrated the stiffness and the effective mass in each direction of motion by gluing additional masses to the tip and measuring the corresponding frequency shift in the resonance. The additional mass δm leads to a new resonant frequency given by:

$$f_0' = \sqrt{\frac{K}{m_{eff} + \delta m}} \tag{2.3}$$

For small masses δm compared to the effective mass m_{eff}, we can linearize the expression above and obtain:

$$f_0' = f_0 - f_0\frac{\delta m}{2m_{eff}} \tag{2.4}$$

Therefore, we have a linear relation between the frequency shift $\delta f = f_0' - f_0$ and the original resonance $f_0 = \sqrt{K/m_{eff}}/2/\pi$. Rearranging the terms, we can show that the slope is directly proportional to the tuning fork stiffness:

$$\boxed{\delta f = -\frac{2\pi^2 f_0^3}{K}\delta m} \tag{2.5}$$

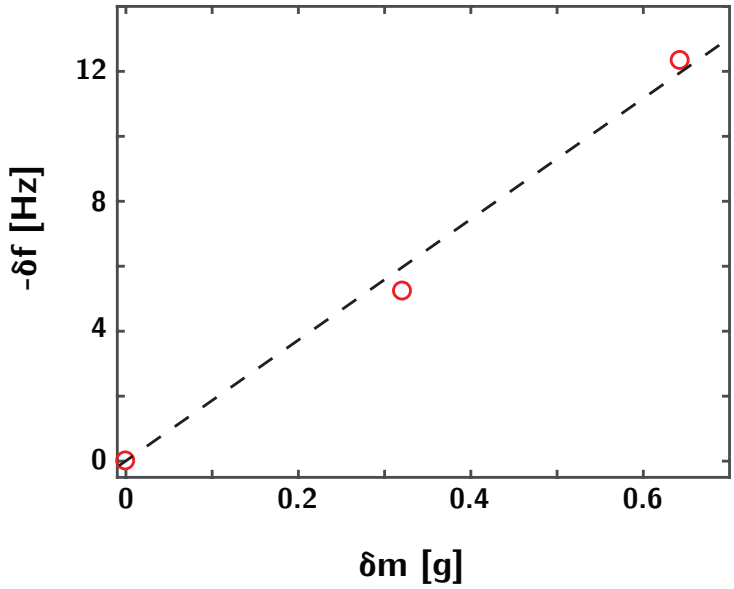

Figure 2.5: Linear relation between the frequency shift in the resonant frequency and the added mass to the tuning fork prong.

The added mass is then computed from the resonant frequency and the found stiffness. For example, we obtain for the tuning fork normal mode a stiffness of 890 kN.m^{-1} and an effective mass of 25g.

Lorentzian behaviour at the resonance

Close to the resonance, the tuning fork can be modeled accurately as a one dimensional harmonic resonator. In the absence of interacting forces, the tuning fork dynamics are given by:

$$m_{eff}\ddot{x} + \gamma\dot{x} + Kx = F_{drive} \tag{2.6}$$

where m_{eff} [kg] is the equivalent oscillating mass, $\gamma[N.s.m^{-1}]$ is a viscous damping due to the intrinsic dissipation in the air, $K[N.m^{-1}]$ is the spring constant of the tuning fork and F_{drive} the external forcing. Non dimensionalizing this equation leads to:

$$\boxed{\ddot{x} + \frac{\omega_0}{Q}\dot{x} + \omega_0^2 x = \frac{F_{drive}}{m_{eff}}} \tag{2.7}$$

with the natural frequency of the tuning fork:

$$\omega_0 = \sqrt{\frac{K}{m_{eff}}} \tag{2.8}$$

and the quality factor:

$$Q = \frac{m_{eff} \times \omega_0}{\gamma} \tag{2.9}$$

We can solve Eq. 2.7 under the hypothesis of oscillatory motion: the sinusoidal force $\underline{F}_{drive}(t) = F_{drive} \cdot e^{i\omega t}$ leads to a sinusoidal amplitude $\underline{a}(t) = A \cdot e^{i\omega t + \phi}$. Accordingly, we can write that :

$$\boxed{A(\omega) = \frac{F_{\text{drive}}}{m_{\text{eff}}} \cdot \frac{1}{\sqrt{\left(\omega_0^2 - \omega^2\right)^2 + \omega^2\omega_0^2/Q^2}}} \tag{2.10}$$

while the phase lag ϕ between the driving force and the tuning fork oscillation reads:

$$\boxed{\tan(\phi(\omega)) = -\frac{\omega\omega_0}{Q\left(\omega_0^2 - \omega^2\right)}} \tag{2.11}$$

Finally, the amplitude at the resonance is defined by:

$$\boxed{A_0 = \frac{F_{\text{drive}}Q}{K}} \tag{2.12}$$

Near the resonance, we can write that $\delta = \omega - \omega_0 << \omega_0$ and $Q >> 1$, and we can linearize 2.11 to obtain the following relation for ϕ:

$$\boxed{\phi \sim -\frac{2\left(\omega - \omega_0\right)Q}{\omega_0}} \tag{2.13}$$

We show in Fig.2.6 the measured amplitude and phase shift for a tuning fork oscillating near the resonance, along with the fits of Eqs 2.10 and 2.11.

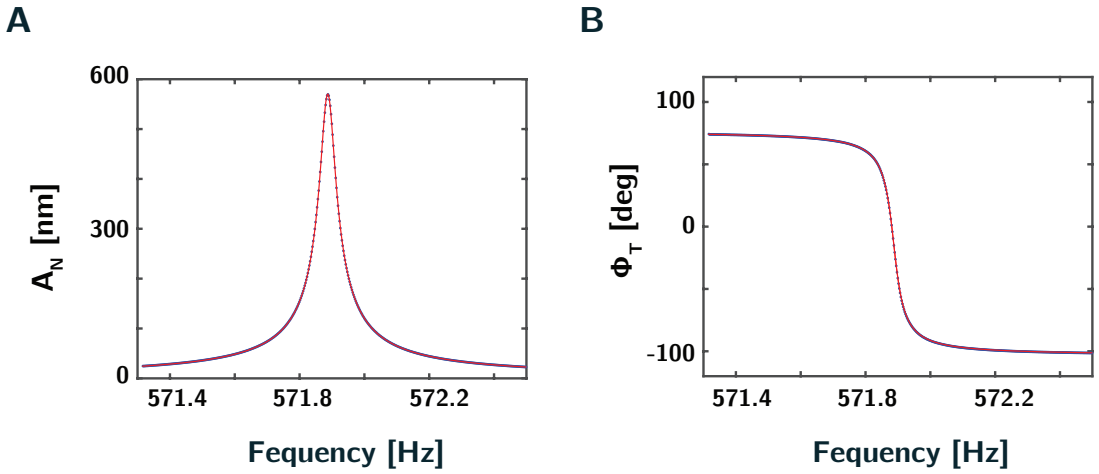

Figure 2.6: Mesured amplitude **(A)** and phase shift **(B)** as a function of frequency close to the resonance for the tangential mode. In blue, the measured data while in red we show the fitted theoretical curves for a quality factor of 11700 and resonant frequency of 571.9Hz.

Quality factor and force sensitivity

The quality factor determines the sharpness of the resonance curve as it is related to the half width peak $\delta\omega$ by: $Q = \omega_0/\delta\omega$. Indeed, higher quality factors mean higher frequency sensitivities. The quality factor also plays an important role in the force sensitivity: when the system is in interaction, additional forces F will lead to a change in the oscillation amplitude that should be detectable. A fundamental parameter is therefore, $s = A/F$ which quantifies the effect of the force on the oscillation amplitude. Far from the resonance, s=1/K, but at the resonance, s=Q/K, hence a higher Q will lead to a bigger amplitude which can be detected more easily. On the other hand, a high quality factor means also a long transient regime as the equilibrium time of the oscillator τ is given by $\tau \sim Q/\omega_0$. Depending on the experiment and technique (AM/FM), a higher or lower quality factor might be advisable. For example, to achieve atomic resolution specific techniques that reduce the quality factors are adopted [69]. In our system, typically, the quality factor varies between 100 and 10 000 depending on a number of parameters such as the considered mode, the mass glued on the tuning fork (probe+detection system), or the external environement (air, vacuum, temperature).

2.2.2 Measurements of conservative and dissipative force fields

When the probe glued on the tuning fork is submitted to an external force field, the resonance of the tuning fork will be modified. Here we show how it is possible to retrieve from the shift in the resonant frequency and the change in the amplitude, quantitative information about the conservative and dissipative force fields at stake. The system can be modeled as sketched in Fig.2.7: the tuning fork tip is interacting with a conservative force field F_c and a dissipative one F_d. As the system is oscillating at a given amplitude A, it is often useful to define the complex mechanical impedance: $Z^* = \frac{F_c+F_d}{A} = Z' + iZ''$. This notation is especially convenient when measuring the properties of materials for which one needs to compare both the elastic and the dissipative mechanical impedances.

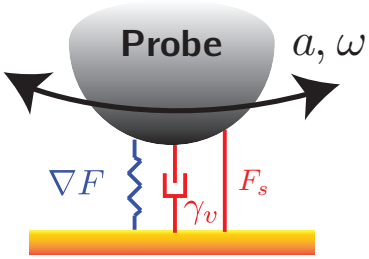

Figure 2.7: Sketch of the probe in interaction with an external force field.

Conservative force field

A conservative force field characterizes elastic forces which are in phase with the displacement. It can be described by a force gradient or by the real part of the mechanical impedance:

$$\boxed{F_c = \nabla F \cdot X} \tag{2.14}$$

$$Z' = F_c/A \tag{2.15}$$

Dissipative force field

A dissipative force field characterizes forces which are in opposition of phase with the displacement. It can be described by the imaginary part of the mechanical impedance and includes both solid frictional forces and viscous ones :

(2.16)

$$\boxed{F_d = -(\gamma_v \dot{x} + F_s \frac{\dot{x}}{x})} \tag{2.17}$$

$$Z'' = \frac{F_d}{A} \tag{2.18}$$

Modified equations of motion

The new equation of motion now reads:

$$m_{eff}\ddot{x} + \gamma_v \dot{x} + Kx = F_{drive} + F_c + F_d \tag{2.19}$$

Using the same method, we can rewrite it in the sinusoidal forced regime as:

$$-\omega^2 \underline{X} + i\omega \frac{\gamma_+ \gamma_v}{m_{\text{eff}}} \underline{X} + \omega_0^2 \left(1 - \frac{\nabla F}{K}\right)^2 \underline{X} = \frac{1}{m_{\text{eff}}} \left(F_{\text{drive}} - \frac{4F_S}{\pi}\right) \tag{2.20}$$

The factor $\frac{\pi}{4}$ comes from the first term of the Fourier expansion of the solid friction force which is a square signal. We disregard the higher terms here because the cutoff frequency of the lock-in amplifier filters higher modes. This equation corresponds to a new Lorentzian, with a new resonance frequency given by:

$$\omega_0{}' = \omega_0 \cdot \sqrt{1 + \frac{\nabla F}{K}} \tag{2.21}$$

In general, $\nabla F << K$, therefore, we can relate directly the frequency shift $\delta\omega = \omega_0' - \omega_0$ to the conservative force field by:

$$\boxed{\nabla F = Z' = 2K \cdot \frac{\delta\omega}{\omega_0}} \tag{2.22}$$

The viscous like force leads to a decrease in the quality factor at the resonance as $Q' = \omega_0' \cdot m_{\text{eff}} / (\gamma + \gamma_v)$. Typically, $\delta\omega/\omega_0 \sim 10^{-2}$, thus one can safely approximate $Q' \sim \omega_0 \cdot m_{\text{eff}} / (\gamma + \gamma_v)$ and from there, we can retrieve that :

$$\gamma_v = \frac{K}{\omega_0} \left(\frac{1}{Q'} - \frac{1}{Q}\right) \tag{2.23}$$

Hence, at the resonance, the dissipative friction force reads:

$$\boxed{F_v = K \left(\frac{1}{Q'} - \frac{1}{Q}\right) \cdot A} \tag{2.24}$$

To account for both solid and viscous friction, one can measure the additional force F_{ext} that has to be provided to keep a constant amplitude A_0 under interaction and at rest. In that case, we obtain from Eqs.2.7-2.19 that:

$$\frac{\omega_0^2 A_0}{Q} = F_d + F_{drive} = F^0_{drive} \tag{2.25}$$

From this, we deduce that F_d is simply related to the increase in the driving force as:

$$F_d = F_{drive} - F^0_{drive} \approx \gamma_v \dot{x} + \frac{4F_s}{\pi} \tag{2.26}$$

Now, replacing F_{drive} and F^0_{drive} by $C \cdot E$ and $C \cdot E_0$, one finally obtains that we can directly measure the global dissipative force (viscous or not) by measuring the additional excitation voltage necessary to keep the amplitude constant accordingly to:

$$\boxed{Z'' = \frac{F_\mathrm{d}}{A_0} = \frac{K}{Q}\left(\frac{E}{E_0} - 1\right)} \tag{2.27}$$

2.3 AFM setup with the Micromegascope

In this section, we describe the workflow necessary to prepare the tuning fork for an experiment as well as the data acquisition procedure.

2.3.1 Tuning fork preparation

To prepare the tuning fork, we have first to glue the accelerometers and magnets on it. To do so, we use different glues depending on the environment: for experiments at room temperature, standard loctite is sufficient, whereas when the setup is placed in a cold environment, we need a glue resistent to cold and humidity. We use a Torr Seal vacuum expoxy which is very well suited to such need. If we use standard loctite, we see after a couple of hours in cold a weakening of the adhesive bonds and in particular, the quality factor of the tuning fork is strongly impacted. The probe is also glued with the same glue.

Oscillation detection

The oscillation amplitude is measured via one or two accelerometers glued on the tuning fork prong. We used three different accelerometers with different sensitivities depending on the amplitude we want to impose. Indeed, when the tuning fork is oscillating, the acceleration a is directly proportional to the amplitude of oscillation A by $a = A \times \omega^2$ where ω is the angular frequency ($\omega = 2\pi f$). For the ice experiment, we wanted to have large amplitudes of oscillation laterally and small ones perpendicularly, therefore we used respectively the ADXL 377 (200g resolution with g the gravitational force equivalent) and the ADXL 335 (3g resolution) from Analog. For the dry friction experiments, we wanted to achieve extremely small amplitudes and we used the LIS344ALHTR from STMicroelectronics (2g resolution). These accelerometers in general have a 50Hz bandwidth, therefore, we changed the capacitance mounted in the circuit to ensure a full signal at the resonant frequencies of the tuning fork. The signal measured is given in mV/g. To check that the calibration is correct, the first easy way is to verify that the saturation voltage corresponds to the maximal resolution of the accelerometer (for example, the ADXL has a resolution of 330mV/g, hence it should saturate at 990mV). For more precision, the accelerometers are calibrated by interferometry.

Mechanical excitation

To excite the tuning fork, we can use two different methods: the first one is to glue a piezo dither on the prong and excite the tuning fork mechanically at the desired frequency. The second one is to glue a magnet on the prong and use a coil to generate a sinusoidal forcing. The advantage of using a coil is that it enables to reach higher amplitudes of oscillation, required for example in the case of the ice friction experiments. On the other hand, having a magnet and a coil induces a constant force that should be taken into account. This results in a positive frequency shift which increases with the excitation voltage (of the order of hundreds of mHz). In the case of the ice friction experiments, this contribution was negligeable as compared to the frequency shift due to the physical interaction.

In both cases, the force acting on the prong can be modeled as $F = F_0 sin(\omega t) = C \times Esin(\omega t)$ where $Esin(\omega t)$ is the voltage provided to the piezo/coil. The force transduction between the excitation voltage E_0 and the resulting forcing F is also calibrated at the beginning of each experiment, and can be retrieved from the quality factor and the amplitude A_0 at the resonance, as:

$$C = \frac{F_{\text{drive}}}{E_0} = \frac{KA_0}{QE_0} \tag{2.28}$$

Probe preparation

For AFM experiments, we use sharp tungsten tips [70] that are etched from a tungsten wire using the so-called double lamellae dropoff etching [71], which takes advantage of small ring electrodes (Fig.2.8-A). A drop of 1 M NaOH in each ring creates an electrolytic cell in which the tungsten wire is etched. After an etching time of less than 5 minutes, the wire becomes so thin that the lower portion falls down under its weight, thus opening the circuit and stopping the etching process automatically. The upper part of the tip has a radius typically smaller than 50 nm (see Fig.2.8-B).

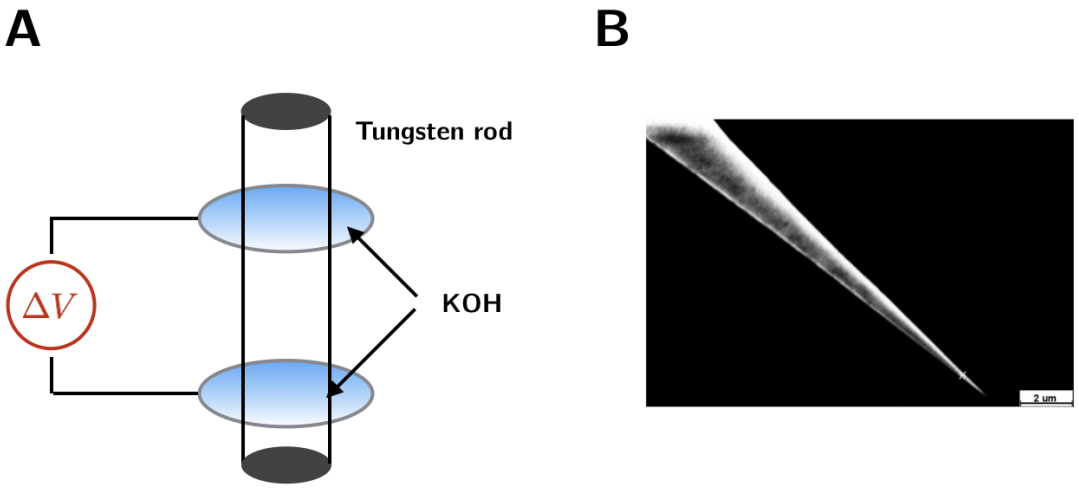

Figure 2.8: **(A)** Sketch of the etching setup. **(B)** SEM image of a tungsten tip.

Global AFM setup

The tuning fork is fixed directly to a Thorlabs XY stage with micrometric precision (Figs.2.9-A,B). We use it in particular to position the magnets glued on the tuning fork in front of the corresponding exciting coils. Coarse positioning motors allow the substrate to approach the tip in the Z direction. We use inertial MechOnics motors. They can move with a step size of 30 nm over a total course of 2 cm. For AFM scans, we use a piezoelectric scanner from Piezosystem Jena. The scanner allows smooth displacements of up to 8 μm in the 3 spatial directions, with a precision below 100 pm. For friction experiments, we use a linear piezoelectric actuator from Physik Instrumente which enables vertical displacements up to 500μm and has an embedded position sensor of nanometric precision. The coarse approach motors are first used to approach the probe on the tuning fork at a few micrometer distance from the tip. The smooth displacement of the piezo is then used to measure the interactions of the probe with the substrate. The whole setup is placed on a passively damped breadboard table: isolation is critical for the measurements and all the passive damping elements act as low pass filters for mechanical vibrations. For AFM measurements, the table is even placed in an acoustic box.

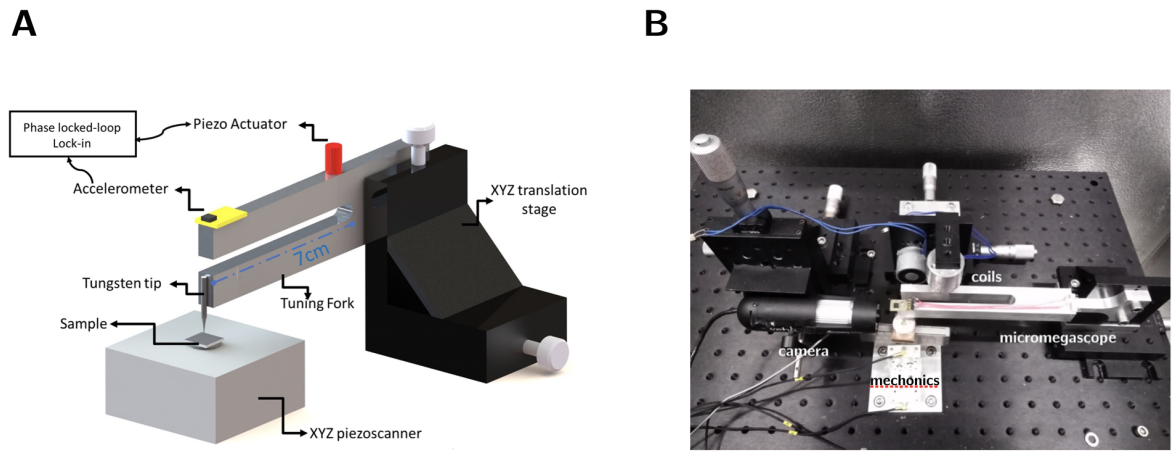

Figure 2.9: **(A)** Sketch of the setup for an AFM scan and **(B)** photograph of the setup for a sfa experiment.

2.3.2 Data acquisition and processing

To measure the mechanical impedance of the force field applied on the tuning fork, we have to measure the shift in the resonance frequency, the amplitude at resonance, and the excitation voltage of the coil/piezo-dither. Hence, we systematically use frequency-modulation AFM techniques, which allow us to measure those parameters in real time. The acquisition and processing of the accelerometers signal is done via a Specs-Nanonis package, designed for AFM experiments. The package consists in one Real Time controller (RT5) with one or two Oscillation Controls OC4 (for each mode) which detect the signal from the tuning fork accelerometers and regulate the ouptut to the coils/piezo, and one high voltage amplifier which is used to increase the ouput voltage to the coils and eventually control the scanner motion when performing an AFM scan.

Signal demodulation

The signal from the accelerometers is detected via a lock in amplifier (operating principle summed up Fig.2.10). This kind of electronic system allows to extract the signal at a given frequency within a determined bandwidth from a noisy environment with a much higher precision than conventional RLC circuits. The lock in is based on the orthogonality of sinusoidal functions: the input signal is multiplied by a reference signal at the desired frequency f_0 and then is integrated over a given time, much longer than the signal period. The resulting signal is a DC signal proportional to the amplitude and phase of the f_0 component of the initial signal, and where the contribution from frequencies different from f_0 vanishes. In order to separate phase and amplitude, the lock in performs this operation twice, with two references that have the same frequency but have a 90°phase shift. It obtains two components X and Y and can recover the amplitude A, and phase shift ϕ, simply by:

$$A = \sqrt{X^2 + Y^2} \tag{2.29}$$

$$\phi = arctan(\frac{Y}{X}) \tag{2.30}$$

The demodulators of the OC4 perform this operation and use the same frequency set for the excitation voltage. Therefore, we recover the amplitude A and phase shift ϕ of the tuning fork oscillations with respect to the excitation voltage E. The important parameters that need to be set are the bandwidth (or cut-off frequency) of the filter and the filter order. In our case, the bandwidth should be set in order to avoid interferences between the two modes. Typically, a cut-off frequency of 50Hz is enough to avoid couplings.

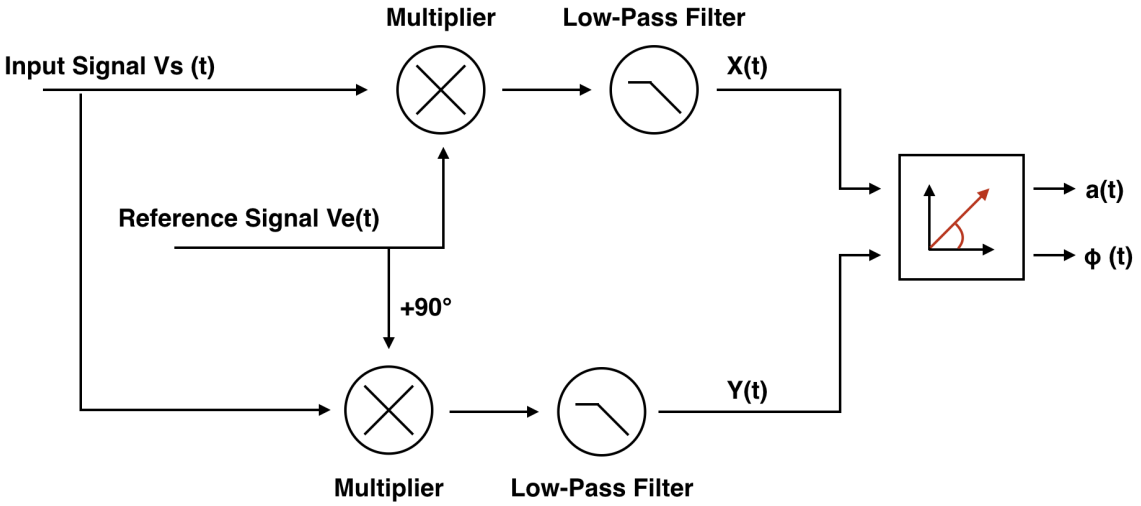

Figure 2.10: Schematic of the operating principle of the lock in amplifier.

Phase Locked Loop (PLL)

To keep the system at the resonant frequency of the tuning fork when it is under interaction with an external force field, we use a Phase-Locked Loop. Essentially, the

OC4 takes as reference the tuning fork phase shift $\phi_0 = \pi/2$ with respect to the excitation voltage signal at the resonance in the absence of interactions, and then, when the system is under interaction, it tunes the frequency of the excitation voltage to keep the same phase shift between the amplitude of the tuning fork and the excitation voltage. In this way, the system is always excited at the tuning fork resonant frequency. The main parameters to adjust are the filter PID coefficients. The Nanonis software automatically calculates the best parameters from the frequency sweep in the absence of interactions.

PID on the amplitude of oscillation

We use an additional PID controller that tunes the excitation voltage E to ensure that the oscillation amplitude A at the resonance remains constant during an experiment. The parameters to set are the PID coefficients. In general, the time constant τ is set around 100ms and the proportional gain P around 10.

2.3.3 Limitations for a dynamic measurement

Intrinsic limitations

We discuss in this section the limitations for dynamic force measurements with frequency modulation techniques [72]. In frequency modulation, the major noise comes from the measurement of the frequency f_0 at which the cantilever is oscillating. In general, the error δf is due to two statistically independent contributions: detector noise and thermal fluctuations with:

$$\delta f = \sqrt{\delta f_{thermal}^2 + \delta f_{detection}^2} \tag{2.31}$$

• **Thermal fluctuations**

For an oscillator submitted to thermal noise, the frequency noise $\delta f$is given by:

$$\delta f_{thermal} = \sqrt{\frac{k_B T B f_0}{\pi K a^2 Q}} \tag{2.32}$$

with B the bandwidth of the filter. In practice, the detector noise is in general greater than thermal fluctuations.

• **Detector noise**

It is possible to relate the error δf to the error δz in the cantilever position. Indeed, the frequency is given by the period T between two consecutive crossings of the 0 position with positive speed. The period T can thus only be calculated with a noise level δT. The uncertainity on the zero crossing is therefore equal to $\delta T/2$ where $\delta T/2$ is equal to the error δz divided by the slope of z(t) at the origin. Because the tuning fork is oscillating at the amplitude A and frequency f_0, the slope is simply $2\pi f_0 A$. And therefore we obtain that:

$$\delta T = \frac{\delta z}{\pi f_0 A} \tag{2.33}$$

Then, since $T = 1/f_0$, we retrieve the error in the frequency measurement:

$$\frac{\delta f_{detector}}{f_0} = \frac{\delta z}{\pi A} \tag{2.34}$$

In fact, this error estimate is correct only if the measurement is done on a timescale close to $1/f_0$. If a longer measurement is performed, we can count more zero crossings and increase the accuracy of the detection. In practice, we can characterize the detector by its noise density n_z (m.Hz$^{-1/2}$)with $\delta z = n_z\sqrt{B}$ and N the number of cycles available for the measurements. This number N is given by the bandwidth of the PLL and the frequency f_0: $N = f_0/B$. Hence, we find finally that:

$$\delta f_{detector} = \frac{\delta z f_0}{N\pi A} \tag{2.35}$$

which leads to

$$\delta f_{detector} = \frac{n_z B^{3/2}}{\pi A} \tag{2.36}$$

2.3.4 Experimental limitations

Brownian noise detection

By performing a frequency sweep without external excitation, it is possible to measure the thermal noise. The amplitude δa is given by the energy balance between the thermal energy k_bT and the mechanical energy $m_{eff}\delta a^2\omega_0^2$. We then find a theoretical value of $\delta a = 10pm$ in excellent agreement with the measured one (see Fig.2.11-A).

Limitations in force detection

The noise limitation depends strongly on the mode, since the related quality factors change substantially. For the normal mode, the typical peak to peak noise in the frequency is about 0.3Hz (Fig.2.11-B) which leads to a peak to peak noise in the force gradient of the order of $1kN.m^{-1}$. For the tangential mode, the noise in the force gradient is the order of $10N.m^{-1}$. The resolution of the dissipative force depends on the oscillation amplitude. Nonetheless, the order of magnitude is typically the tenth of microNewton.

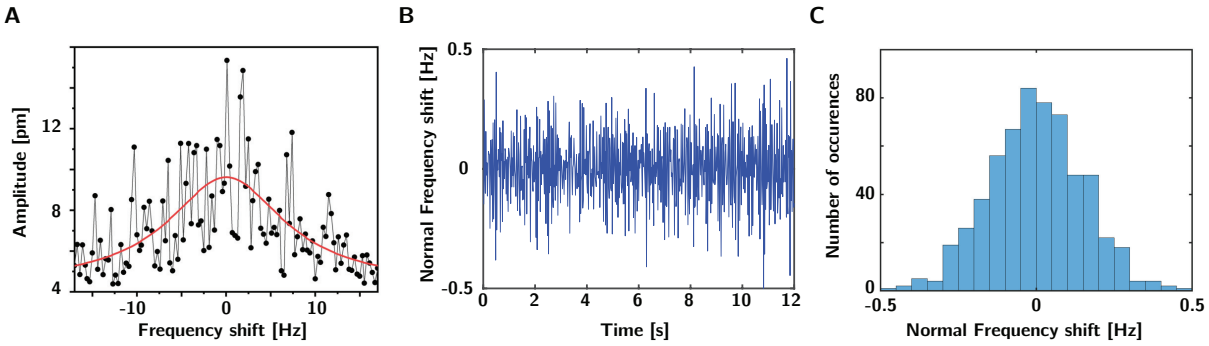

Figure 2.11: **(A)** Detection of the thermal fluctuations of the tuning fork. **(B)** Typical noise for the frequency detection of the normal mode and the corresponding gaussian shape **(C)**.

2.4 Applications to force microscopy and surface force measurements

To test the versatility and efficiency of the Micromegascope in both AFM and SFA configurations, we proceeded to various AFM scans and standard SFA rheological measurements. The data from the latter part was taken and analyzed by Antoine Laine. However, I performed similar experiments with silicone oil to benchmark the ice friction setup.

2.4.1 AFM capabilities

To demonstrate the potential of the Micromegascope for force microscopy, we initially performed a series of approach-retract curves on a silicon dioxide flat surface (see Fig.2.9-A for the setup). The interaction between the apex of a sharp tungsten tip glued at the extremity of one prong and the sample surface is detected by measuring the shift in the resonant frequency. In Fig.2.12, we present the measurement for the fundamental frequency of the normal mode, the first harmonics of the same mode, as well as the fundamental frequency of the tangential mode along with its resonance curves. These measurements prove that the macroscopic force sensor can detect the near-field interaction forces, and demonstrates that the technique can be applied to AFM applications and friction studies.

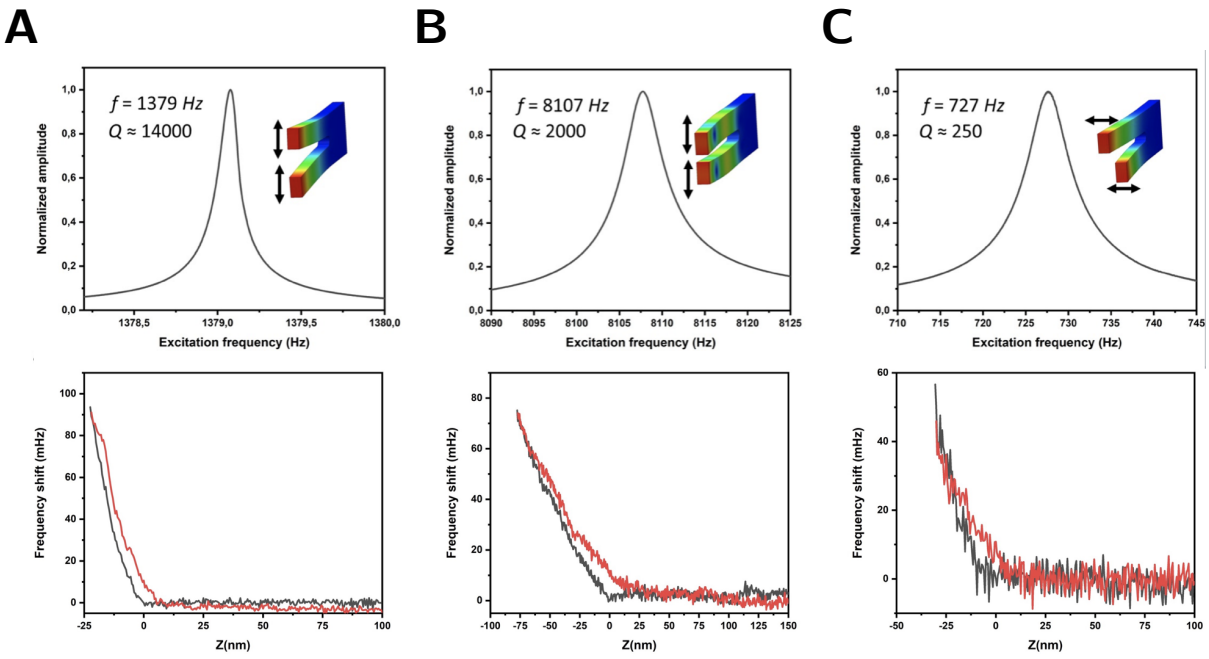

Figure 2.12: Resonances and force curves obtained with a tungsten tip on a silicon dioxide substrate at different frequencies:**(A)** Fundamental harmonics of the normal mode (∼1380 Hz).**(B)** First harmonics of normal mode (∼8100 Hz).**(C)** Fundamental harmonics of the tangential mode (∼700 Hz). Approach in black, retract in red

To go beyond, we also performed AFM images (Fig. 2.13) in frequency modulation. The oscillation amplitude of the tuning fork is kept constant at 10 nm. We imaged a nanometrically resolved standard calibration grating with a pitch of 5 μm and depth 180 nm and a clived mica substrate. Notwithstanding the effects inherent in the piezoelectricity of open-loop scanners (creep, hysteresis...), these scans obtained with a centimetric oscillator correspond in every aspect to the ones expected with a conventional AFM probe. This irrefutably shows the exceptional sensitivity that our centimetric mechanical oscillator coupled with microelectromechanical systems detection can achieve.

Going even further, we proceeded to the imaging of the same calibration grating as above, but completely immersed in a highly viscous liquid, silicone oil (10000 Pa.s). Indeed, AFM imaging in liquid media is still a challenge today. When fully immersed, the quality factor of conventional levers decreases drastically, laser detection is deteriorated by beam reflections on the liquid surface and multi-peak resonances make it difficult to distinguish the natural frequency of the cantilever. To tackle this problem with a conventional silicon cantilever, specific probes have been designed. Similar issues appear with quartz tuning forks. In our case, our sensor does not interact directly with the liquid, so its properties and sensitivity are not affected. The image shown in Fig.2.13-C does not show any more defects than the one obtained in the air, and its realization did not require more technical means. This completes the demonstration of the versatility, sensitivity and ease of use of the Micromegascope for AFM purposes.

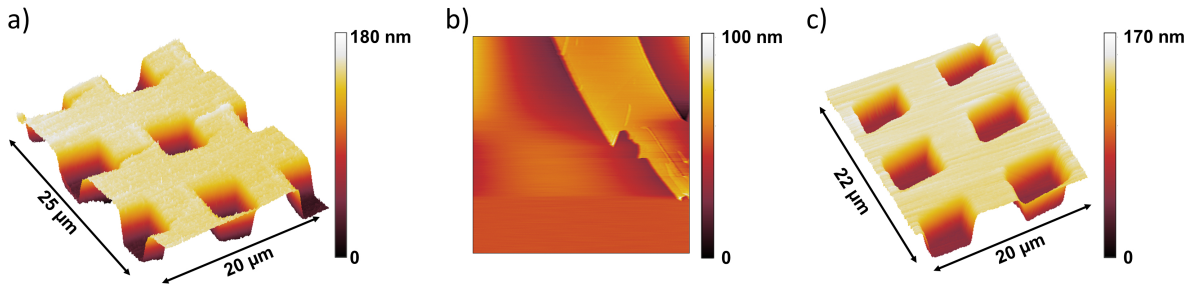

Figure 2.13: **(A)**AFM image of a standard nanoletric calibration grating **(B)** AFM image of a mica sustrate. **(C)** AFM image of the same grating immersed in a very viscous silicone oil.

2.4.2 SFA measurements

To perform rheological measurements, the nanometric tungsten tip is replaced by an atomically smooth sphere of 1.5mm radius. Using a method developed in the Charlaix group, the sphere is obtained from a glass bar of 1mm radius. We break the bar to have pieces of 20mm length and then we use an oxyacetilene welding to melt one end of the bar. It is important to rotate the bar while melting to avoid aysmmetries due to gravity effects. In this way, because of surface tension, we obtain a perfectly spherical and smooth sphere. The sphere is then checked with a binocular to verify for the absence of bubbles that could form if the welding temperature is too high. If it looks smooth, it is washed first with acetone and isopropanol in the clean room and then left for an hour in a piranha solution in order to remove any possible dust left over. Finally, we obtain a clean smooth

sphere which can be used for the experiments, as shown by the AFM scan in Fig.2.14.

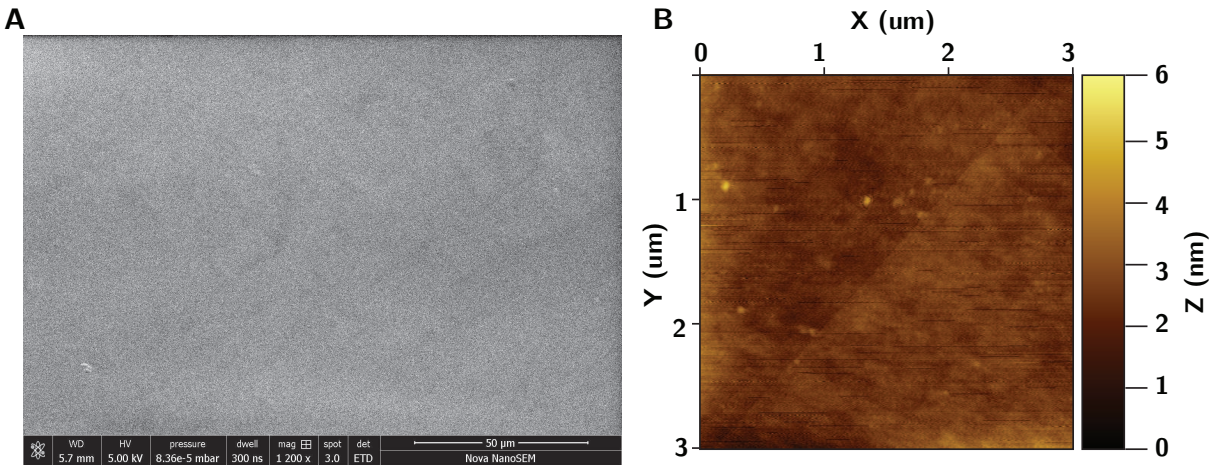

Figure 2.14: Glass surface: **(A)** SEM image of the surface, **(B)** AFM scan of the apex with a RMS roughness of 400pm.

Approach-retracts are done on a mica substrate with a standard silicone oil of 100cst viscosity lying on top of it. A sketch of the set up is shown in Fig.2.15, with the tuning fork oscillating normally to the plane at an amplitude $a_N = 500pm$.

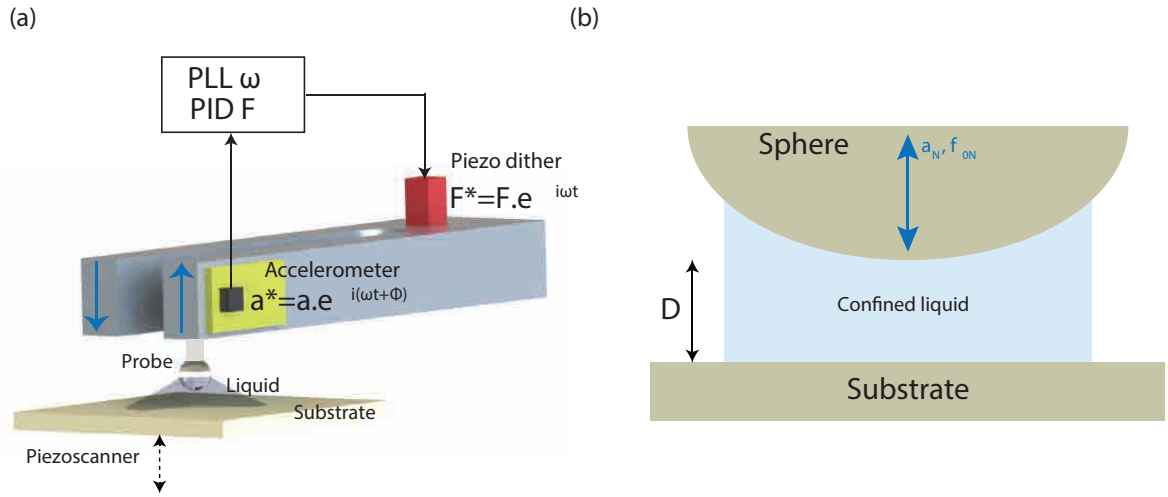

Figure 2.15: **(A)** Schematic of the setup **(B)** Zoom on the interface

In such a sphere-plane geometry, a newtonian fluid,in response to an harmonically driven normal oscillatory strain, presents a purely dissipative mechanical impedance, the impedance being described by the Reynolds formula:

$$Z'' = \frac{6\pi\eta R^2 2\pi f_N}{D} \tag{2.37}$$

where η is the fluid viscosity, f_N the normal frequency and D the confinement distance. Fig.2.16-A shows the plot of 1/Z" versus distance: the linear relationship from several micrometers down to hundreds of nanometers proves that the normal damping is well

described by the viscous drainage force and the viscosity remains constant at its bulk value over this whole confinement range. From the slope, we retrieve a viscosity of 96 mPa.s in excellent agreement with the tabulated value of 100mPa.s. At higher confinements, we observe a systematic deviation from the drainage dissipative response along with a stiffness increase (Fig.2.16-B). We attribute this deviation to elastohydrodynamic effects as previously observed in dynamic SFA with smaller frequencies [73, 74]. In the elastohydrodynamic framework, under a critical confinement distance, part of the liquid is clamped by its viscosity and the mechanical response becomes dominated by the surface deflection, thereby giving access to the surface mechanical properties without contact. Our results present a good qualitative agreement with the elastohydrodynamic model.

In summary, we observe that our MicroMegascope based dynamic Surface Force Apparatus is capable of measuring the micrometer-range rheological response down to molecular confinement. With it, even small interfacial features such as ionic liquid layering can be highlighted ([75]) with unprecedented ease.

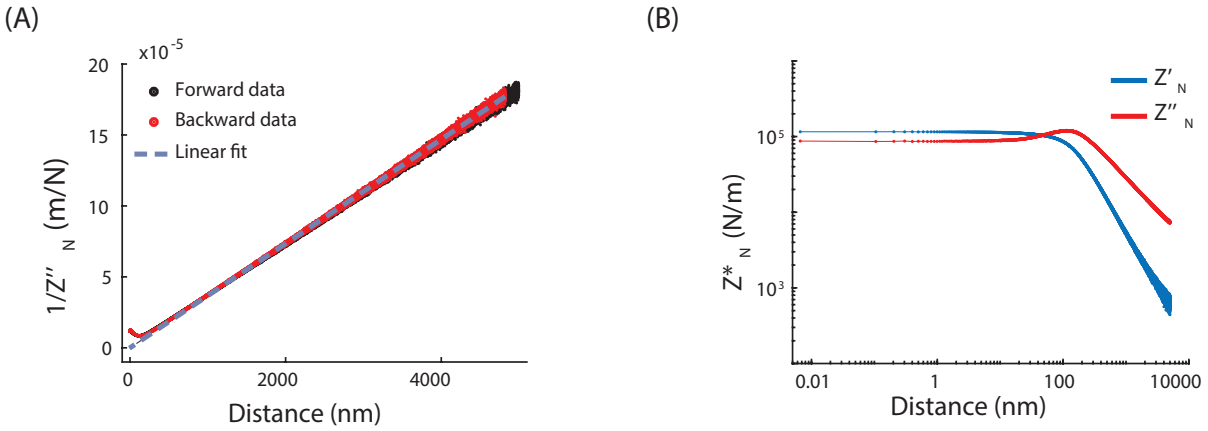

Figure 2.16: **(A)**Inverse of the imaginary normal impedance as a function of distance. Forward(resp. backward) data corresponds to a decreasing(resp increasing) confinement distance. The blue dashed line represents the linear fit of the drainage viscous force. The correspondance of the forward and backward responses discards any hysteresis and highlights the stability of the system. **(B)** Variations of Z' and Z" with the confinement distance: at high confinements elastohydrodynamic effects appear.

2.5 Conclusion

In this Chapter, we have presented a new tuning fork based force sensor for measurements at the nanoscale suggesting it is an ideal apparatus for tribological studies. The main advantages of this device are:
-its very high stiffness which allows a strong mechanical stability, as necessary to indent the stiff ice interface
-its high quality factor, which makes it an excellent resonator,
-its ability to measure quantitatively and separately the conservative and dissipative forces acting on the probe of the tuning fork via frequency modulation AFM techniques,
-its capacity to make macroscopic measurements with nanoscopic sensitivity with unprecedented ease and flexibility, which allows a wide variety of surfaces and liquids to easily examine.

With frequency-modulation techniques, we can directly measure the conservative force gradient $\frac{dF}{dz}$ and the dissipative forces F_d, or equivalently the conservative and dissipative mechanical impedances Z' and Z" of the force field. They are related respectively to the frequency shift δf in the resonance frequency f_0, and to the external excitation force necessary to keep a constant amplitude of oscillation by:

$$Z' = \frac{dF}{dz} = 2K \cdot \frac{\delta f}{f_0}$$

$$Z'' = \frac{F_{\mathrm{d}}}{A_0} = \frac{K}{Q}\left(\frac{E}{E_0} - 1\right)$$

Chapter 3

Applications to contact mechanics

Contents

Macroscopic friction is the result of many, time dependent, nanoscale contacts, hence making the real contact area difficult to evaluate. This makes macroscopic measurements extremely difficult to perform and reproduce. To the contrary, nanoscale friction measurements, which in general are performed with AFM, are extremelly precise, since they can target a single asperity of predetermined shape and size [76, 77, 78]. Indeed, atomic-scale tribological studies have been conducted to evidence new phenomena such as superlubricity [79], the effect of local anysotropies [80] or lattices periodicity [81, 82]. Molecular Dynamics simulations have strengthened the experimental findings, linking them to the developed theoretical models [83, 84, 85]. Nonetheless, it is still unclear how this nanoscale phenomena evolve at larger scales. One of the main reasons is the absence of an experimental tool which allows measurements in the intermediate load regimes with a high-level resolution and relative ease [86].

We have shown that the Micromegascope has the required nanometric sensitivity and mechanical stability to measure local properties in confined fluids. In this chapter, we will show that it is therefore an excellent tool for tribometric measurements. We will first study the contact properties of two rough SiO_2 spheres undergoing mechanical compression. Then, we will first stress that the Micromegascope makes it possible to measure simultaneously the normal and tangential mechanical impedances, and that this enables shear measurements while regulating the normal load. We will then present a first example of tribometric measurement related to lubrication: the friction of a glass bead on a possible phase changing material, in this case the polyethylene glycol.

3.1 Mechanical compression between rough spheres

This section presents work done in collaboration with Eric Clément and collaborators.

3.1.1 Motivations

According to the well-known Amonton law, the friction between two macroscopic solids is linear with the applied load and independent of the apparent contact area A_{app} [87]. It was noted later that in fact the real contact area is much smaller than the apparent one and consists in a large number of small sub-micrometric contacts, called asperities [39].

Many experiments and simulations have therefore focused on the study of individual asperities [88, 89]. In the case of a single asperity, the simplest model which accounts for homogeneous, isotropic, linear elastic spheres is the Hertz model [90], which gives that $A_{asp} \sim F_N^{2/3}$. Note that adhesive effects due for example to capillary condensation yields also a sublinear dependence for the area with the load. Then, the friction force is simply

$F_T = \tau \cdot A_{asp}$ where τ is a shear strength, and thus F_T is also sublinear in load. Indeed, many experiments have reported such behavior. For two solids with multiple asperities, Greenwood and Williamson [91] have shown that it is possible to retrieve macroscopically the Amonton law if we consider that each contact follows a Hertz law and the distribution of contacts is exponential. In the case of a gaussian distribution, they showed that this applies as long we have a separation of scales such that if N is the total number of summits on the surface and n is the number of contacts for a given indentation, we have $1 \ll n \ll N$. Nonetheless, at very small indentations, for extremely rough surfaces, this approximation does not hold and the dynamics of the contacts are still unclear. A recent experiment [92] has shown that a sublinear dependence is indeed obtained for the friction force when rough millimetric PMMA beads move over a flat glass surface (Fig.3.1). By revealing the real contact area with a confinement-induced shining molecule, it was shown that this sublinear dependence was due to strain hardening of the local contacts. Interestingly, it was evidenced that at high indentations the real contact area follows almost a Hertz law, while below $1\mu m$ indentation, it looks like a collection of single asperities.

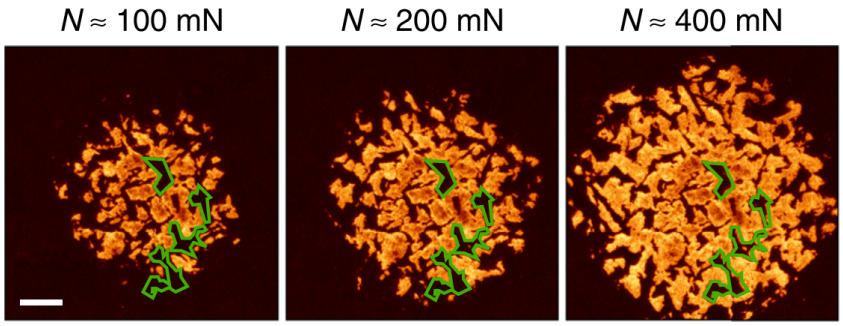

Figure 3.1: Imaging of the real contact area between a PMMA rough sphere and a flat glass plate [92]. A load of 100mN corresponds to an indentation of $1\mu m$.

The way spheres interact has important implications in granular media: indeed, the way contacts are established is critical to explain the transition between jammed situations and flow regimes. In particular, the situation is currently debated for frictional granular assemblies, as the relation between the granular contacts and the external confining pressure is not clearly established [93]. Numerical simulations have shown that for a given confining pressure, the elastic moduli could vary significantly with some packing characteristics such as for example the number of contact per grains [94, 95]. Moreover, for the numerous sound propagation experiments done since the 1950s, the empirical relations at large confining pressures, between confining pressure and sound velocity were found to contradict the classical Hertz relation for two spheres [96, 97, 98, 99]. A recent experiment at very small confining pressures performed by the group of Eric Clement also confirms the same anomalies. Hence, there is a fundamental need for characterizing properly the contact dependence between two rough spheres at small indentations. This work is indeed a collaboration with Eric Clement to understand these discrepancies from the Hertz law.

3.1.2 Experimental setup

The experimental setup is shown in Fig.3.2: we excite the tuning fork at its resonant frequency along the normal (880Hz, Q∼300) direction. While one sphere is glued on the tuning fork, the other sits on a piezo element with nanometric resolution, which brings them in contact. The setup is at room temperature, humidity is around 40%. We perform compressive experiments where the tuning fork is only excited normally and shear experiments where we excite both modes. We use SiO_2 spheres of radius R=750μm. These spheres are extremely rough (Ra ∼90nm, see AFM scans in Fig.3.2-B,C).

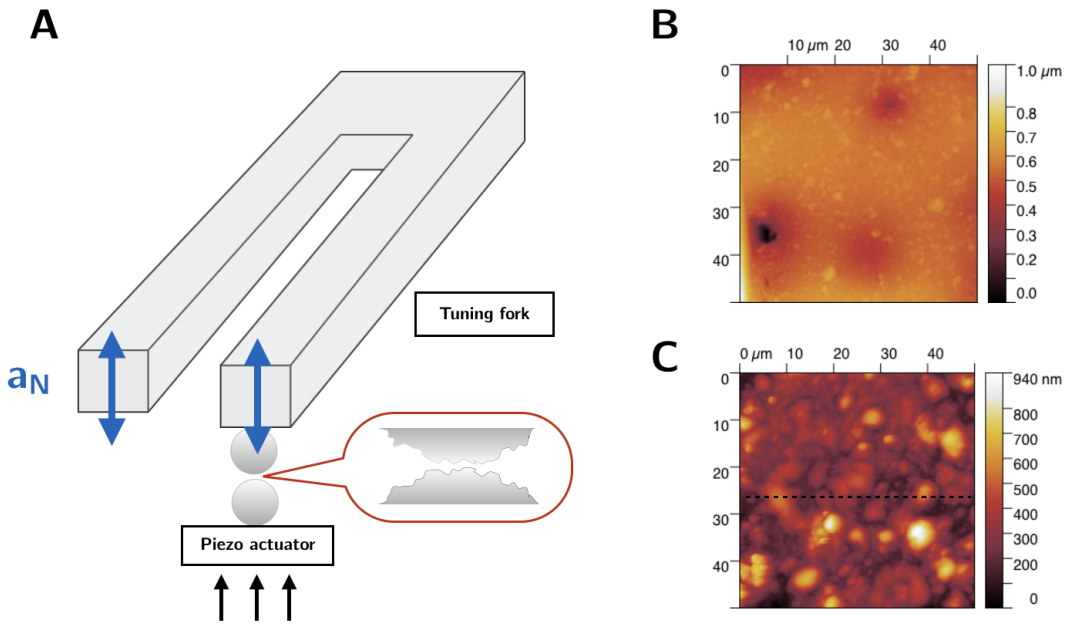

Figure 3.2: **(A)** Sketch of the experimental setup.**(B-C)** AFM scans of two SiO_2 spheres.

3.1.3 Compressive measurements

High indentations

We perform approach-retracts where we indent the two spheres over several hundredths of nanometers and retrieve the normal mechanical impedance $Z_N = Z'_N + i \cdot Z''_N$ as a function of the indentation distance. The oscillation amplitude is set to 5nm while the approach speed to 10nm/s. An example is shown in Fig.3.3-A. The first striking observation is that the contact is mostly elastic with the elastic impedance Z'_N being more than an order of magnitude bigger than the dissipative part Z''_N. Furthermore, the elastic impedance seems to follow a power law.

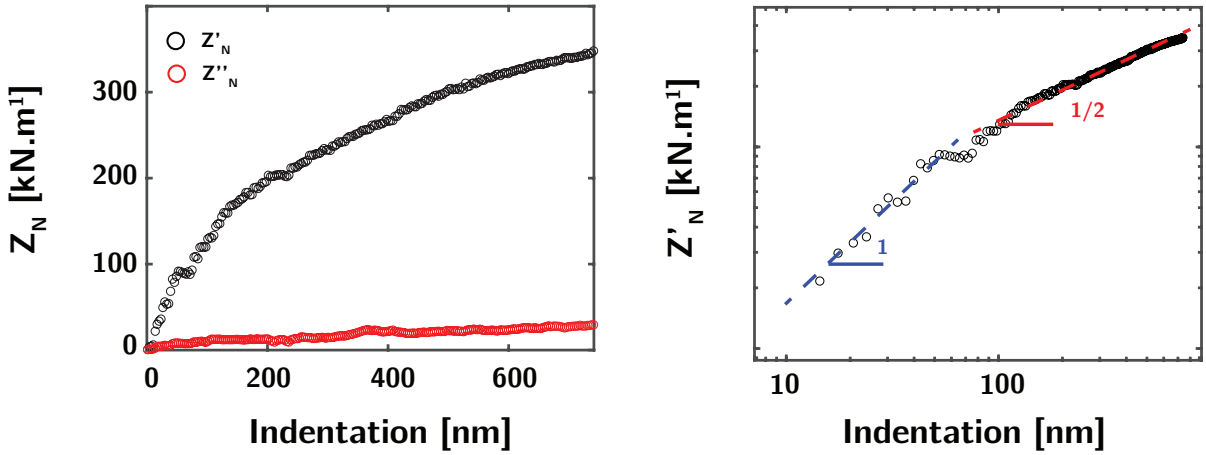

Figure 3.3: Approach curves for the conservative elastic impedance Z'_N (black) and the dissipative impedance Z''_N (red). **(B)** Log-log plot of the elastic impedance reveals two different regimes at low and high indentations.

When plotting the data in log-log scale, we realize the existence of two distinct regimes.

At high indentations (typically above a hundred nanometers), we have a square root dependence with the indentation. This regime corresponds to a standard Hertzian contact. Indeed, in that case, the normal force F_N is directly related to the indentation δ by:

$$F_N = \frac{4}{3}\sqrt{R^*}E^*\delta^{3/2} \tag{3.1}$$

where R^* is an effective radius, (for two identical spheres $R^* = R/2$) and E^* is the effective Young modulus defined by the mechanical characteristics of the two materials in contact $1/E^* = (1-\nu_1^2)/E_1 + (1-\nu_2^2)/E_2$. Therefore, the gradient of the conservative force is related to the indentation by:

$$\nabla F_N = 2\sqrt{R^*}E^*\delta^{1/2} = Z'_N \tag{3.2}$$

From the Hertz fit, we find an effective modulus E^* of 10.4GPa, which yields a Young modulus of 20GPa, considering a Poisson ratio of 0.2. This value is in good agreement with the expected value for SiO_2.

At low indentations, though, we observe a linear variation of Z'_N with the indentation $Z'_N = \alpha \cdot \delta$. This regime is in fact much more unexpected and warrants further investigations. In the following, we will only focus on this regime, limiting the indentations to a maximal value $Z'_N \sim 10^2 \text{kN.m}^{-1}$.

Low indentations

As shown in Fig.3.4, when performing consecutive approach-retracts, we encounter two different situations. Most of the time, we do not observe any difference between the approach and the retract. Both the approach and the retract exhibit the same linear

regime (Fig.3.4-A). It should be noted that the onset of this linear regime is not always at null indentation but varies between 0 and 10nm of indentation, depending on the spheres. However, in a few cases (below 10% of the tested contacts), we observe a hysteresis between the approach and the retract (Fig.3.4-B). Note that in this case, the variation of the conservative impedance with the indentation distance is not linear during the retract phase. This is probably the mark of an additional adhesive force. In the following, we discard such hysteretic data.

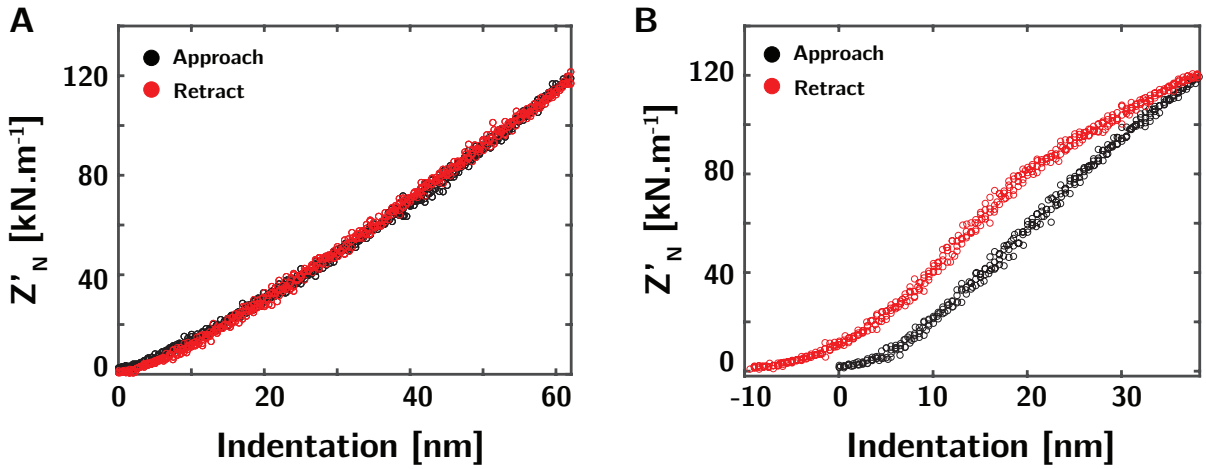

Figure 3.4: **A** Approach-retract where no hysteresis is observed. **B** Approach-retract with a strong hysteresis. In this case, the retract does not exhibit a linear regime.

Performing consecutive approach-retracts does not lead to an evolution of the contact properties as shown in Fig.3.13.

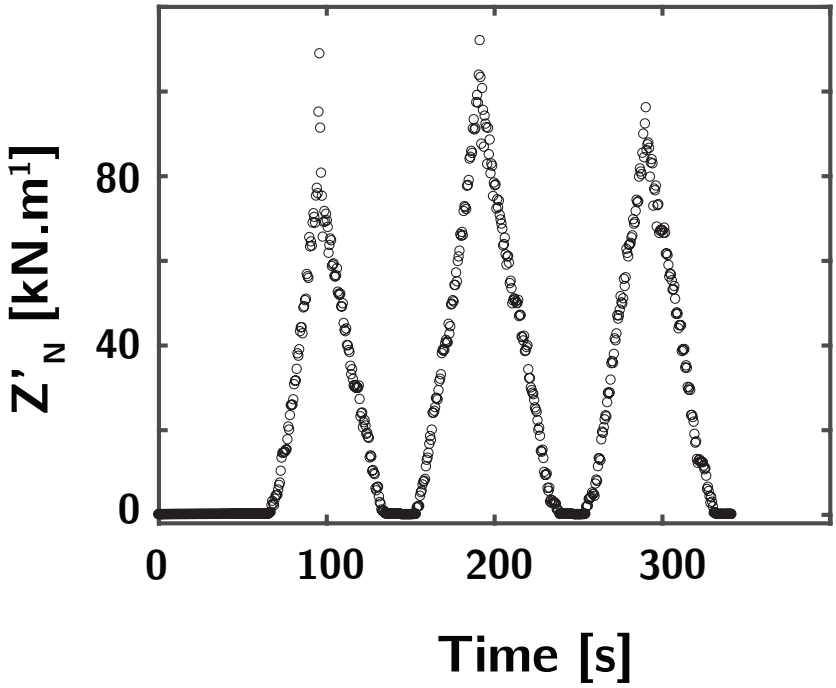

Figure 3.5: Timeseries of the elastic impedance for consecutive approach-retracts.

Amplitude and frequency dependence

Interestingly, when varying the normal amplitude of oscillation a_N, we still observe a linear regime $Z'_N = \alpha \cdot \delta$, but the slope α of the elastic impedance versus indentation distance changes, as shown in Fig.3.6-A. At higher amplitudes of oscillation, the slope is lower. When varying the amplitude over a larger range, we observe two distinct regimes (Fig,3.6)-B. Below a threshold amplitude $a_{N0} \sim 20nm$, the slope is constant ($\alpha \sim 10^{12}$ N.m^{-2}). Above this threshold, the slophe becomes roughly inversely proportional to the amplitude of oscillation. This result may be due to a dynamic effect. In such case, another oscillating frequency would yield a different behavior. To test this hypothesis, we proceed to the same experiment but we leverage the other mode of the tuning fork at 570Hz. The results are shown in Fig.3.6-C: changing the oscillating amplitude does not change the amplitude dependence of α, hence discarding a dynamic effect.

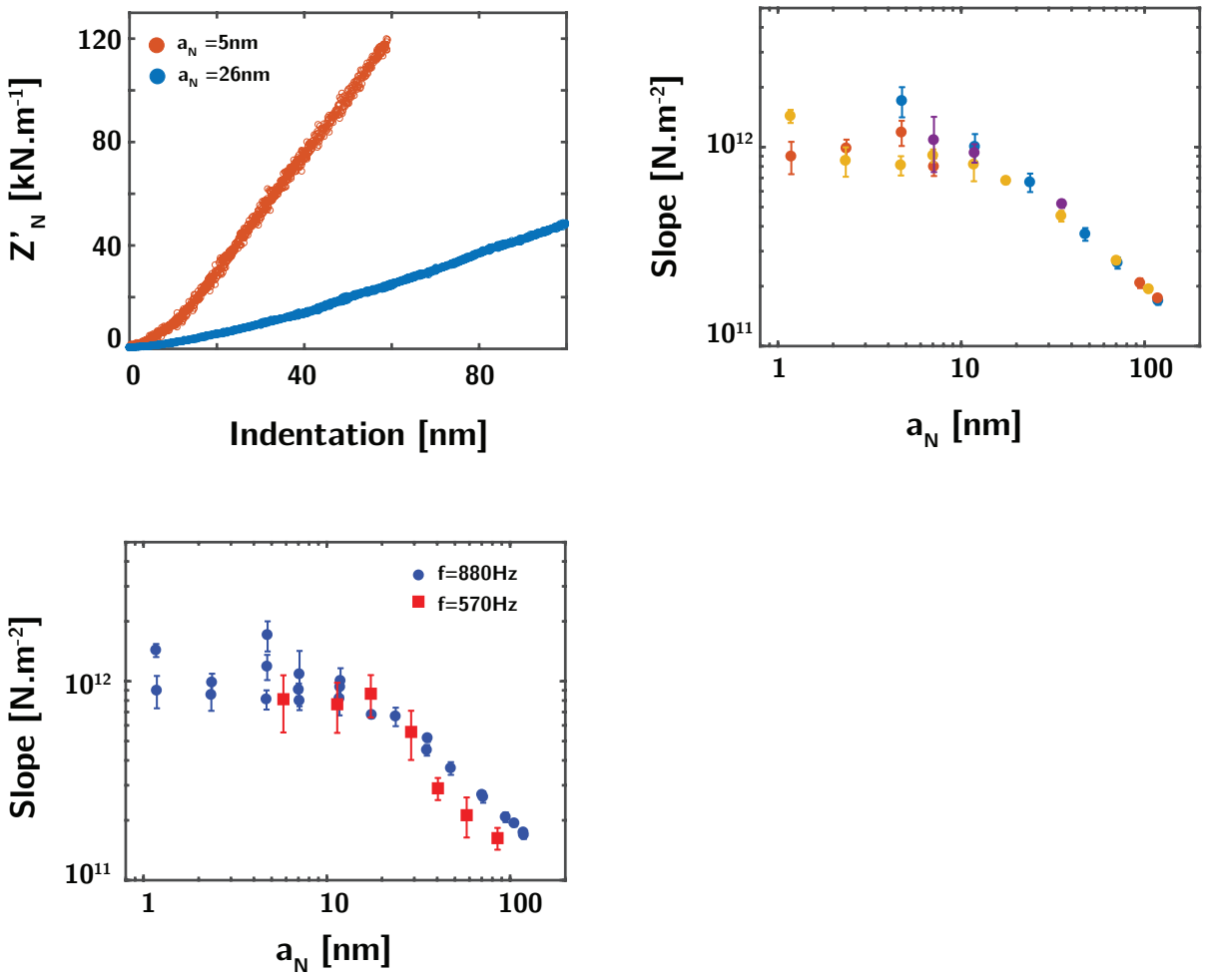

Figure 3.6: **(A)** Approaches at two different oscillating amplitudes yield a different slope for the elastic impedance versus indentation. **(B)** Amplitude dependence of the slope of the elastic impedance versus indentation. Each color corresponds to a different pair of spheres. **(C)** Slope versus amplitude for two different oscillating frequences.

A more probable cause for this decay with amplitude is an averaging effect. When

the tuning fork is oscillating, the frequency shift measured over one period of oscillation at distance z is strictly given by:

$$\Delta f(z) = -\frac{f_0^2}{KA}\int_0^{1/f_0} F\left(a(t)+z\right)\cos\left(2\pi f_0 t\right)dt \tag{3.3}$$

where $F(z)$ is the force field , f_0 the resonance frequency, K the tuning fork stiffness and a(t)=A cos(2πft) the oscillating amplitude [72]. If the force field gradient $k(z)$ is weakly varying over the oscillating amplitude, then one can approximate $k(z+a) \sim k(z)$ and retrieves the known formula:

$$k(z) = 2K\frac{\delta f}{f_0} \tag{3.4}$$

This must be the case in the first regime, where we measure a constant slope independent of the amplitude and frequency of oscillation. In the second regime though, the amplitude of oscillation must be bigger than the typical distance over which the gradient varies, hence we measure an averaged value of the stiffness.

Soft shell model

Our experiments show that at low indentations, the modulus scales linearly with indentation, in the form $Z'_N = \alpha \cdot \delta$. One possible model to understand this behavior is the de Gennes model of soft shell, which assumes that a thin layer of a softer material (Young modulus E*, thickness e) covers the bulk sphere. See the schematic in Fig.3.7-A. This thin layer can be for example a layer of oxides. In this case, while the contact area is still of order $S \sim R\delta$, the pressure now is given by $P \sim E^*\frac{\delta}{e}$. Hence, the compressive force reads:

$$F_N = E * R\frac{\delta^2}{e} \tag{3.5}$$

This model yields a quadratic dependence of the normal force with the indentation distance, which we observe in our experiments. Another prediction of this model that can be tested is the linear dependence with the bead radius. Hence, we have started to do some measurements with other radii. We show in Fig.3.7-B some very preliminary results for R=750μm and R=1.5mm. We observe indeed that the linear slope is doubled when we double the radius. Now, more experiments are currently performed to increase the range of tested radii to further validate this model. In the mean time, we can nonetheless push the analysis: as we obtain, $\alpha = kR$, then $k \sim 2E^*/e$. Numerically, we find k $1.3 * 10^{15}$ leading to $E^*/e \sim 2.6 * 10^{15}$. This soft layer is as thick as the distance over which we observe the linear regime. Hence, typically, $e \sim 50nm$. Then, one finds $E^* \sim 1.3GPa$. This value is as expected one order of magnitude smaller than the measured bulk modulus $E \sim 20GPa$ (see the paragraph above about high indentations).

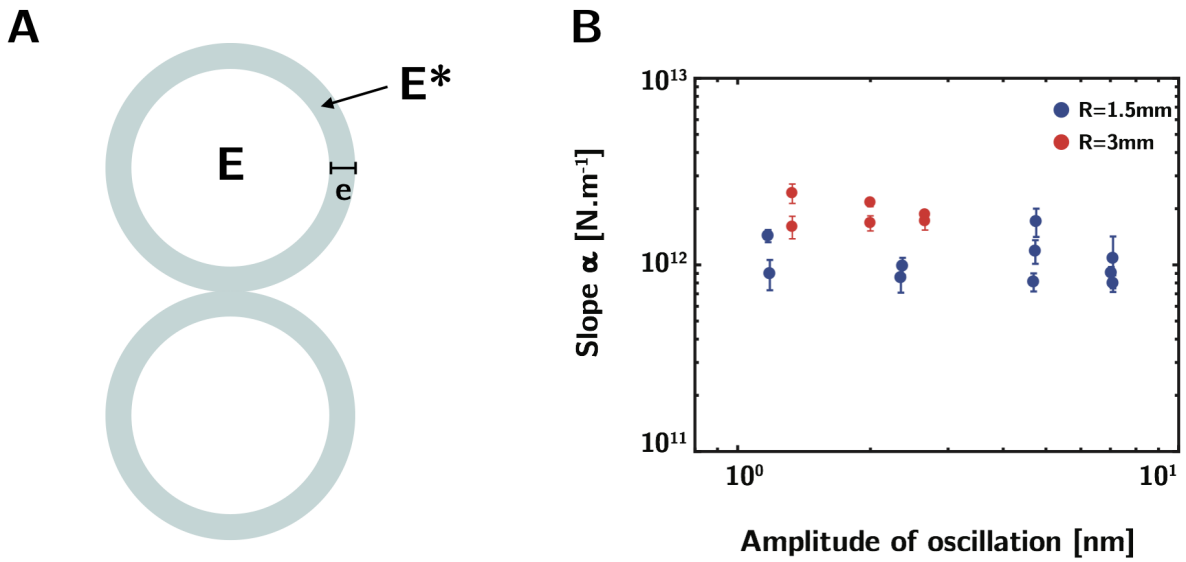

Figure 3.7: **(A)** Schematic of the shell model contact mechanics **(B)** Variations with amplitude of the slope of stiffness versus indentation for two different bead radii.

3.1.4 Linking the local contact to the macroscopic sound propagation in granular media

The group of Eric Clément has performed experiments on sound propagation, which can be compared to the outcome of our study. We report here their experimental setup and main results.

In this experiment, the very same glass spheres are packed in a cubic cell made of Acrylonitrile butadiene styrene (ABS) with a honey-nest inner structure to guarantee phonic insulation and prevent for acoustic bypass. An aluminium outer structure rigidifies the cell. The top plate of the celll is directly made of aluminium and connected to three piezo electric actuators. It can hence move, acting as a piston and imposing thereby a local confing pressure. The typical plate displacement is in the nanometric range, and very small confining pressures can be reached down to a tenth of Pascals, 5 order of magnitudes lower than the weaker pressures that have been investigated so far. The set up allows for driving frequencies up to 6kHz, and the experimental results presented here have been realized at 4kHz. Two accelerometers situated at the top ad bottom plate enable to measure the sound wave propagation through the granular medium. A schematic of the setup is shown above in Fig.3.8.

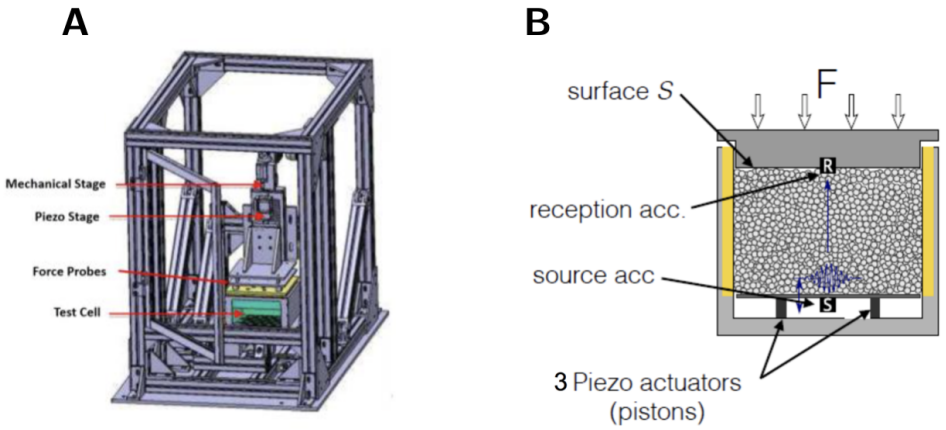

Figure 3.8: **(A)** Overview of the phonic insulation chamber (without the phonic panel walls) that contains the test cell. One can see the two linear stages (mechanical and piezoelectric) mounted onto one another above the force sensors probing the force applied on the top piston (lid of the box) that compresses the grains. **(B)** Vertical cross-section of the cell. The top piston is applying a stress P(t) to ensure a quasi-fixed confinement pressure at the bottom. Under these conditions, the bottom plate is entrained from below by three vibrating piezoelectric actuators that induce a Gaussian wave packet through the granular medium. The acceleration of the vibrating plate is measured by an accelerometer labelled S, while the received signal is measured by another accelerometer labelled R.

The measurements are taken during a parabolic flight at zero gravity. A deeper description of the setup and the data analysis is given in [100]. The macroscopic results presented were taken and analyzed by Adrien Izzet with Eric Clément. As shown in Fig. 3.9, a non linear relation between the local confining pressure and wave propagation velocity is found: the velocity V_c increases weakly with the confining pressure P, following $V_c \propto P^{1/4}$.

The sound velocity depends upon the bulk modulus of the granular medium K:

$$V_c \propto \sqrt{\frac{K}{\rho}} \tag{3.6}$$

where ρ is the volumic mass of the granular medium. In a mean field approach, where we assume that the forces are equally distributed between each contact of each grain, we can relate the local contact between each grain to the bulk modulus. The force F on a contact depends only on the indentation distance δ. As the pressure is given by the sum of the contact forces divided by the surface area of a grain, it is proportional to the average number of contacts per grain Z. Hence, the confining pressure is given by:

$$P \sim \frac{ZF}{R^2} \tag{3.7}$$

For a standard Hertz contact, $F \sim ER^{1/2}\delta^{3/2}$. Hence, one finds that:

$$P \sim ZE\left(\frac{\delta}{R}\right)^{3/2} \sim ZE\Delta^{3/2} \tag{3.8}$$

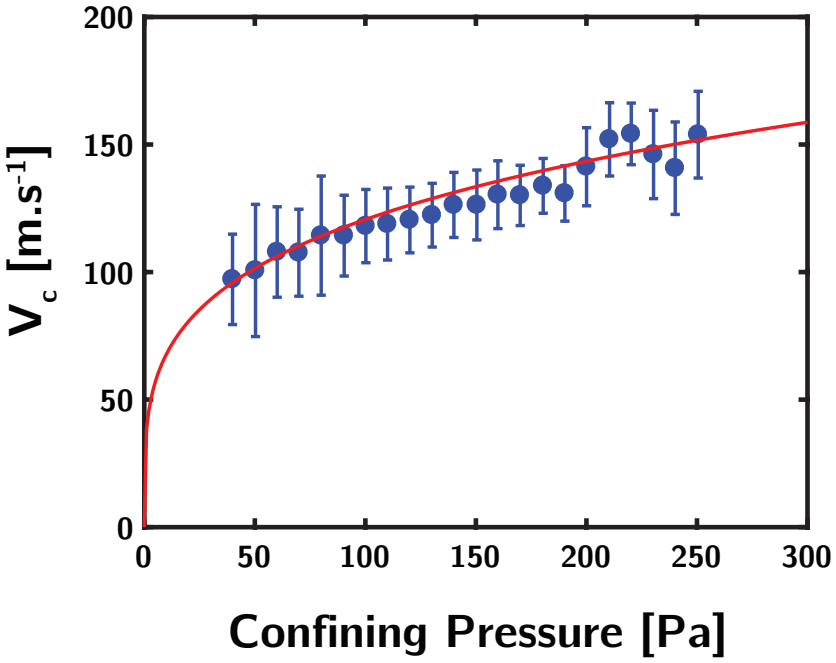

Figure 3.9: Measured sound propagetion velocity as a function of the confining pressure. The red line correponds to the fit obtained with a mean field model derived from the local compressive measurements of section 3.1.3.

where $\Delta = -\delta V/V$ represents the relative variation of volume occupied by the medium. Following [101], the bulk modulus can be expressed as:

$$K = -V\frac{\partial P}{\partial V} = \frac{\partial P}{\partial \Delta} \tag{3.9}$$

Hence taking the derivative of expression 3.8, one obtains the following scalings for the bulk modulus and the speed of sound:

$$K \sim ZE(\Delta)^{1/2} \sim (ZE)^{2/3}P^{1/3} \tag{3.10}$$

$$V_c \sim P^{1/6} \tag{3.11}$$

Thus, a Hertz contact fails to model the experimental findings.

Now, if we consider the experimental results from Section 3.1.3, we found that the elastic impedance Z'_N is related to the indentation δ by $Z'_N = \alpha\delta$, hence integrating yields $F = \alpha\delta^2/2$. Thus one obtains:

$$P \sim \frac{Z\alpha}{2}\left(\frac{\delta}{R}\right)^2 \tag{3.12}$$

This new relation gives the following expression for the bulk modulus and the speed

velocity:

$$K \sim Z\alpha\Delta \sim \sqrt{2Z\alpha P} \tag{3.13}$$

$$V_c \sim \left(\frac{\sqrt{2Z\alpha}}{\rho}\right)^{1/2} P^{1/4} \tag{3.14}$$

The only fitting parameter is the average number of contacts per grain. As shown in Fig.3.9 by the red line, we obtain an excellent fit for our data for Z=5. Such a small value is indeed expected for low confining pressures and similar order of magnitudes has been predicted by numerical simulations [102].

3.2 Tribology and rheology

In this section, we show that we can perform simultaneously tribological and rheological measurements with the tuning fork. This is achieved by probing at the same time both the normal and tangential mechanical impedances (see Fig.3.10). For this aim, the tunig fork is excited simultaneously along the tangential and normal directions. Such technique coined *stroke-probe* gives access to the tribological and rheological properties of confined liquids. It is therefore well suited for the study of tribological phenomena. The high sensitivity along with the high stiffness of our apparatus enable to measure forces from the nanoscale up to the macroscale with relative easiness. The confinement distance is directly imposed by a piezo actuator, thus removing the need of a technically demanding distance measurement setup. Such simplification enables versatility, and allows a wide variety of surfaces and liquids to be examined. In particular, it is a very useful tool to probe the ice interfacial properties under shear. In the following, we will present benchmarks studies with this setup on a standard newtonian fluid (silicone oil) and on a solid material likely to undergo a phase transition under shear at room temperature.

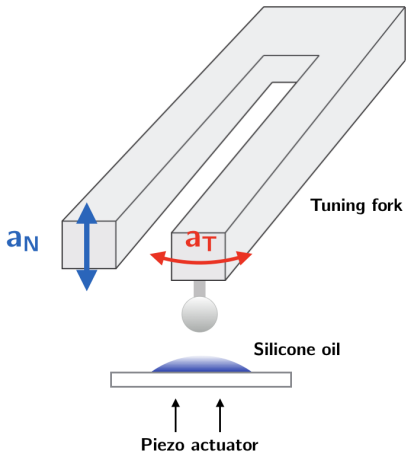

Figure 3.10: Sketch of the experimental setup used with the stroke-probe technique for rheological and tribological measurements. The horizontal and perpendicular modes of the tuning fork are excited simultaneously allowing to probe both the tribological and rheological properties of the medium interacting with a glass bead (a drop of silicone oil in this case).

3.2.1 Measurements on silicone oil

The experimental methodology and setup were validated by benchmarking the results on a simple newtonian fluid. We performed measurements with a standard silicone oil of viscosity 20mPa.s. We chose a small viscosity in order to avoid elasto hydrodynamics effects. Approach-retracts were done on a mica substrate with the oil lying on top of it. The sphere is both excited tangentially at a velocity U=0.018m.s^{-1} (which corresponds to an amplitude of roughly 5μm) and normally. We set the initial normal oscillation amplitude a_N at 26nm. During the approach-retract, we do not regulate the normal amplitude. As a matter of fact, when the probe sinks into the liquid, the normal amplitude decreases until it reaches 0 close to the contact (Fig.3.11-A). Remarkably, upon retract, the curve is almost perfectly symmetrical, which justifies the low hysteresis of the piezo-actuator. In this case, the dissipative impedance Z''_N is simply related to the change in amplitude by:

$$Z''_N = \frac{K}{Q}\left(\frac{a_N}{a_{N0}} - 1\right) \tag{3.15}$$

For such a Newtonian fluid, we expect to retrieve a viscous drainage which is inversely proportional to the confinement distance. Indeed, when plotting the inverse of the dissipative impedance, we retrieve a linear behaviour with the distance. We also obtain experimentally a viscosity of 19mPa.s (from the slope of the approach curve in blue) in excellent agreement with the tabulated value. We observe a slight difference between the approach and retract which might be due to the hysteresis at the beginning of the retract phase of the piezo actuator. Nevertheless, we obtain the same hydrodynamic zero and have a difference in viscosity below 5%. This measurement justifies the complete independence of the two modes that proves that the tangential oscillation has no impact on any normal oscillation.

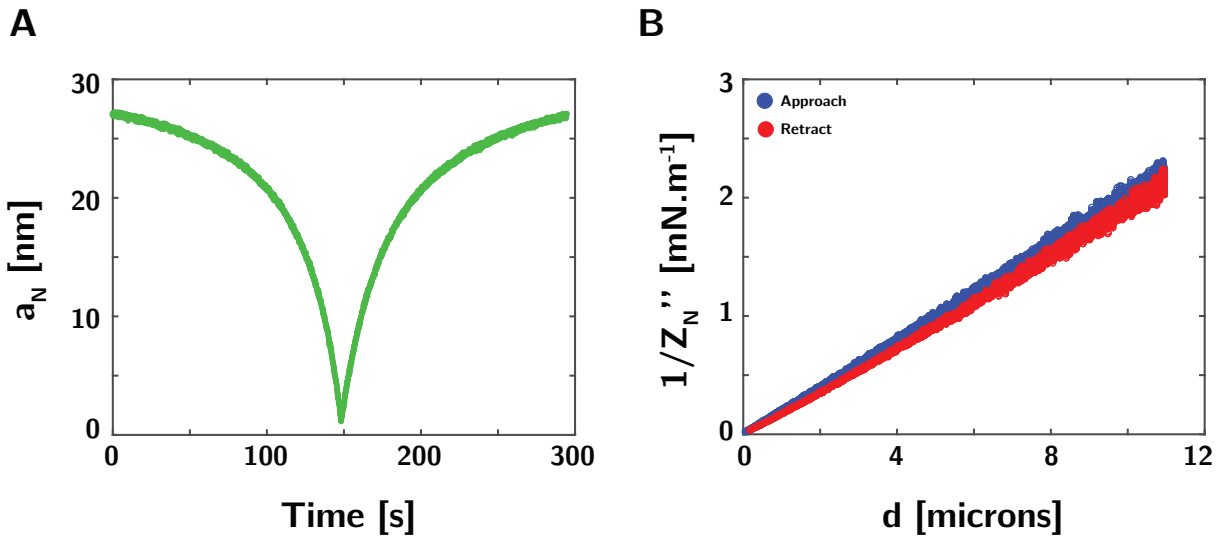

Figure 3.11: **(A)** Normal amplitude decrease during the approach followed by the increase during the retract **(B)** Inverse dissipative impedance as a function of distance during the approach and the retract.

3.2.2 Measurements on polyethylene glycol

Before proceding to experiments on ice, we wanted to test the set up on a different material with less experimental constraints. Chiefly, performing experiments on ice, requires control of the environmental temperature. Therefore, we have looked for a material likely to change phase at room temperature. We have opted for polyethylene glycol (PEG) 1000. First, this polymer melts around 35°C, so the situation at room temperature, is comparable to the situation of ice at -10°C. Liquid polyethylene glycol 1000 has a viscosity of 100mPa.s, but at room temperature, it appears like a waxy solid. Second, polyethylene glycol is used in the industry as a lubricant in aqueous and non aqueous environments for various products (skin creams, personal lubricants...). Hence, we were interesting in seeing whether the origin of these lubricating properties were also due to some phase change as speculated for ice. These experiments were performed with Quentin Louis, a master student from the Ecole Polytechnique, during his internship.

Setup

The experimental setup is very similar to the silicone oil setup (see Fig.3.10). A millimetric glass bead is glued on the tuning fork prong and brought into contact with a substrate of PEG-1000 by a piezo actuator. PEG is molten in a 5mm thick box of 1x2cm surface, and then resolidifies at room temperature. The tuning fork is excited at its resonant frequencies to probe both the normal and tangential mechanical properties of the interface. The tangential speed U is varied between 10^{-3} and 10^{-2}m.s^{-1}, while the normal amplitude is kept constant at 50nm. The whole setup is at room temperature T=24°C. We use a standard piezo element with no embedded position control. Therefore, we calibrate it by interferometry over a range of 50μm to take into account the hysteresis (50μm being the maximal resolution of the interferometric method).

Preliminary observations

In order to get some first insights about the rheological response of PEG, we performed some standard approach-retracts where we indent the PEG surface. As shown in Fig.3.12 A-B, the situation is completely different from what we found on the glass sphere. The first striking difference is the indentation distance: we need almost $100\mu m$, to reach a stiffness of 5kN.m^{-1}, two hundred times more than what needed for the solid rough glass spheres. it should be noted that this distance is bigger than the maximal interferometric resolution (50μm), so we plotted the piezo imposed displacement which could be slightly off from the effective displacement. Nonetheless, the order of magnitude is correct. Furthermore, we are in a regime where elasticity is overcome by dissipation. Interestingly, the elastic part does not follow a square root law, which would be expected for a Hertzian contact.

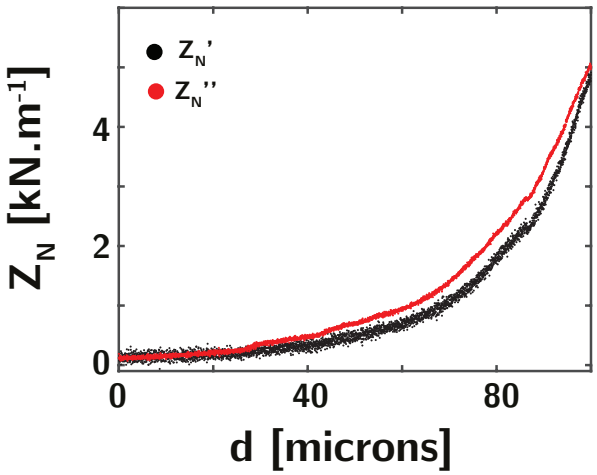

Figure 3.12: Example of an approach for the normal conservative and dissipative impedance.

Experimental procedure

We indent the PEG surface until reaching a constant normal frequency shift $df_N \sim 2Hz$ that corresponds roughly to $Z'_{N0} \sim 4kN.m^{-}1$, then we retract smoothly. Because of the limited range for the piezo calibrated position, we use a coarse motor for the approach, and then the calibrated piezo actuator for a retract distance of 50μm maximum. We measure the friction force F_T at a constant Z'_{N0}, and this for different tangential amplitudes. As shown in Fig.3.13, the data is extremely reproducible for the same spot. However, we observe big differences among the different spots we choose. This big discrepancy is most likely due to the initial state of the PEG surface: indeed, it is difficult to shave it to obtain a very even surface, therefore great differences can emerge from one spot to the other. It should also be noted that the extremely small friction forces we measure despite the huge indentation (tenth of mN, see Fig.3.13-C) underline indeed the excellent lubricant properties of PEG.

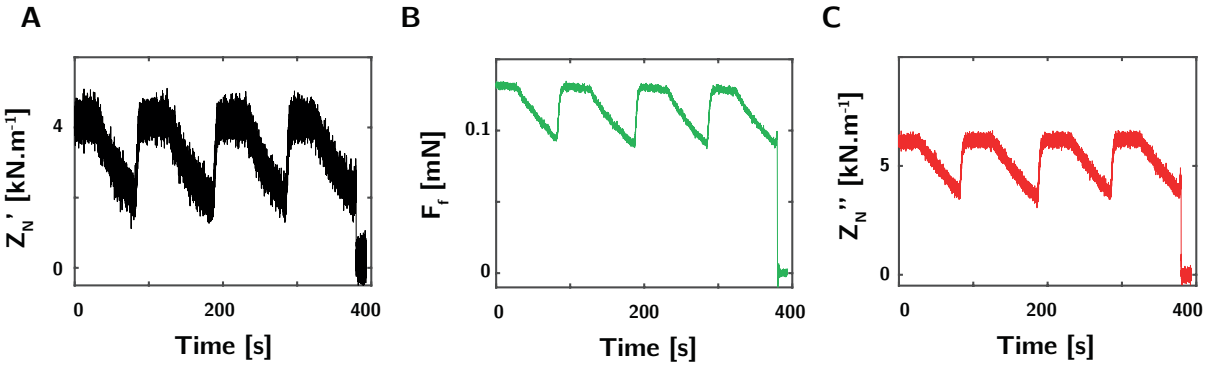

Figure 3.13: Timeseries of consectuive approach-retracts for the normal mechanical impedance **(A-B)** and the friction force **(C)**.

Frictional Properties

Now, we can change the amplitude of oscillation, hence the shearing speed and look at the variations of the friction force F_T with the tangential speed U. The friction force F_T is measured to be an affine function of the shear velocity, $F_T = F_T^0 + \alpha U$, with a finite friction force $F_T^0 \simeq 0.1$ mN as $U \to 0$ and $\alpha \simeq 0.015$ kg.s^{-1} a friction coefficient.

Rheology

In order to test the liquid-like nature of PEG, we plot the inverse of the normal dissipative impedance $1/Z''_N$ versus the retract distance d. Here, the origin for d is taken arbitrarily at the beginning of the retract phase. We observe a linear variation over several microns, which proves that the normal damping is well described by a viscous drainage flow:

$$Z''_N = \frac{6\pi\eta\omega R^2}{h} \tag{3.16}$$

Accordingly, the film thickness h can be directly inferred from the intersection of the extrapolated line with the x-axis and the viscosity η from the slope. As shown respectively

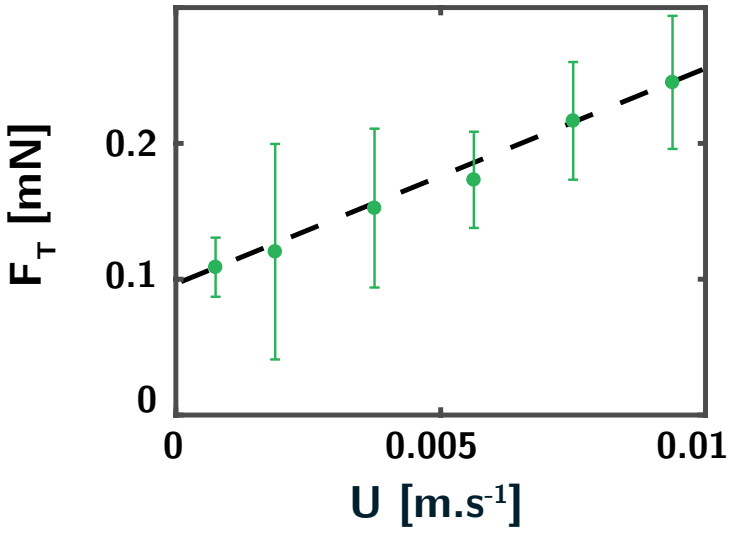

Figure 3.14: Linear relation between the tangential speed U and the friction force F_T.

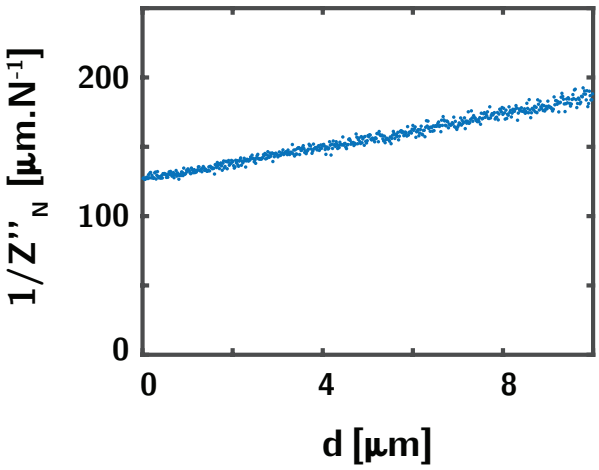

Figure 3.15: Inverse of the dissipative normal impedance as a function of the retract distance. We observe a linear relation, which suggests a hydrodynamic behaviour.

in Fig.3.16A-B, we do not observe any particular variation of the film thickness h_0 and viscosity η_R with the tangential speed. We obtain a mean thickness h_M of 20.4μm. It is surprising to be able to melt such a large liquid film. Indeed, a naive method for estimating a typical timescale for melting would be to divide the energy E needed to form the required volume V by the typical frictional power. E is typically given by the PEG latent heat ($\sim 170kJ/kg$), density ($\sim 1200kg/m^3$) and the volume of liquid. For a film thickness of 20microns, one has an estimated volume $V = 2\pi Rh^2$ since the drainage flow occurs typically over a cylinder of radius $\sqrt{2Rh}$ and thickness h. Then $E = \rho LV \sim 0.6mJ$. The power supplied is given by $P = F_T \cdot U \sim 50\mu W$. Then, one finds a typical melting time $t = E/P$ of 20minutes, way larger than the typical experimental time (around 1minute)! Actually, one cannot exclude finite hydrodynamic slippage of the PEG-1000 on the glass bead under sliding, since slippage is expected to be particularly large for polymer melts. In this case the hydrodynamic film thickness is the sum of the thickness of the flowing layer h_{layer} and a hydrodynamic slip length b: $h_0 = h_{\text{layer}} + b$ [103]. Slip lengths in the

range of microns are common for polymers [104]. Slippage may explain the large value of h_0 as measured in Fig.3.16-A.

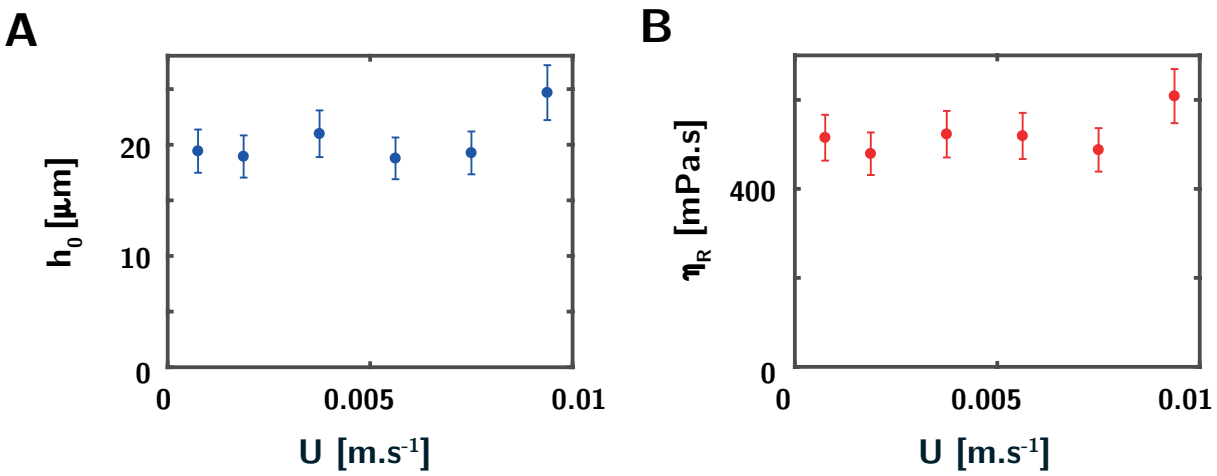

Figure 3.16: Measured thickness and viscosity as a function of the shearing speed.

The extrapolated viscosity is also higher than the viscosity of liquid PEG: we find a mean viscosity η_{RM} of 522mPa.s, five times bigger than the viscosity of molten PEG at 40°C ($\sim 100mPa.s$). To further investigate this discrepancy, we performed rheological measurements using a strain-controlled rheometer (Discovery HR-2 from TA instruments) in a plane-plane geometry. Measurements were performed with a 1mm gap and a Peltier element allowed us to control the local temperature in the gap. We varied the temperature between 50°C and 35°C, corresponding to a range where PEG is expected to be fully molten (above 40°C) or partially (according to the fabricant specifications the melting temperature is in the range 33°C to 40°C). In this range of temperature, we observe a linear relation between stress and strain rate, from which we could extract the shear viscosity (Figs.3.17A-B). The viscosity variations with temperature are shown in Fig. 3.17-C. When the temperature is high enough (above 40°C), we retrieve the tabulated viscosity as well as a low decrease with temperature, which is also given in the usual datasheets. When the temperature is below 37°C, we observe a strong increase in viscosity. The value for the viscosity infered from our TF-AFM methodology ($\eta_R \approx 0.5$Pa.s.) therefore agrees with measurements of the bulk shear viscosity of the molten PEG with standard rheometry.

This suggests that indeed shear induces melting. Above a critical stress σ_c, PEG flows like a standard fluid and we obtain indeed a linear relation with the tangential speed. Hence, PEG behaves as a Bingham fluid with rheology $\sigma = \sigma_c + \eta_R\dot{\gamma}$. Interestingly, we find that polyethylene glycol does not undergo a complete phase transition at the interface but rather exhibits a third-body film. This film is a complex fluid with a non newtonian rheology. We will come back later in the discussion on ice friction on a possible interpretation of this result.

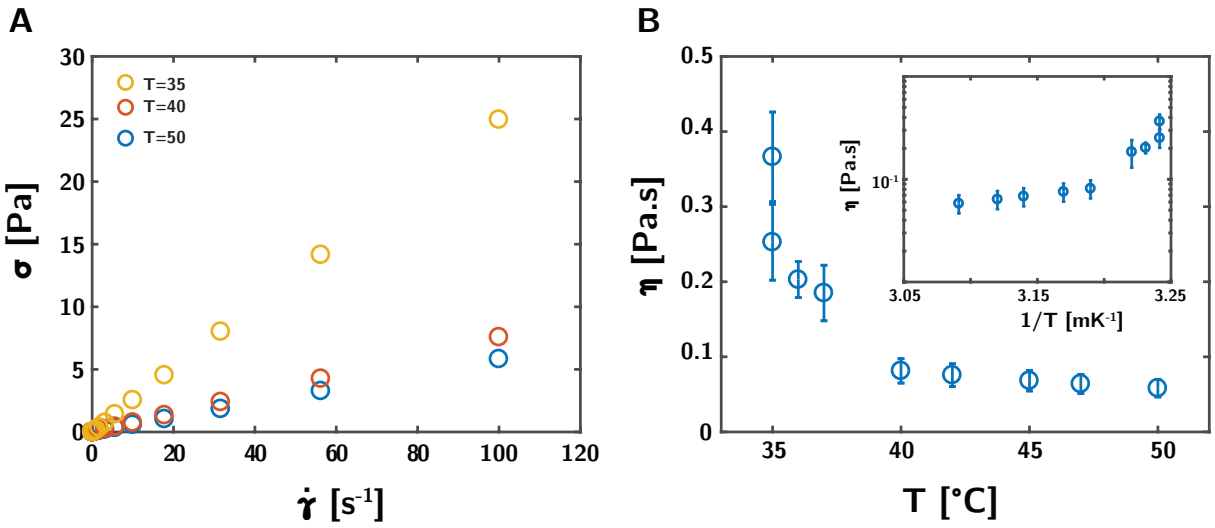

Figure 3.17: Rheology of a 1mm thick film of Polyethylene glycol performed with a macroscopic rheometer. **(A)**: stress-strain rate relation measured at different temperatures. We observe a linear relation, which allows us to retrieve the local viscosity. **(B)** Viscosity variation as a function of temperature. In the inset, an Arhenius-like plot is shown with the variations of the viscosity in log-scale as a function of 1/T.

3.3 Conclusion

In this Chapter, we have shown that the Micromegascope can be used successfully as a tribometer both for solid and lubricated contacts. We have stressed that it was possible to charaterize precisely the local contact mechanics between solid spheres. These measurements show a discrepancy from the standard framework of the Hetzian interaction. They underline a novel mechanism and call for rethinking the standard models of contact mechanics at very low indentations. They also allow us to understand some macroscopical behaviours observed in granular media. In this context, our instrument bridges the gap between nano-measurements and macroscopic ones.

In the context of tribology, the ability to disentangle the frictional properties from the normal mechanical response allows a proper determination of the interface and its properties. We have shown that it is possible to retrieve the rheological properties of a standard viscous fluid such as silicone oil and studied the frictional behaviour of a material that could undergo a phase transition. Interestingly, we have shown that polyethylene glycol does not undergo a straight change from a solid to a liquid phase, but rather passes trough an intermediate state, which appears to behave like a Bingham fluid and which mediates the contact.

The Micromegascope is hence a particularly suitable instrument for conducting tribological measurements on ice.

Chapter 4

Nanotribology of ice

Contents

In this chapter, we investigate the interfacial properties of ice under sliding by making use of the Micromegascope and the stroke-probe technique introduced previously. We present first briefly the experimental setup, and then we focus on the interfacial properties and the effect of hydrophobic coatings that we observe.

4.1 Experimental setup and protocol

4.1.1 Setup

The experimental setup is shown in Fig.4.1: a millimetric glass bead is glued on one prong of a centimetric aluminium tuning fork. The system can be accurately modeled as a mass-spring resonator of large stiffness $K_T \approx 10^2$ kN.m^{-1} and quality factor $Q_T \approx 2500$. An electromagnetic excitation at the tuning fork resonance frequency $f_T \simeq 560$ Hz then yields a lateral oscillatory motion of the bead. Its amplitude a_T varies between 1-30μm and its velocity $U = 2\pi a_T f_T$, typically goes up to 0.1 m.s^{-1}. Simultaneously, we take advantage of the higher order eigenmodes of the tuning fork: as sketched in Fig. 1A, we excite the first normal mode associated to a resonance frequency $f_N \simeq 960$ Hz ($K_N \sim 10^3$ kN.m^{-1}, $Q_N \sim 200$). The characteristics of each mode are summed up in Table 4.1.

Parameter	Tangential mode	Normal mode
Resonant frequency f_0	550Hz	900Hz
Quality factor Q	10^3-10^4	200
Stiffness K	200kN.m^{-1}	890kN.m^{-1}
Amplitude of oscillation	1-30μm	50nm

Table 4.1: Parameters for the two oscillatory modes of the tuning fork

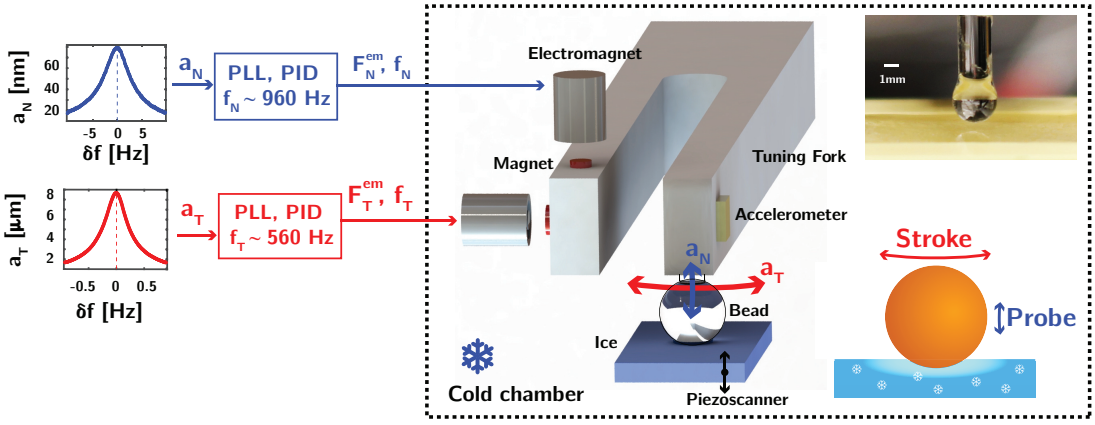

Figure 4.1: **Stroke-probe tribology of ice** Schematic of the set up. A glass bead of radius $R \approx 1.5$ mm, is glued to a macroscopic tuning fork (not to scale). The tuning fork is excited at its resonances, leading to a tangential and normal bead oscillation so as to simultaneously shear the ice (stroke, horizontal red arrow) and measure the interfacial properties (probe, vertical blue arrow).

The whole setup is placed in a cold chamber with controlled temperature between -16°C and 0°C. Ice is made from deionized water (Milli-Q IQ7003/05/10/15, resistivity 18MΩ.cm, pH ∼5.5). The sample is 1x2cm wide and 5mm thick. In order to obtain a clean flat surface, the ice is shaved with a flat blade before each experiment. Environmental humidity is approximately 70-80 % and is independent of temperature. Evaporation occurs over a time scale much longer than the experimental time (more than a day versus 40min to obtain one temperature dataset). A thermocouple measures the ice temperature in-situ and all measurements are reported with respect to the ice temperature. The oscillating sphere is brought into contact with an ice substrate by a piezo element with integrated position sensor of nanometric resolution.

When the sphere shears the ice, the tangential friction force F_{F} can be simply measured by tracking the additional excitation force F_{T}^{em} necessary to keep the oscillation amplitude a_{T} constant while sliding according to $F_F = \frac{K_{\mathrm{T}}}{Q_{\mathrm{T}}}\left(\frac{F_{\mathrm{T}}^{em}}{F_{\mathrm{T},0}^{em}} - 1\right) \cdot a_{\mathrm{T}}$ [75]. At the same time, the normal oscillation with a tiny normal oscillation amplitude $a_{\mathrm{N}} \sim 50$nm, allows us to measure the normal mechanical impedance of the sheared ice $Z_{\mathrm{N}}^* = F_{\mathrm{N}}^*/a_{\mathrm{N}}$ with F_{N}^* the complex normal force acting on the sphere. The real and imaginary part of $Z_{\mathrm{N}}^* = Z_{\mathrm{N}}' + i\, Z_{\mathrm{N}}''$ correspond respectively to the normal conservative and dissipative mechanical impedance of the interfacial medium. Altogether, this superposition methodology allows to probe gently the mechanical properties of the interface while the tangential stroke mode shears laterally the ice surface, echoing the principle of superposition rheometry [105].

4.1.2 Early experiments

In the first experiments, we added below the ice sample a Futek load sensor lsb200 with a resolution below the milliNewton to measure normal loads. The inconvenience of this sensor is that it is extremely soft and as such, it caused mechanical instabilities for the measurements of the normal conservative and dissipative forces. Nonetheless, it was possible to perform approach-retracts, while measuring only the frictional force and the load. As shown, in Fig.4.2-A, at T=-5°C and U=0.01m.s^{-1} we obtain a linear relation between the normal load and the friction force, the friction coefficient μ being small ($\mu = 0.1$) and consistent with the macroscopic experiments with the tribometer. Furthermore, at the end of the retract phase, we measure a negative load: this fact is a preliminary clue to the existence of a meniscus which causes an adhesive force. When varying the tangential speed, we also retrieve a weak power law behaviour for the friction coefficient in agreement with the tribometer findings (Fig.4.2-B).

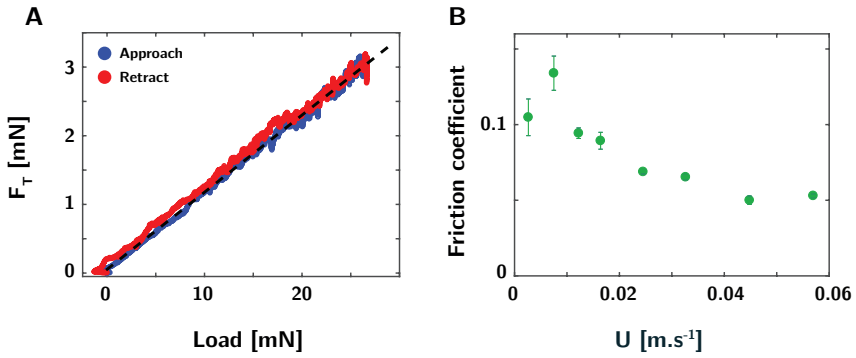

Figure 4.2: **(A)** Linear relation between the friction force and the normal load yielding a friction coefficient μ=0.1. **(B)** Variations of the friction coefficient with the lateral speed.

Indeed, by means of a camera, it is possible to monitor the contact zone during the experiment. As shown in Fig.4.3, we observe a change in the surface when the bead is shearing the ice with the formation of a meniscus.

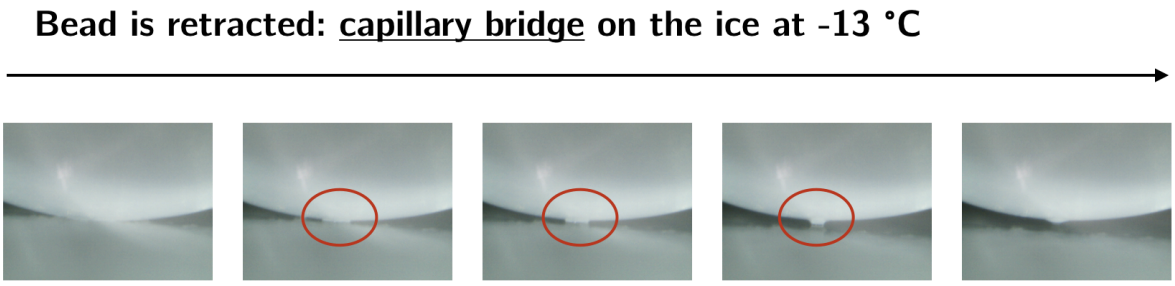

Figure 4.3: Time series of a retract at T=−13°C, where we observe a capillary bridge.

4.1.3 Experimental Procedure

In the following, we describe the experimental procedure implemented without the load sensor. During a typical experiment, the probe is slowly put in contact with the ice, see Fig.4.4-A. During the approach, the indentation distance d decreases and the probe starts shearing the ice, leading to an increase in the friction force. By adjusting the maximum indentation position d, we set the normal conservative impedance Z'_N at a prescribed value Z'_{N0}. We accordingly measure a lateral frictional force F_T for a given prescribed Z'_N0 (see Fig.4.4-A, horizontal red dashed line). Subsequently, the bead is retracted slowly and the friction force decreases back smoothly to zero. Note that during the retract the normal conservative impedance does not exhibit a square root dependence with the indentation as it would be expected for a Hertzian deformation; we come back below on the impedance behavior. Furthermore, the small maximal indentation, typically $\delta_0 \sim 3\mu m$ precludes ploughing dissipation, which has been previously evidenced in relation to higher loads and indentations [14].

For these experiments, we do not have a load sensor. However, we can retrieve the normal interaction by integrating the conservative normal mechanical impedance Z'_N over the indentation distance during the retract phase. We show a series of experiments (Fig.4.4-B)

where we regulate at different Z'_{N0}. For each measurement, we retrieve the normal interaction by integration. As shown, for each Z'_{N0}, we find consistently the same load under regulation. Therefore, we can say that regulating at a given Z'_{N0} is equivalent to fixing the normal load on the sphere.

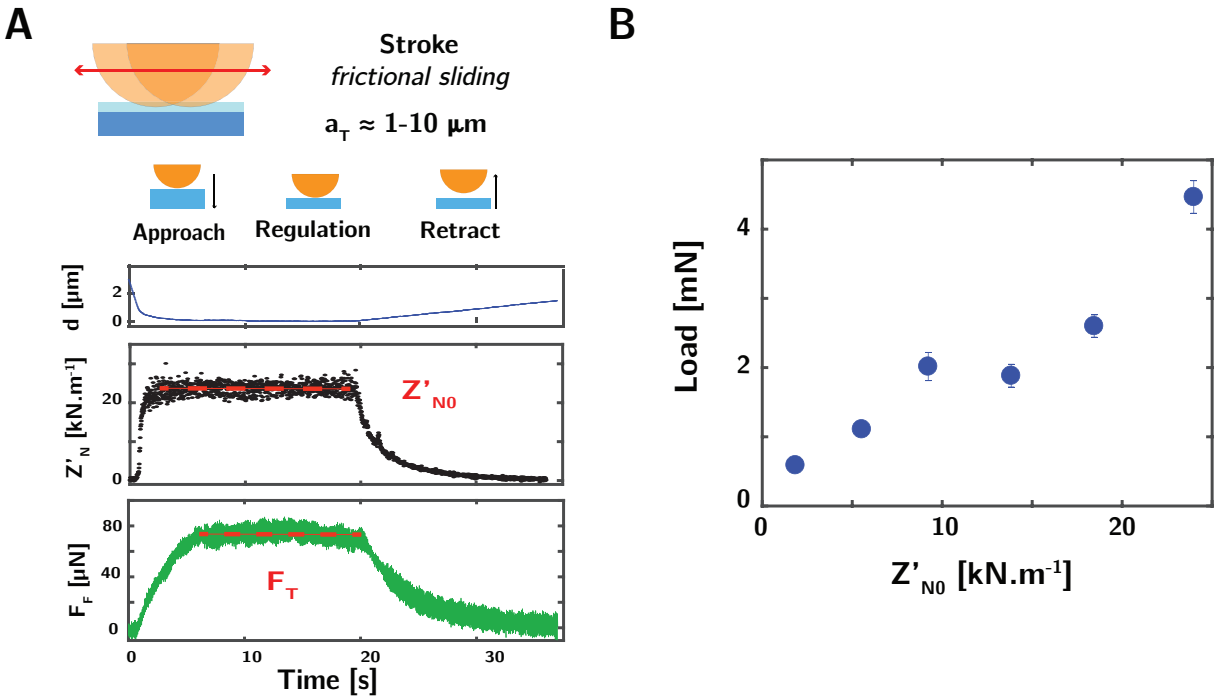

Figure 4.4: **(A)** Typical approach-retract curve for the indentation distance d and the tangential frictional force F_{F} ($T = -6°\mathrm{C}$) at U=0.005m.s^{-1}. Regulating at prescribed value Z'_{N0} allows to define a steady-state friction force F_{T}. **(B)** Equivalence between fixing the the normal impedance and fixing the normal load.

Data reproducibility

Before each experiment, we proceed to a few preliminary approach-retracts to level the surface. This procedure allows us to get reproducible measurements under a fixed load (see Fig.4.5). The measurements are done as the same spot. We do not observe strong variations over time. Unless specifically mentioned, all the measurements presented below are performed for the same value $Z'_{N0} = 24kN.m^{-1}$, corresponding to a load of 4.5mN.

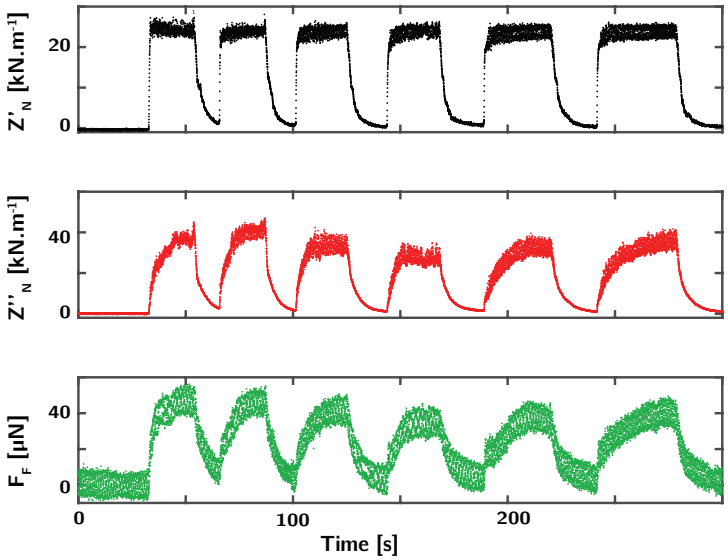

Figure 4.5: **Data reproducibility** Timeseries of consecutive approach-retracts for the real **(A)** and the imaginary part. **(B)** of the normal mechanical impedance as well as for the friction force **(C)**.

4.2 Frictional properties

We report in Fig.4.6, the lateral friction force F_{T} as a function of the tangential velocity U (associated with a_{T} in the range $1 - 30$ μm). The friction force does not vanish at low speeds, similarly to solid-on-solid friction. In addition, a weak power-law decay of the frictional force versus velocity is observed, with $F_{\mathrm{T}} \propto U^{-\gamma}$ where $\gamma \sim 0.3 - 0.5$. This behavior is consistent with previous macroscopic measurements on ice and snow [8, 9] and with the observations of our macroscopic tribometer (see section 1.3.2). Furthermore, repeating these measurements for various temperatures allows us to obtain the temperature dependence of the friction force, see Fig.4.6-B. The friction force (here shown for two different velocities) is shown to increase steadily as the melting point is approached. As compared to our macroscopic measurements, the minimum seems therefore slightly shifted towards lower temperatures. In fact, the rather large variations on the position of this minimum with temperature in the literature is still consistent with our findings (see for example, the variability in the recent experiments of Weber et al [14]). Interestingly, the friction increase close to the melting point also bares similarities with the temperature dependence of the force required to separate two ice particles [106].

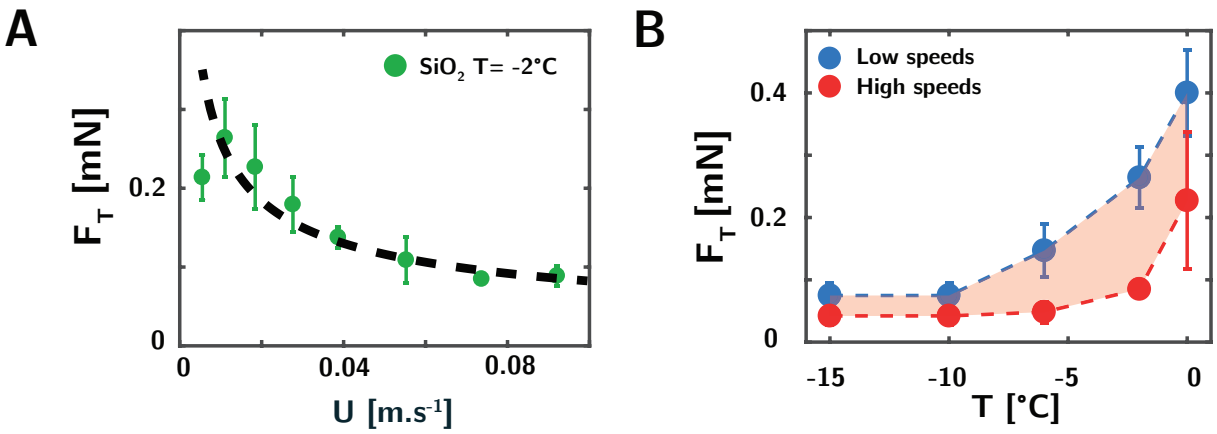

Figure 4.6: **(A)** Steady-state friction force F_{T} as a function of tangential speed U. The dashed line is a fit according to $F_{\mathrm{T}} \propto U^{-\gamma}$ with $\gamma = 0.5$. **(B)** Friction force F_{T} as a function of the ice temperature for two distinct velocities ($U = 0.01$ m.s^{-1} and $U = 0.1$ m.s^{-1}), exhibiting a steady increase close to the melting point.

Furthermore the friction force at a fixed velocity is found to be proportional to the normal load (Fig.4.7). This points to a solid-like friction characterized by a friction coefficient $\mu = 0.015$; this value is also in very good agreement with macroscopic measurements on ice [14]. Finally, we retrieve all the features that we had observed with our tribometer and reported in the first chapter.

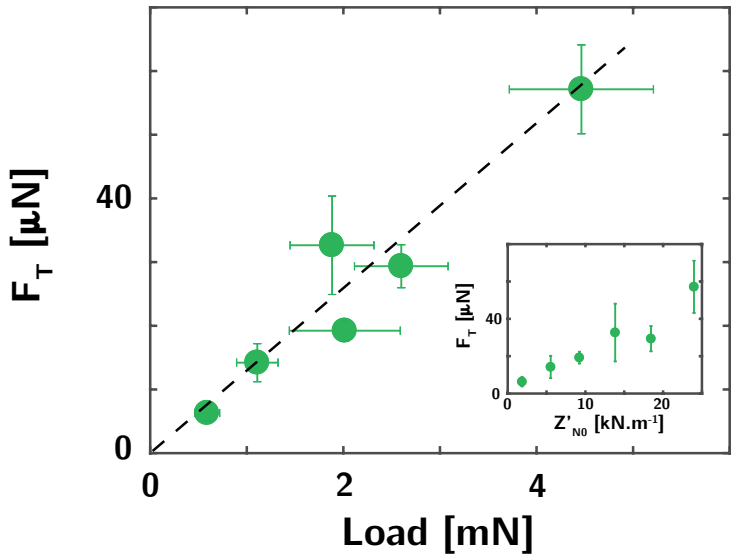

Figure 4.7: Friction evolution with the integrated load, we observe a linear relation typical of a solid-like friction.

4.3 Interfacial Properties

4.3.1 Analysis Method

Now, to measure the properties of the interface during sliding, we take advantage of the additional normal oscillation of the tuning fork. As described above, the real (Z'_{N}) and imaginary (Z''_{N}) parts of the mechanical impedance, which are respectively related to the elastic and dissipative response of the interface are measured. The range of the oscillation amplitude $a_{\mathrm{N}} = 50$ nm enables a resolution below the estimated frictional film thicknesses [107] and close to the magnitude measured for the premelted film on ice [21, 108, 109, 23]. The variation of the normal mechanical impedance Z''_{N} under contact and upon retract is shown in Fig.4.8-A. We observe the same trends as for the friction force F_f: a plateau during the regulation at Z'_{N0}, followed by a smooth decrease during the retract.

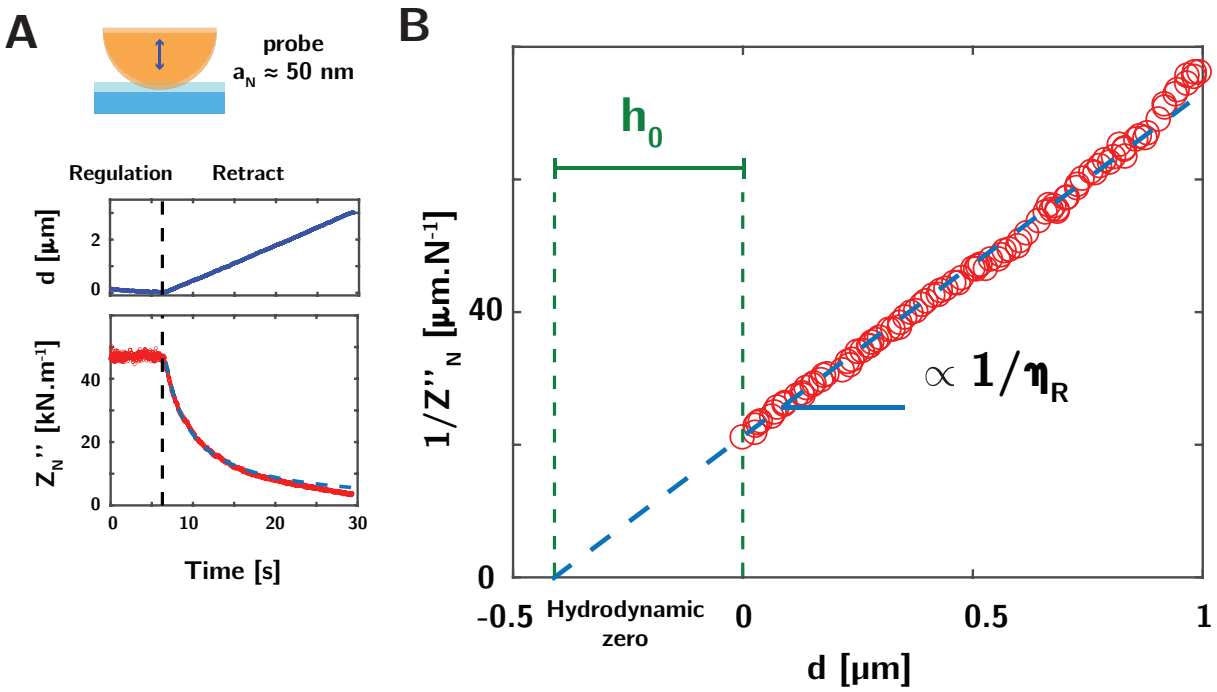

Figure 4.8: **Measuring the thickness of the interfacial film (A)** Retract curve for the dissipative (Z''_{N}, red) normal mechanical impedance while the bead is simultaneously shearing the ice surface at speed $U = 0.01\mathrm{m.s}^{-1}$ ($T = -2°\mathrm{C}$). Under regulation, a steady state is reached. Upon withdrawal, the impedance Z^* relaxes smoothly to zero. **(B)** Inverse of the mechanical impedance $1/Z''_{\mathrm{N}}$ as a function of the separation distance d (during the retract phase). The origin $d = 0$ is fixed arbitrarily at the beginning of the retract phase. The film thickness h_0 (green) is calculated as the distance to the extrapolated hydrodynamic zero. The linear variation of $1/Z''_{\mathrm{N}}$ versus the distance is accounted for by the Reynolds formula, Eq.(1), and points to the liquid-like nature of the interfacial layer.

Further insights into the dissipation are obtained by plotting the inverse of the dissipative impedance $1/Z''_{\mathrm{N}}$ as a function of the separation distance d ($d = 0$ corresponds here to the beginning of the withdrawal phase); see Fig.4.8-B. A first key result from this plot is that a *linear variation* of the inverse normal impedance is measured as a function of the separation d. This suggests a hydrodynamic-like response of the interface during the withdrawal, consistent with the Reynolds law:

$$Z''_{\mathrm{N}} = \frac{6\pi\eta_R R^2 \cdot \omega_{\mathrm{N}}}{h_{\mathrm{hyd}}} \tag{4.1}$$

where R is the sphere radius, h_{hyd} is the hydrodynamic film thickness and η_R the viscosity. For a non-vanishing shear velocity U, the interstitial fluid exhibits a viscous-like response during the retract.

In the stationary state, the hydrodynamic film thickness h_{hyd} is not fixed *a priori* but self-adjusts to reach a stationary value. According to the linear relation between h_{hyd} and $1/Z''_{\mathrm{N}}$ highlighted above, the thickness h_0 of the stationary film can then be obtained from the measurement of the dissipative modulus Z''_{N}. As shown in Fig.4.8-A in the regulation regime, Z''_{N} reaches a plateau as a function of time under imposed shear velocity U and normal load. Accordingly the stationary film thickness h_0 is deduced from this plateau value thanks to Eq.(4.1) in Fig.4.8-B: h_0 can be read on the graph by extrapolating the $1/Z''_{\mathrm{N}}$ line versus h_{hyd} to the zero intercept (dashed blue line): h_0 then corresponds directly to the absolute value of the extrapolated hydrodynamic zero (Fig.4.8-B, green dashed line). Note that by convention, and to make the reading easier, we set in Fig.2-B the position of the sphere corresponding to the plateau value to $d = 0$, so that h_0 corresponds directly to the absolute value of the extrapolated hydrodynamic zero.

In principle the hydrodynamic thickness is expected to be the sum of the actual film thickness and a slip length, if any. However since ice is hydrophilic, a very small slip length is expected (typically few nanometers) [103], so that the hydrodynamic thickness should be safely identified to the real film thickness. In addition, it is possible to retrieve the viscosity from the slope. Further verifications on the experimental procedure and analysis are given in the Annexe A.

4.3.2 Film thickness

We repeat this procedure under various experimental conditions to retrieve the stationary film thickness as a function of the lateral sliding speed, normal load and temperature in the considered sphere-plane geometry. We report in Fig.4.9-A, the variation of the film thickness with the tangential speed U. Surprisingly, the equilibrium film thickness is found to only scarcely depend on the tangential speed, in contrast to the common belief that a larger velocity would induce a larger film [110, 107]. Similarly, it shows a weak variation as a function of the normal load (Fig.4.9-B).

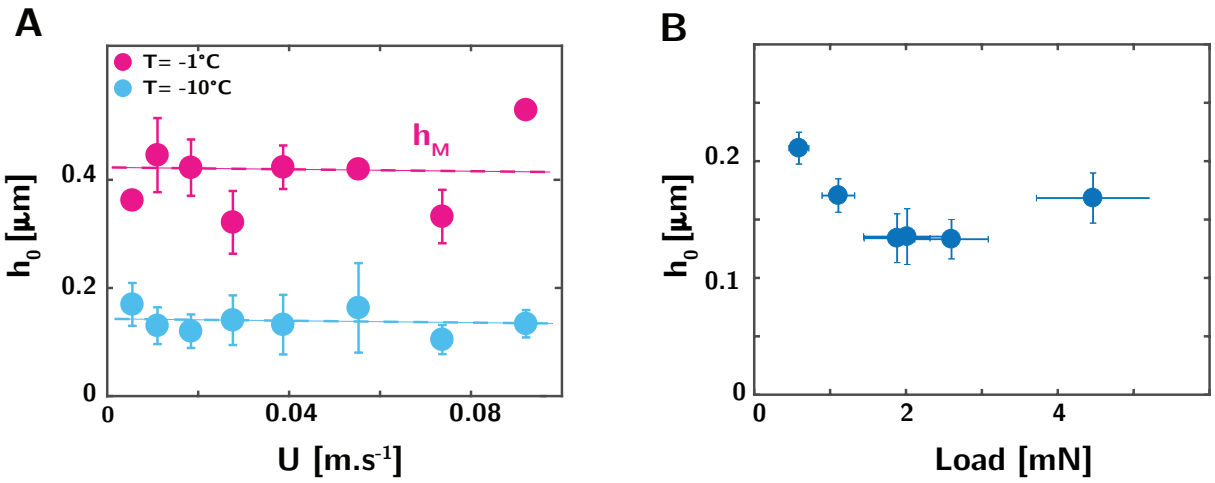

Figure 4.9: **(A)** Measured thickness h_0 as a function of speed for two temperatures ($T = -10$ °C and $T = 0$ °C) In each case, there is no variation with the shearing speed U. **(B)** Average thickness h_0 as a function of the imposed load for a give speed.

However, the thickness increases with temperature (Fig.4.10) ranging from 100 nm to 500 nm. Remarkably, the thickness of the stationary film is slightly but not considerably larger than the values for the equilibrium premelting films (pale blue in Fig4.10) [21, 108, 109, 23].

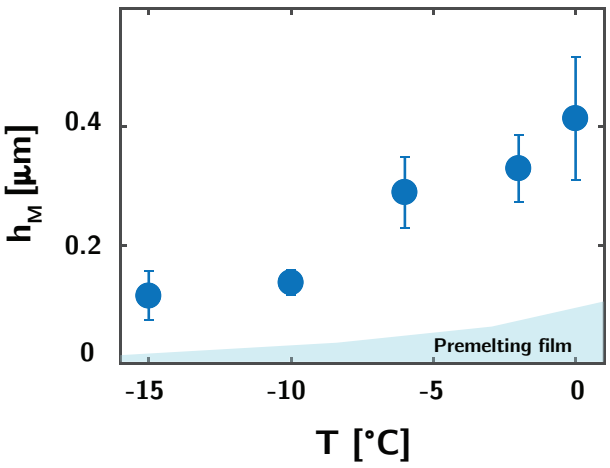

Figure 4.10: Average thickness h_M as a function of T. As intuitively expected, we observe an increase in the film thickness as we approach the melting point. An upper limit for the thickness of the premelting film on ice taken from theliterature is shown in pale blue [111].

4.3.3 Rheology

A second fundamental lesson emerging from these measurements is that the interfacial film exhibits a visco-elastic rheology, associated with a complex viscosity $\tilde{\eta} = \eta_{\mathrm{R}} - i\eta_{\mathrm{I}}$ [112, 113]. Indeed, as shown in Fig4.11, the inverse of the elastic impedance $1/Z'_N$ also exhibits a linear variation with the separation distance d during the retract, allowing to retrieve both real and imaginary parts of the viscosity, η_R and η_I, from the slopes. Accordingly, the linear extrapolations of both the elastic and the dissipative modulus cross at the same hydrodynamic zero within 30% error. Such visco-elastic response of the interstitial film is analogous to that of complex fluids, *e.g.* polymers and polyelectrolytes [112, 113].

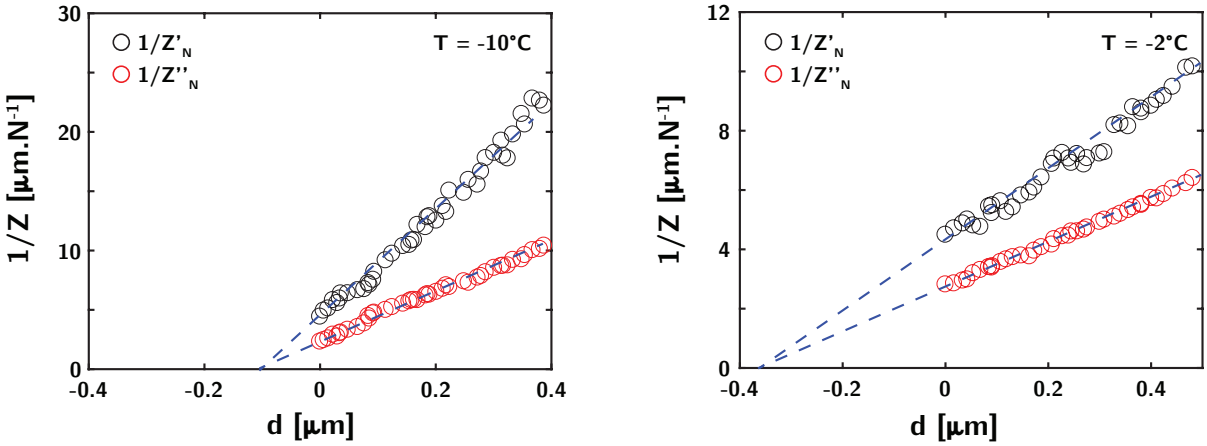

Figure 4.11: Inverse of the normal mechanical impedance $1/Z'_N$ (black) and $1/Z''_N$ (red) as function of the retract distance at T=-10°C **(A)** and T=-2°C **(B)**. We observe a linear relation typical of a complex fluid.

Quantitatively, a first striking result is that the viscosity η_{R} is much higher than the typical viscosity of supercooled water at the same temperature $\eta_{\mathrm{W,S}}$, see Fig.4.12-B (orange dashed line) [114]. Both the real and the imaginary part of the viscosity follow a weak power law decay as a function of the tangential speed, similarly to the friction force:: $\eta_{R,I} \propto U^{-\alpha}$ with $\alpha \sim 0.3 - 0.5$, see Fig.4.12.

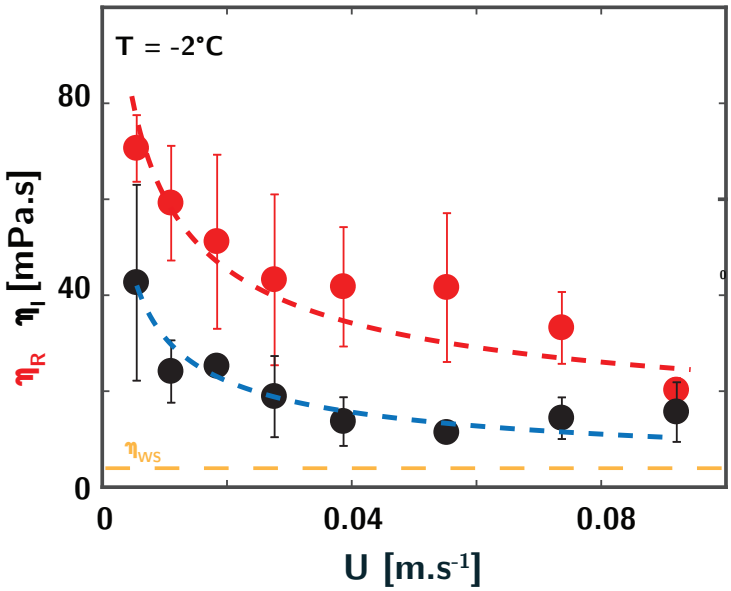

Figure 4.12: Evolution of the real and imaginary part of the viscosity as a function of the shearing speed. The dashed lines correspond to a fit $\eta_{R,I} \propto U^{-\alpha}$ with $\alpha = 0.5$.

Moreover, η_{R} is found to increase tremendously towards the melting point and reaches a value close to two orders of magnitude higher than water at 0°C (Fig.4.13-A). On the other hand, the imaginary (elastic) part η_I is found to be less sensitive to temperature, but the corresponding elastic modulus G', $G' = 2\pi f_{\mathrm{N}}\, \eta_{\mathrm{I}}$ typically lies in the range of 10^2 Pa (4.13-B), stressing the strong elastic response of the film.

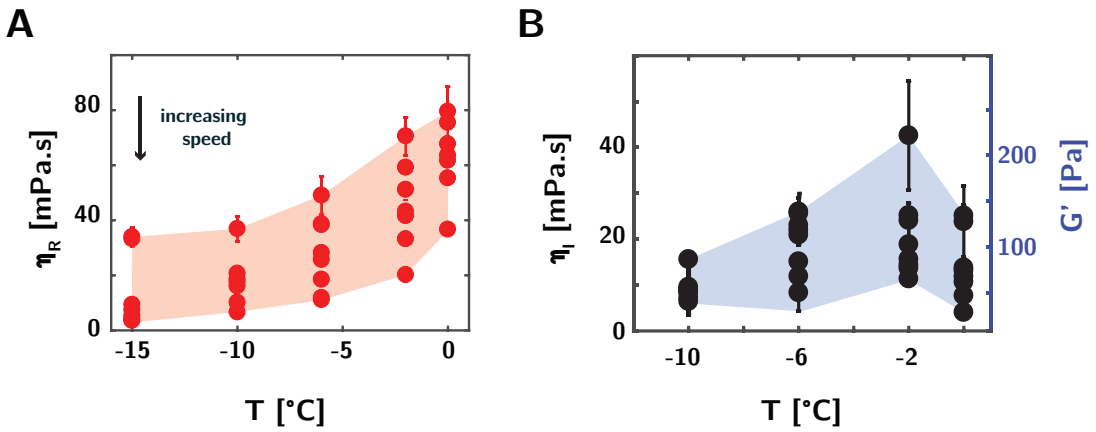

Figure 4.13: **(A)** Evolution of the real part of the viscosity (dissipation) as a function of temperature: we observe a steady increase towards the melting point, reminiscent of the friction force trend. **(B)** Imaginary (elastic) part of the viscosity of the interstitial fluid as a function of temperature. The right axis of panel (B) provides the corresponding elastic modulus G'.

Finally, we observe that the viscosity η_R increases linearly with the load (Fig.4.14 A-B). All these observations underlines the strong link between the friction force and the viscosity dependence (same power law with U, same increase with T, same linearity with the load).

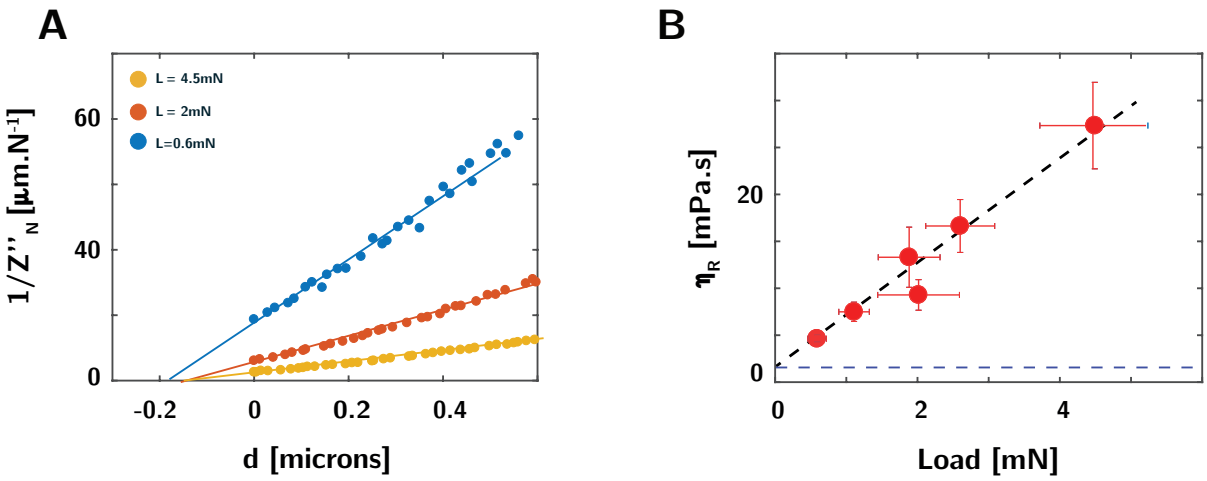

Figure 4.14: **(A)** Retract curves for different regulating loads: we observe a change in the slope rather than in the confinement distance with the regulating load. **(B)** Variations of η_R as a function of the regulating load, the change in friction increase is rather related to a change in the local dissipative viscosity than in a change in the confinement. The blue dashed line in (D) corresponds to the viscosity of super cooled water at -6°C. The data correspond to measurements done with an hydrophobic sphere.

Altogether, our observations converge to an unexpected complex rheology for the meltwater. A first comment is that the interfacial water film under shear is 'as viscous as an oil', with a viscosity up to two orders of magnitude larger than bare water. This points to an unexpected rationale for the exceptional friction properties of ice, contrasting with the bad lubricant behavior of bare liquid water. Indeed a viscous film is a prerequisite to properly lubricate the contact: it limits squeeze-out, thereby avoiding direct solid-on-solid contact. In contrast to standard water, the 'slimy melt water' which is generated under sliding is an excellent lubricant. The complex rheology of meltwater has been completely overlooked up to now in the modeling of ice friction. The latter usually assumes bare newtonian water and focuses on the interplay between frictional heating and the thickness of the meltwater film. Our findings suggest to reconsider the standard framework for ice friction, as well as the dissipative mechanisms occuring in the lubricating film.

As a side note, one may remark that the measured values for the elastic impedance $1/Z'_N$ in the stationary state is much larger than estimates for a capillary contribution due to a meniscus : $\gamma R/h_0 \sim 1kN.m^{-1} \ll Z'_{N0}$ with γ a typical surface tension, and moreover with opposite sign. Furthermore the estimated dissipation due to the contact line displacement and meniscus dissipation would be in the order of few μN, almost two orders of magnitude smaller than the measured friction force. This shows that capillary effects are negligeable.

4.4 Role of hydrophobic coatings

As we stated in the first chapter, a puzzling standard practice in winter sports is to use hydrophobic coatings to reduce friction, typically wax containing fluor additives [115]. However, adding hydrophobic coatings to favor water lubrication may seem counterintuitive and the very origin of this behavior remains mysterious. To this end, we have investigated the friction properties of hydrophobic silanized silica beads.
In this experiment, the sliders differ from the previous glass spheres only by a nanometric silane layer coated on the surface of the bead. Borosilicate beads were silanized following the protocol described in [116]. We measured the advancing and receding contact angles by the dynamic sessile drop method. On bare glass, we found $\theta_A = 55°$and $\theta_R = 42°$for the advancing and receding contact angle respectively (see Fig.4.15-A). On silanized glass, we found θ_A =115°and $\theta_R = 105°$. The low hysteresis for both materials is coherent with the high smoothness of the surfaces.

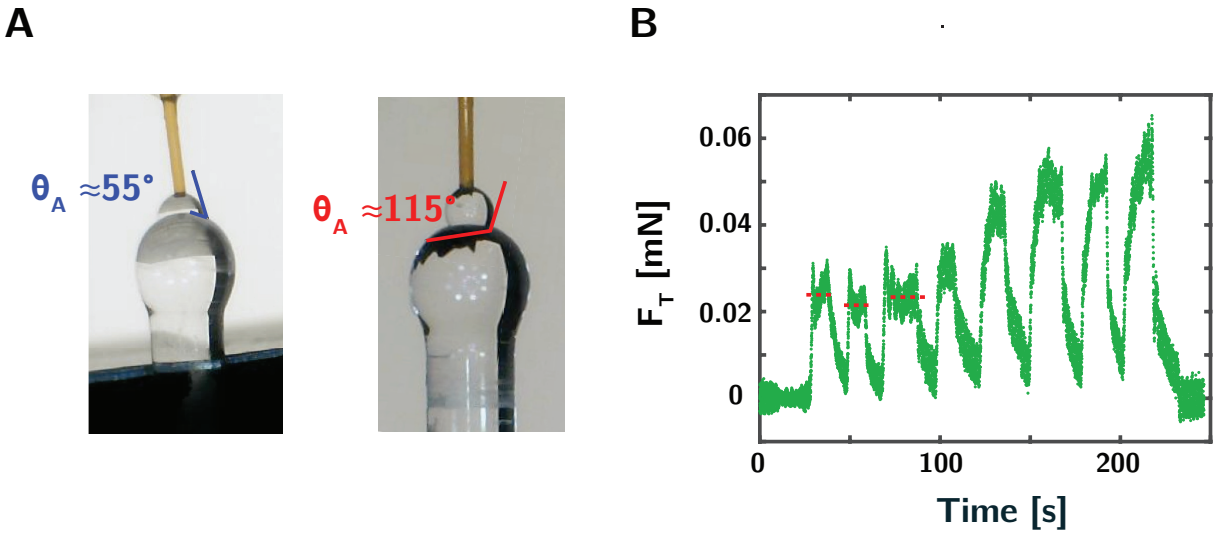

Figure 4.15: **(A)** Measurement of the advancing contact angle for the hydrophilic and hydrophobic glass. **(B)** Ageing of the friction force a the same spot for an hydrophobic bead.

A first remark concerns the ageing of the interfacial properties: while we did not observe any time-dependant evolution for the bare glass, with the silanized beads, we observe that the steady state friction force starts to increase after a few approach-retracts at the same spot (see Fig.4.15-B). Therefore, we only considered the very first measurements done at each spot in the following.

A second remark concerns the fact that, as highlighted in Fig.4.16, the hydrophobic treatment leads to a drastic reduction of friction, as much as a factor 10, as compared to standard glass surface. The friction reduction becomes stronger close to the melting point, in agreement with observations for the effect of wax on snow friction [115].

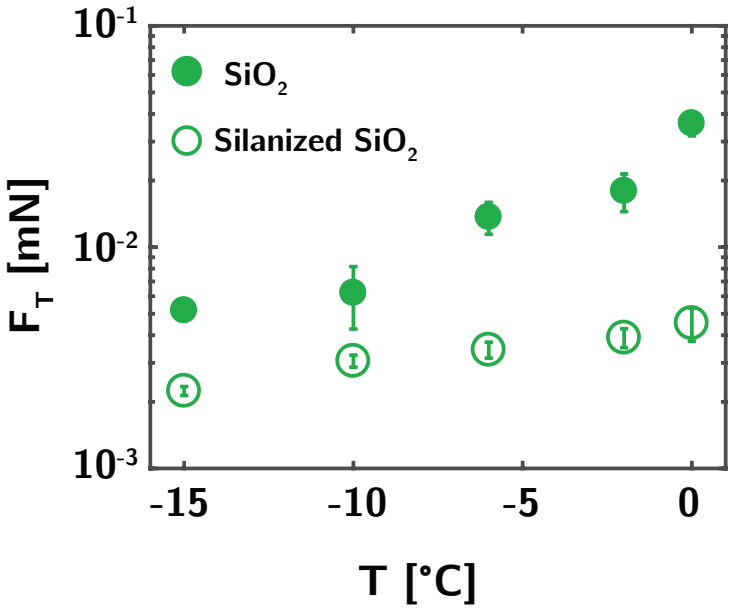

Figure 4.16: Comparison of the friction force for a silanized sphere and bare glass for $U = 2.8\text{cm.s}^{-1}$ as a function of temperature. We measure a drastic reduction of friction for the hydrophobic glass sphere.

To get more insights into the dissipative mechanism at stake, we plot in Fig.4.17-A,B the respective film thickness and viscosity η_R for the hydrophobic and hydrophilic sliders. Our measurements highlight that this friction reduction is not associated with a modified hydrodynamic film thickness h_0 (Fig. 4.17-A). On the one hand, this is somehow surprising since it excludes *a priori* the effect of a finite hydrodynamic slippage at the surface, which may occur for complex fluids [117, 113]. On the other hand, it is an additional proof that the hydrodynamic thickness that we measure is not affected by any slip effect even in the case of bare glass.

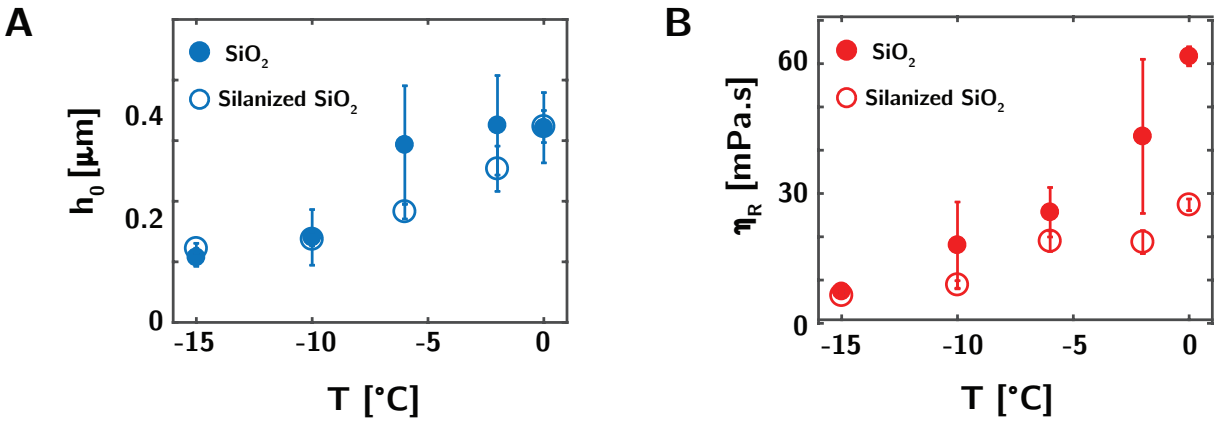

Figure 4.17: **(A)** Comparison of the film thicknesses between the hydrophilic and hydrophobic coatings, showing similar results. **(B)** Comparison of the dissipative part of the viscosity: at high temperatures, the hydrophobic coating highlights a lower viscosity η_R, in line with the observed reduced friction. The effect is reduced at lower temperatures.

Rather, we observe a clear reduction in the real part of the viscosity for the hydrophobic glass as compared to the hydrophilic case. This effect is amplified as the temperature approaches the melting point (Fig. 4.17-B). The trend is also qualitatively the same as for the friction force. The relationship between the viscosity of the interstitial medium and the surface properties suggests that hydrophobicity may affect the melting process under shear leading to a change in the size or density of the suspending debris. Altogether, these findings show that surface effects *at the nanometric scale* can have remarkable implications for macroscopic ice friction. We note that in winter sports, wax coatings are not only hydrophobic, but their composition is chosen such that its hardness adjusts the ski sole to that of the snow/ice grains: this suggests a specific interplay beween elasticity, wear and hydrodynamic properties, in line with our findings. However, snow is a much more complex material than ice (porous material with a mixture of soft snow, hard ice and water). Hence, while our results shed some light on the hydrophobic effects, the specific interplay beween elasticity, wear and hydrodynamic properties at stake in snow remains to be further investigated.

4.5 Discussion: yield stress and suspensions

To summarize, these results reveal interesting similarities between ice and PEG 1000. In both cases, a finite friction force is measured in the limit U$\rightarrow$ 0, *i.e.* a yielding behavior of the interstitial film with a threshold force (or stress) to induce flow. Furthermore, the rheological response of the interstitial film under lateral shear exhibits a hydrodynamic-like response in the tested velocity range. Overall the film response is intermediate between that of a pure solid and a pure liquid, with a yielding behavior and shear-induced fluidization. This behavior bares similarities with solid-on-solid friction where the interstitial joint is shown to exhibit the phenomenology of soft glasses [118]. In a different context, this also echoes closely the observation for fluidization of granular materials which is induced by an independent flow agitation and results in an effective viscosity of the (otherwise yielding) material [119]. The emerging picture is in contrast with the existing literature on ice friction, which assumes a straight transition from a cristalline phase to the bare liquid water phase. But it is consistent with the fact that shear can not lead to a full liquefaction of the contact since this would require a very strong temperature increase in the contact, which is not observed experimentally, see Fig.4.18B-C and Refs.[9, 120]. The recent experiments of Ref.[120], reporting microscale infra-red thermography and optical measurements of snow-grain contacts, actually highlighted abrasion, rather than melting, of the interstitial contact region. The very nature of this intermediate phase remains however to be characterized.

A tempting explanation for the observed response would be that, under abrasive wear, a suspension of liquid and sub-micron (ice or PEG) debris is formed, hence resulting in composite lubrication in the contact. Lateral shear is expected to fluidize the {solid-liquid} mixture within the interstitial layer, again similar to [119], and the interstitial material should exhibit a complex rheology typical of dense suspensions [121], except that here the grains constituting the suspensions should self-adjust under the imposed shear, load and temperature. For a suspension, the viscosity diverges with the volume fraction ϕ as $\eta \sim \eta_0 \left(\frac{1}{\phi_m - \phi}\right)^2$, where ϕ_m is the maximal volume fraction (typically $\phi_m \sim$0.58). Hence,

the measured increase in the local viscosity would correspond to a volume fraction of 70-90% of ϕ_m [121]. Also, higher normal loads may lead to higher indentations and abrasions, providing more debris and higher viscosities. As a matter of fact, the viscosity extrapolated at vanishing load, obtained from the linear variation of the viscosity with the load (Fig.4.14-B), does perfectly match the viscosity of supercooled water at -6°C, suggesting again that the further rise is a direct consequence of the abrasion during the contact. We leave for future works the full structural characterization of the interstitial material under shear, *e.g.* using spectroscopic measurements. This hypothesis also supports the very small increase in the local interfacial temperature.

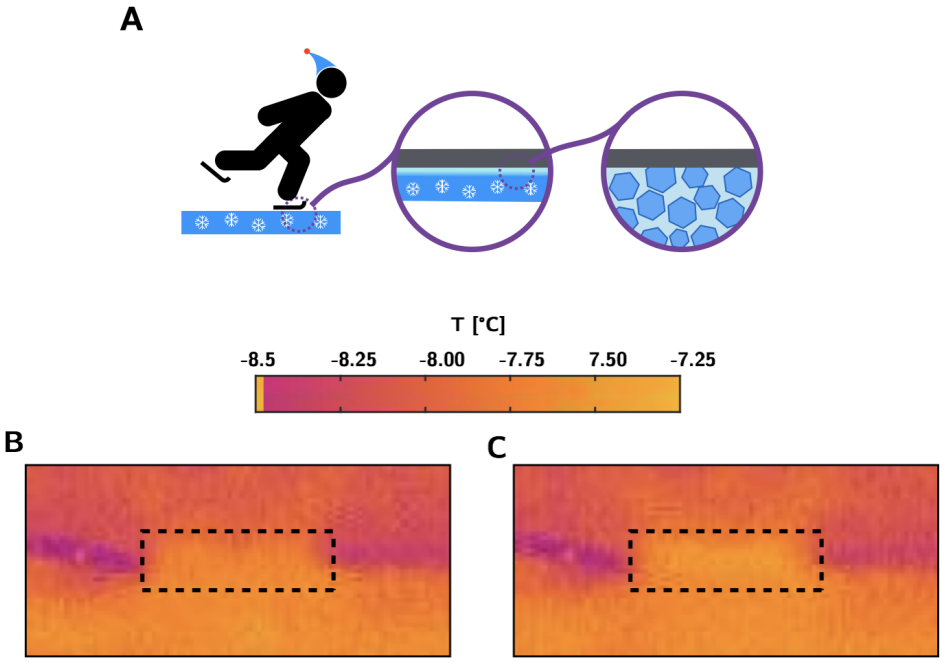

Figure 4.18: **A**. Sketch of the possible mixture of water and ice debris under the skis. **(B-C)** Local heating of the interface when the probe and the ice are in contact respectively without sliding and under sliding.

At this stage, proposing a complete theoretical description for the behavior at stake is of tremendous difficulty because it requires to describe the intertwined relationships between the mechanical, rheological and thermodynamic mechanisms accounting for the generation of the interstitial film, its structure and characteristics. Nonetheless, the observed mechanical properties of the contact provide a guide to revisit the standard framework for ice friction and more generally phase changing materials. In particular, one may obtain some rationale for the surprising independence of the film thickness as a function the tangential speed that we observe both for ice and PEG 1000.

Guided by the experimental observations, one may attempt a simple generalization of the energy balance proposed by Colbeck and others [107], now incorporating the complex rheology and yielding response of the interfacial film. We accordingly rewrite Colbeck's balance between frictional heating and fluid melting as

$$\mathcal{V} \times \sigma(\dot{\gamma}) \times \dot{\gamma} \sim L_f \times \dot{\mathcal{V}}_D \tag{4.2}$$

with $\mathcal{V} \sim R^2\, h$ the volume of the interstitial film with thickness h, $\dot{\gamma} \sim \frac{U}{h}$ the shear rate in the film, $\dot{V}_D \sim R\, h\, U$ the volume melting rate; here σ is the shear stress of the interstitial fluid. In contrast to Colbeck's original argument, we do not assume a newtonian behavior but a complex (yielding) rheology for $\sigma(\dot{\gamma})$. Also, in Colbeck [107], L_f is the latent heat of fusion (per unit volume) but, as we pointed out above, we do not expect a full liquefaction of the interstitial fluid, hence L_f would rather correspond here to the latent heat associated with the fusion of a partial fraction of the interstitial volume. An alternative interpretation of this balance, in line with the previous picture of a film composed of ice debris, would account the term in the right-hand-side of Eq.(4.2) for the rate of energy associated with the fragmentation of the corresponding volume under shear. Accordingly L_f would rather be interpreted in terms of a fracture strength, required to break the ice volume into elementary fragments.

Now, the finite friction force at vanishing velocity exhibited by the force measurements corresponds to a yielding behavior with $\sigma \approx \sigma_Y$ for $U \to 0$, with σ_Y a yield stress of the interstitial material. One thus obtains:

$$h \sim \frac{R\sigma_Y}{L_f} \tag{4.3}$$

This revisited balance thus predicts that the film thickness h is *independent* of velocity. This is in contrast to Colbeck's predictions assuming a newtonian interstitial fluid [107], where h is found to scale as a power law with U. This prediction is however in agreement with our experimental observations for ice, see Fig.4.9-A, as well as for the waxy material (PEG 1000), see Fig.3.16.

In terms of orders of magnitude, one expects the yield stress of the (liquefied) interstitial material σ_Y to be much smaller than the volumic latent heat L_f, so that $\epsilon = h/R \sim \sigma_Y/L_f \ll 1$, as observed experimentally. The values measured for the film thickness, Fig.4.10, actually correspond to $\epsilon \sim 10^{-4}$, hence, they suggest a yield stress $\sigma_Y \sim 3$ kPa using the tabulated value for the water latent heat, $L_f \simeq 360$ MPa (or J.m^{-3}). However, as we mentioned above, we do not expect the ice to be fully molten in the interstitial film. Thus, the effective latent heat relevant to such estimates should be substantially smaller

than the bare latent heat of fusion, lowering accordingly the estimated value for the yield stress σ_Y of the interstitial film. Alternatively, turning to the idea of shear-induced wear and debris formation, one would rather use the fracture strength of ice for L_f, *i.e.* typically $L_f \sim 1$ MPa at -10°C [122], retrieving a value for the yield stress $\sigma_Y \sim 10^2$ Pa. We note that this estimate predicts a friction force in the range $F_T \sim R^2\sigma_Y \sim 0.1$ mN, in fair agreement with the experimental observations for the friction force at low velocity, see Fig.4.6. Such value for σ_Y is also close to the measured value for the elastic modulus of the interstitial material in Fig.4.13-B. However, going beyond these rule-of-thumb estimates would necessitate to build a complete modeling of the reactive interface involving wear and debris formation, as well as its complex rheology. We leave this challenging task for future theoretical investigations.

4.6 Conclusion

Thanks to our unique stroke-probe experimental setup, for the first time it has been possible to bridge the gap between the nanoscale and macroscale tribometry of ice, while fully characterizing the ice interface during frictional sliding.

A key outcome of this study is the evidence for a visco-elastic behavior of the interstitial meltwater along with a yielding behavior at low speeds. We speculate that this may be attributed to the generation of a complex suspension of ice debris within the interfacial film. This large viscosity, coupled with an elastic response, yields an excellent hydrodynamic lubricant behaviour, leading in fine to low friction.

Our experiments challenge the existing theories and should motivate a complete reformulation of the frameworks describing ice friction, beginning with the new fundamental insights unveiled here. Our results will also help improve the empirical strategies adopted to reduce ice or snow friction, in particular the use of wax during winter sports competitions.

Chapter 5

Conclusions and outlooks on snow friction

Contents

In this Chapter, we draw the main conclusions from the work of this thesis, and then we provide some perspectives for further studies on snow friction. We present some different frictional mechanisms which could be involved with snow, focusing on frictional processes which could arise from its granular structure and showing how capillary and wetting phenomena may intervene.

5.1 Bridging the gap between macroscale and nanoscale

Throughout the thesis, we have shown the exceptional versatility of the Micromegascope: this instrument allows to perform AFM scans and rheological measurements with unprecedented ease (see Chapter 2, section 2.4). Furthermore, in tribology, detecting and controlling forces in the gap range between the nanoscale and macroscale regimes has so far limited the application of fundamental atomic-scale insights to practical friction and wear control, pushing scientists towards tedious solutions. With the Micromegascope, we have shown that it is now possible to bridge this gap in different tribological contexts (see chapter 3, sections 3.2 and 3.3). This instrument has therefore the potential of enabling an unprecedented amount of new evidence to become available not only for the study of ice, but for tribological studies at large.

5.2 Friction on ice and snow

The objective of this thesis was to advance the understanding of the mechanisms underlying ice and snow slipperiness. We have successfully been able to characterize the interfacial properties of ice during a friction experiment (see Chapter 4) and shown a fundamental new insight: the existence of a visco-elastic film of meltwater, which lubricates the contact. We have shown that the frictional properties are direclty linked to the rheological properties of this liquid (section 4.2 and 4.3). The overall picture of ice behaviour emerging from our measurements differs remarkably from the canonical models of ice friction developed over the last few decades (that indeed lacked experimental control).

More generally, we have shown for two different phase changing materials that the interface response is intermediate between that of a pure solid and a pure liquid, with a yielding behavior and shear-induced fluidization. The new fundamental insights unveiled here strongly challenge previous understanding of this subject, and should provide the foundations for a reformulation of the framework describing friction on phase changing materials .

5.3 Outlooks on snow friction

For snow friction, we have designed a tribometer capable of capturing wax effects, while characterizing the frictional properties of different materials. A complete understanding of the frictional mechanisms at stake is still lacking, because snow friction is even more complex than ice, mixing elements from all scales (grains, slider). For now, we address

some of those additional mechanisms that should be kept in mind when conducting further studies on the composite dynamics of snow friction.

5.3.1 Ploughing friction

Throughout our experiments on ice, we performed tests using a plexiglass under different snow conditions (see chapter 1, section 1.4.2). Since the plexiglass slider is transparent, it is possible to observe what is happening under sliding: we observe that a snow front is created at the top of the slider. The resulting friction is therefore the sum of two contributions:
- at the front of the slider, there is an energy dissipated in rolling and compacting the ice grains over each other. We have stated previously that the friction coefficient due to snow compaction can be estimated as the ratio of the compacted thickness over the effective length (see Chapter 1, section 1.4.2). In fact, the penetration depth strongly depends on the grains size and on the humidity which determines the grains cohesion and the penetration hardness. In some sense, this kind of friction is very similar to the one on wet and dry sands. Indeed, it has been shown that on sand, friction is strongly affected by water content and for a specific water content, friction is minimized. It has also been shown that the water content affects the elastic modulus of sand [123]. This can be explained by the build up of capillary bridges that initially strengthen the sand, thereby yielding a stronger modulus. The subsequent decrease at higher water contents results from the filling up of those bridges leading to smaller Laplace pressures [124]. It has been shown that the hardness behaves similarly although the reason is still not very clear [125].

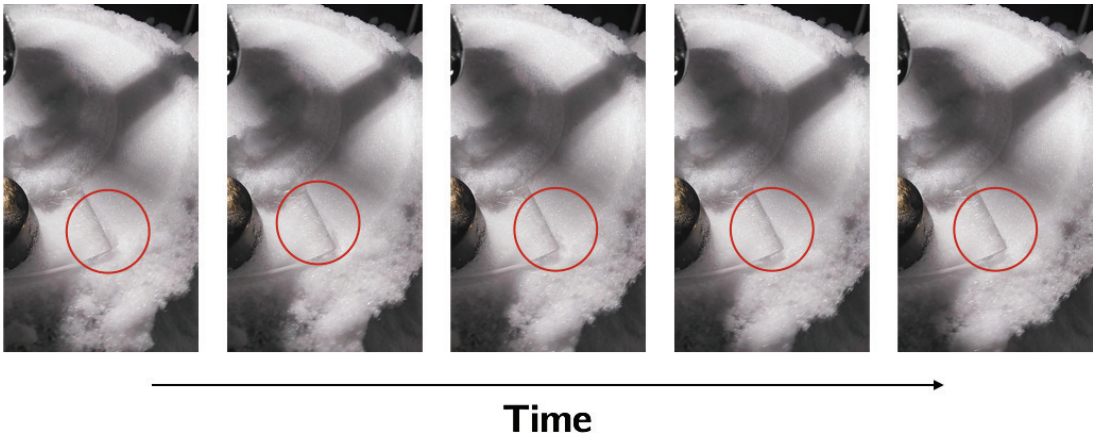

Figure 5.1: Snapshot from

At the back of the slider, to the contrary, friction is probably determined by the local contact between each grain and the slider, and so what we observed for ice may apply.

5.3.2 Capillary adhesion

In the vicinity of the melting point, wetting phenomena should also be taken into account. While the ice is probably wetting for liquid water (hence a null contact angle), we have to

consider the presence of a finite contact angle θ between the water bridge and the slider. For a hydrophilic surface, the liquid meniscus is bent towards the interior ($\theta < 90°$), leading to a negative pressure drop inside the liquid. Therefore, an adhesive force between the slider and the ice grain builds up, leading eventually to an increased friction. For a spherical ice-grain, this force may be calculated as :

$$f_{\text{adh}} = 2\pi\gamma_{LV} r_0(1 + \cos\theta) \tag{5.1}$$

where γ_{LV} is water-vapor surface tension ($\gamma_{LV} \sim 72mJ/m^2$) and r_0 the grain radius [126]. The adhesive force has to be compared to the normal force acting on each contact, which is $f_N = F_N/N_c$ where N_c is the number of contacts. In a first approximation, this number is directly related to the material hardness H, so that $f_N \sim Hro^2$. For a typical grain size $r_0 \sim 100\mu m$ and $H \sim 50kPa$, one finds $f_N \sim 5.8 \cdot 10^{-4}N$ versus $f_{adh} \sim 9 * 10^{-5}N$. This shows that in principle capillary adhesion cannot be negligible and should be taken into account in the friction calculation.

5.3.3 Capillary pumping

Because snow is a granular material, especially at high humidity, water is present among the grains. Therefore, rather than being created by melting, it could be that water is drained to the interface by capillary pumping from the surrounding humid medium.

Imbibition dynamics

To explore the possibility of imbibition dynamics, we made some soaking experiments to observe whether drainage was possible. We used natural snow collected after a snowfall. We pack the snow in a cylindrical tube of length 15 cm and radius R=4 cm. The snow density is constant and equal to $1.5 \cdot 10^3$ kg.m^{-3} (within 20% error). After compacting the snow, we leave it for few hours in a freezer. Then, we put the snow cylinder in contact with a solution of methylene blue kept at 0°C. Because of surface tension, the snow is soaked and we film the liquid rise as shown in Fig.5.2-A. When an equilibrium is reached, we measure again the mass of snow in order to deduce the mass of water absorbed. From that, we retrieve the pore volume fraction. We find extremely high values, between 30 and 40% of the total volume, which suggests that imbibition should not be neglected. As shown in Fig. 5.2 B, the dynamics of the liquid height $h(t)$ is well described by a power-law dependence with time. The exponent 1/2 is reminiscent of a Lucas-Washburn law: $h(t) \sim \sqrt{D_w t}$ with D_w the diffusion coefficient across the porous medium. From the data, we find $D_w \sim 2.10^{-4}$ m^2.s^{-1}. As $D_w \sim \gamma_{LV} d/\eta$, one has access to an estimate of the average pore size d, which we find here to be of the order of the micron. We performed the same experiments with different samples kept either at 0°C or at -18°C. To verify that water was not freezing during the capillary rise, we have also made some experiments with a mixture of water and a refrigerant that freezes at -50°C, but we did not observe any significant difference in the results.

These experiments demonstrate that capillary flows can occur through snow macroscopically. The open question is whether the inherent water inside snow can flow. To demonstrate that this phenomenom may occur, we have performed a simple model-experiment: we use the macroscopic setup described in Chapter 1 with a plexiglass slider,

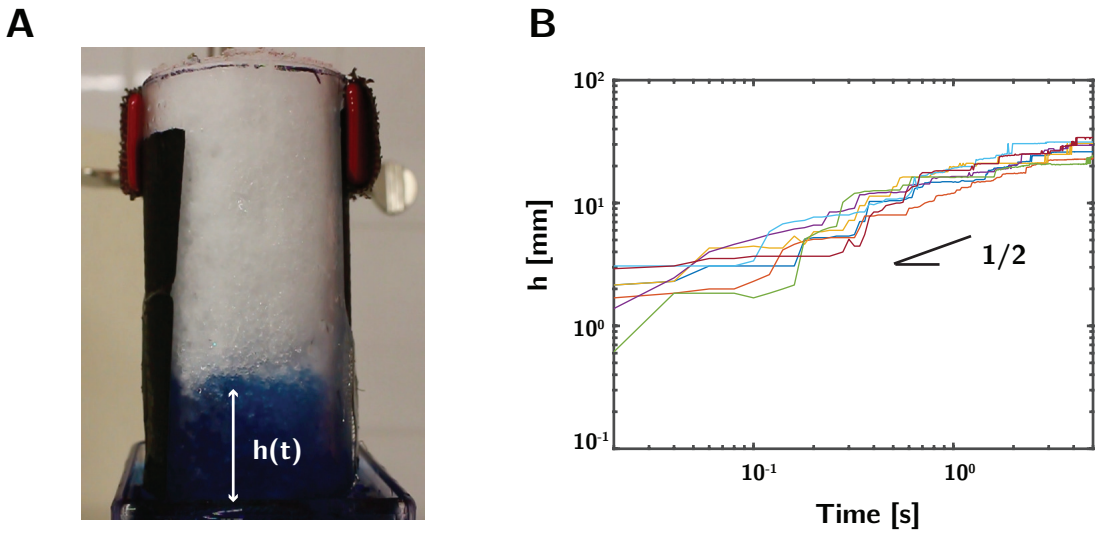

Figure 5.2: **(A)** Snapshot of the experimental set up: a solution of methylene blue is put in contact with a block of snow, leading to a capillary rise. **(B)** Liquid thickness evolution as a function of time at T=0°C.

but we drill a small hole in it. Because PMMA is transparent, we can see the ice interface while sliding. When the hole is empty, we do not observe anything special under the slider. No liquid film can be seen, at least at sight. However, if we fill the hole with snow, we observe that a macroscopic liquid wake forms behind the hole (see snapshots of Fig.5.3). This liquid must come from the snow-ice interaction. At this stage, we cannot conclude directly that it is a reversed capillary drainage or whether ice/snow interface produces additional melting. Although, we may argue that if it were additional melting, it should also be neatly visible in a standard plexiglass on snow experiment. In any case, this basic observation should strongly encourage to push further the drainage experiments with a proper experimental setup that quantifies them thoroughly.

Based on these observations, we may propose some theoretical models which could account for this phenomenon and may serve as a guide for future investigations:
the main idea, sketched in Fig.3, is that the capillary bridges at the interface between the water and the ski create a capillary pressure drop which drains water in this interfacial region. At the interface we expect the vertical extension of a capillary bridge to be fixed by a typical length scale l_c of the interface. The latter can be fixed either by the roughness of the ski coating, or the size of the snow asperities. This is a regime that we would expect for a snow that has a high liquidity content. A Laplace pressure is built, and the water at the interface is at lower pressure as compared to the atmosphere:

$$\Delta P = P_{water} - P_{ext} \sim -\gamma_{LV} \times \frac{1+\cos\theta}{\ell_c} \tag{5.2}$$

where θ is the contact angle between the ski sole and water. This pressure drop will accordingly drive a water flow to the interface.

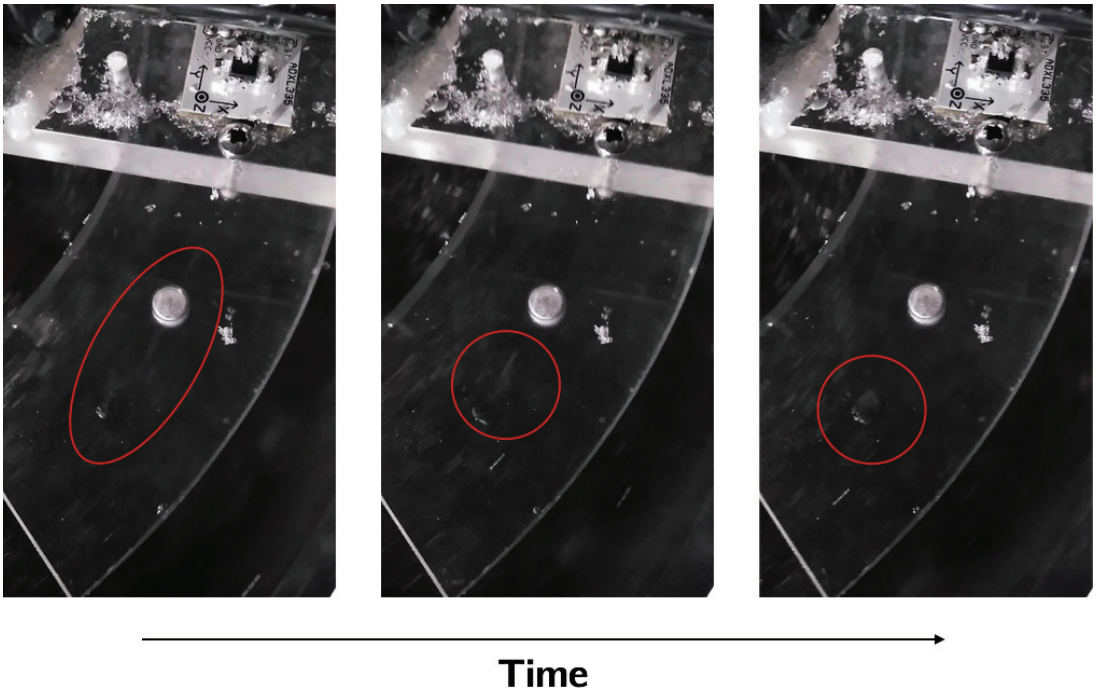

Figure 5.3: Snapshots of the PMMA-ice interface, which evidence the presence of a liquid wake behind the hole filled with snow.

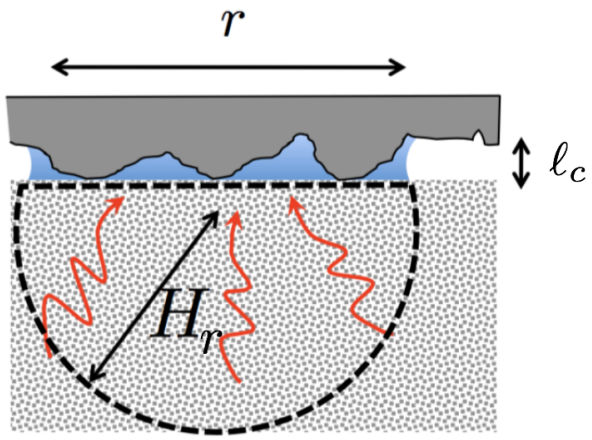

Figure 5.4: Sketch of the capillary drainage

Low velocity regime

At low velocities, we expect that the flow in the snow occurs on a region of similar size to the capillary bridge extension $H_r \sim r$. Then the inward flow is given by:

$$Q_{in} \sim \mathcal{L}_{hyd} \times \frac{-\Delta P}{r} \tag{5.3}$$

where $\mathcal{L}_{hyd}$ is the snow permeability as a porous medium, related to the water viscosity and pore size by: $\mathcal{L}_{hyd} \sim d^4/\eta$ (Poiseuille flow approximation). Simultaneously, there is an outward flux due to the slider dynamics which constantly expells water:

$$Q_{out} \sim \mathcal{A}_{lat} \times U \tag{5.4}$$

where $A_{lat} \sim r \times \ell_R$ is the lateral area of the liquid bridge. Balancing these two fluxes leads to an equation for the lateral extension of the capillary bridge r:

$$r\ell_c \times U \sim \mathcal{L}_{hyd} \times \frac{\left[\gamma_{LV}\frac{1+\cos\theta}{\ell_c}\right]}{r} \tag{5.5}$$

In fact, this relation could also be obtained by considering that the volume of the capillary bridge is controlled by the flux Q_{in} over a typical passage time $t \sim r/U$: $\mathcal{V}_{cap} \sim r^2\ell_R \sim \mathcal{L}_{hyd}(-\Delta P) \times \frac{r}{U}$. For such bridge, the viscous shear force is accordingly:

$$f_{\text{shear}} \sim r^2 \times \eta\frac{U}{\ell_R} \sim \eta\mathcal{L}_{hyd} \times \gamma_{LV}\frac{1+\cos\theta}{\ell_R^3} \tag{5.6}$$

Remarkably, this force is independent of the velocity but also of the water viscosity as $\mathcal{L}_{hyd}$ scales like $1/\eta$. Now, the global shear force is just the force per bridge multiplied by the number of contacts. Following the previous arguments, this number can be fixed by the normal force and the snow hardness by : $N_c \sim F_N/Hr_0^2$ where r_0 is the typical size of an ice grain on snow. Altogether, the friction coefficient would be given by:

$$\mu \approx \frac{\eta\mathcal{L}_{hyd}\gamma_{LV}}{Hr_0^2\ell_c^3} \times (1+\cos\theta) \approx \frac{d^4\gamma_{LV}}{Hr_0^2\ell_c^3} \times (1+\cos\theta) \tag{5.7}$$

This simple model is interesting because it embeds many features of snow friction: first, it yields an apparent solid friction with a friction coefficient independent of speed, as we observed in our measurements. Secondly, it supports the extreme variability of the friction coefficient: indeed, all the parameters involved, are strongly dependent on temperature (snow hardness, and pore/grain sizes) and on the slider (l_c is related to roughness, the contact angle to the coating). It would also explain the magic effect of wax, which both adapts the roughness (hence l_c) and the contact angle. For example, in the case, of standard waxes, a contact angle $\theta \sim$ 110°would yield a decrease in μ of 34%.

High velocity regimes

For high velocities, the stationary state may not be reached during the passage of the slider on the snow. Therefore H_r, which is the size of the drained volume in the reservoir, may be different from r during the filling process. In this case, the capillary bridge with volume $\mathcal{V}_{cap} \sim r^2(t)\ell_c$ would be filled by draining the corresponding volume inside the snow by capillary imbibition, so that $\mathcal{V}_{cap} \sim H_r(t)^3$. This draining process is a non stationary process, driven by:

$$\frac{d\mathcal{V}_{cap}}{dt} = \mathcal{L}_{hyd} \times \frac{-\Delta P}{H_r(t)} \tag{5.8}$$

with $-\Delta P \sim \gamma_{LV} \times \frac{1+\cos\theta}{\ell_c}$ so that we obtain:

$$H_r(t)^4 \sim \left[\mathcal{L}_{hyd} \times \gamma_{LV} \times \frac{1+\cos\theta}{\ell_c}\right] \times t \tag{5.9}$$

This is the imbibition dynamics for a three dimensional spherical interface. The passage time is still $t \sim r/U$. Therefore, equating the volume drained into the capillary bridge to its final volume leads to:

$$H_r^4 \sim \left(r^2\ell_R\right)^{4/3} \sim \left[\mathcal{L}_{hyd} \times \gamma_{LV} \times \frac{1+\cos\theta}{\ell_c}\right] \times \frac{r}{U} \tag{5.10}$$

so that

$$r \sim \left[\mathcal{L}_{hyd} \times \gamma_{LV} \times \frac{1+\cos\theta}{\ell_c}\right]^{3/5} \frac{1}{\ell_c^{4/5}} \times \frac{1}{U^{3/5}} \tag{5.11}$$

Considering that the friction force per bridge is still $f_f = \eta r^2 U/\ell_c$, one gets for the friction coefficient the following expression:

$$\mu \approx \frac{\eta}{H r_0^2 \ell_c^{13/5}} \times \left[\mathcal{L}_{hyd} \times \gamma_{LV} \times \frac{1+\cos\theta}{\ell_c}\right]^{6/5} \times \frac{1}{U^{1/5}} \tag{5.12}$$

This friction coefficient exhibits a weak velocity dependance, which in fact, we also observe sometimes in our data. Again, it is strongly dependent on the snow characteristics.

These models merely serve as guidelines to illustrate that the granular nature of snow may lead to complex friction behaviours. Water transport is entangled with friction properties in a complex and subtle manner. Hence, they are only a first attempt to rationalize capillary effects. What emerges from these models is that they embed all the main snow and slider properties, but they are also extremely sensitive to some underlying assumptions. For instance, how we define the region over which the drainage occurs, strongly impacts the expression of the friction coefficient. Hence, a proper experimental investigation is needed to bring further insights.

5.4 Conclusion

In this Chapter, we have shown that other phenomena can intervene in snow friction because of its granular properties. We have shown that capillary effects could partly be at the root of the macroscopic frictional features observed for snow. The models presented are still at a purely theoretical stage, yet, they incorporate all the key ingredients that seem to be important to reduce friction (hardness, contact angle...). Therefore, the investigative leads suggested from these preliminary observations should be explored in the future, to further unveil the fundamental mechanics of snow friction, with all the useful applications that this would have in a number of fields.

References

[1] Kenneth Holmberg and Ali Erdemir. Influence of tribology on global energy consumption, costs and emissions. *Friction*, 5(3):263–284, 2017.

[2] William Bate Hardy and Ida Doubleday. Boundary lubrication.?the paraffin series. *Proceedings of the Royal Society of London. Series A, Containing Papers of a Mathematical and Physical Character*, 100(707):550–574, 1922.

[3] Duncan Dowson. *History of tribology*. Addison-Wesley Longman Limited, 1979.

[4] Victor F. Petrenko. The effect of static electric fields on ice friction. *Journal of Applied Physics*, 76(2):1216–1219, 1994.

[5] DCB Evans, John Frederick Nye, and KJ Cheeseman. The kinetic friction of ice. *Proceedings of the Royal Society of London. A. Mathematical and Physical Sciences*, 347(1651):493–512, 1976.

[6] Jos J. de Koning, Gert de Groot, and Gerrit Jan van Ingen Schenau. Ice friction during speed skating. *Journal of Biomechanics*, 25(6):565–571, 1992.

[7] Martine Le Berre and Yves Pomeau. Theory of ice-skating. *International Journal of Non-Linear Mechanics*, 75:77–86, 2015.

[8] D. Buhl, M. Fauve, and H. Rhyner. The kinetic friction of polyethylen on snow: The influence of the snow temperature and the load. *Cold Regions Science and Technology*, 33(2-3):133–140, 2001.

[9] L. Bäurle, D. Szabó, M. Fauve, H. Rhyner, and Nicholas D. Spencer. Sliding friction of polyethylene on ice: Tribometer measurements. *Tribology Letters*, 24(1):77–84, 2006.

[10] M. Hasler, K. Schindelwig, B. Mayr, Ch Knoflach, S. Rohm, J. van Putten, and W. Nachbauer. A Novel Ski–Snow Tribometer and its Precision. *Tribology Letters*, 63(3):1–9, 2016.

[11] Anne Marie Kietzig, Savvas G. Hatzikiriakos, and Peter Englezos. Physics of ice friction. *Journal of Applied Physics*, 107(8), 2010.

[12] F. P. Bowden. Friction on Snow and Ice. *Proceedings of the Royal Society A: Mathematical, Physical and Engineering Sciences*, 217(1131):462–478, 1953.

[13] Pekka Oksanen and Juhani Keinonen. The mechanism of friction of ice. *Wear*, 78(3):315–324, 1982.

[14] Bart Weber, Yuki Nagata, Stefania Ketzetzi, Fujie Tang, Wilbert J. Smit, Huib J. Bakker, Ellen H.G. Backus, Mischa Bonn, and Daniel Bonn. Molecular Insight into the Slipperiness of Ice. *Journal of Physical Chemistry Letters*, 9(11):2838–2842, 2018.

[15] B. V. Derjaguin. Mechanical properties of the boundary lubrication layer. *Progress in Surface Science*, 45(1-4):328–336, 1994.

[16] M. Akkok, C. M. McC. Ettles, and S. J. Calabrese. Parameters Affecting the Kinetic Friction of Ice. *Journal of Tribology*, 109(3):552, 2009.

[17] M Faraday. Philos mag. *Philos Mag*, 17(113):162–169, 1859.

[18] J. G. Dash, Haiying Fu, and J. S. Wettlaufer. The premelting of ice and its environmental consequences. *Reports on Progress in Physics*, 58(1):115–167, 1995.

[19] Ben Slater and Angelos Michaelides. Surface premelting of water ice. *Nature Reviews Chemistry*, 2019.

[20] D Frank Ogletree, Charles S Fadley, Hendrik Bluhm, Miquel Salmeron, and Zahid Hussain. The premelting of ice studied with photoelectron spectroscopy. *Journal of Physics: Condensed Matter*, 14(8):L227–L233, 2002.

[21] Astrid Döppenschmidt and Hans Jürgen Butt. Measuring the thickness of the liquid-like layer on ice surfaces with atomic force microscopy. *Langmuir*, 16(16):6709–6714, 2000.

[22] Layer On, T H E Surface, and O N Ice. and D. NASON *. 96:357–363, 1980.

[23] M. M. Conde, C. Vega, and A. Patrykiejew. The thickness of a liquid layer on the free surface of ice as obtained from computer simulation. *Journal of Chemical Physics*, 129(1), 2008.

[24] Ignacio Pickering, Martin Paleico, Yamila A.Perez Sirkin, Damian A. Scherlis, and Matías H. Factorovich. Grand Canonical Investigation of the Quasi Liquid Layer of Ice: Is It Liquid? *Journal of Physical Chemistry B*, 122(18):4880–4890, 2018.

[25] Ken-ichiro Murata, Harutoshi Asakawa, Ken Nagashima, Yoshinori Furukawa, and Gen Sazaki. Thermodynamic origin of surface melting on ice crystals. 2016.

[26] Samuel C Colbeck. Pressure melting and ice skating. *American Journal of Physics*, 63(10):888–890, 1995.

[27] F. P. Bowden and T. P. Hughes. The Mechanism of Sliding on Ice and Snow. *Proceedings of the Royal Society A: Mathematical, Physical and Engineering Sciences*, 172(949):280–298, 1939.

[28] S. C. Colbeck. A Review of the Friction Of Snow. *Physics of Sliding Friction*, pages 275–291, 2013.

[29] L. Bäurle, Th U. Kaempfer, D. Szabó, and N. D. Spencer. Sliding friction of polyethylene on snow and ice: Contact area and modeling. *Cold Regions Science and Technology*, 47(3):276–289, 2007.

[30] Ari J. Tuononen, András Kriston, and Bo Persson. Multiscale physics of rubber-ice friction. *Journal of Chemical Physics*, 145(11), 2016.

[31] W. Ambach and B. Mayr. Ski gliding and water film. *Cold Regions Science and Technology*, 5(1):59–65, 1981.

[32] H. Strausky, J. R. Krenn, A. Leitner, and F. R. Aussenegg. Sliding plastics on ice: Fluorescence spectroscopic studies on interfacial water layers in the μm thickness regime. *Applied Physics B: Lasers and Optics*, 66(5):599–602, 1998.

[33] Brett A. Marmo, Jane R. Blackford, and Chris E. Jeffree. Ice friction, wear features and their dependence on sliding velocity and temperature. *Journal of Glaciology*, 51(174):391–398, 2005.

[34] Maurine Montagnat and Erland M. Schulson. On friction and surface cracking during sliding of ice on ice. *Journal of Glaciology*, 49(166):391–396, 2003.

[35] S. Ducret, H. Zahouani, A. Midol, P. Lanteri, and T. G. Mathia. Friction and abrasive wear of UHWMPE sliding on ice. *Wear*, 258(1-4 SPEC. ISS.):26–31, 2005.

[36] Tristan Baumberger and Christiane Caroli. Solid friction from stick-slip down to pinning and aging. *Advances in Physics*, 55(3-4):279–348, 2006.

[37] Anne Marie Kietzig, Savvas G. Hatzikiriakos, and Peter Englezos. Ice friction: The effects of surface roughness, structure, and hydrophobicity. *Journal of Applied Physics*, 106(2), 2009.

[38] François Cardarelli. *Materials handbook: a concise desktop reference*. Springer Science & Business Media, 2008.

[39] Frank Philip Bowden. tabor d. the friction and lubrication of solids, 1950.

[40] David A Lind and Scott P Sanders. *The physics of skiing: skiing at the triple point*. Springer Science & Business Media, 2013.

[41] Gerd Binnig, Calvin F Quate, and Ch Gerber. Atomic force microscope. *Physical review letters*, 56(9):930, 1986.

[42] Q Zhong, D Inniss, K Kjoller, and V B Elings. Fractured Polymer Silica Fiber Surface Studied By Tapping Mode Atomic-Force Microscopy. *Surface Science*, 290(1-2), 1993.

[43] Y. Martin, C. C. Williams, and H. K. Wickramasinghe. Atomic force microscope-force mapping and profiling on a sub 100-Å scale. *Journal of Applied Physics*, 61(10):4723–4729, 1987.

[44] T R Albrecht, P Grtitter, D Horne, and D Rugar. Frequency modulation detection using highdkantilevers microscope sensitivity for enhanced force. *J. Appl. Phys.*, 69(2):668–673, 1991.

[45] Khaled Karraï and Robert D. Grober. Piezo-electric tuning fork tip-sample distance control for near field optical microscopes. *Ultramicroscopy*, 61(1-4):197–205, 1995.

[46] Joshua D. McGraw, Antoine Niguès, Alexis Chennevière, and Alessandro Siria. Contact Dependence and Velocity Crossover in Friction between Microscopic Solid/Solid Contacts. *Nano Letters*, 17(10):6335–6339, 2017.

[47] M. Labardi and M. Allegrini. Noncontact friction force microscopy based on quartz tuning fork sensors. *Applied Physics Letters*, 89(17):1–4, 2006.

[48] M. Heyde, M. Kulawik, H.-P. Rust, and H.-J. Freund. Double quartz tuning fork sensor for low temperature atomic force and scanning tunneling microscopy. *Review of Scientific Instruments*, 75(7):2446–2450, 2004.

[49] Franz J Giessibl. Atomic resolution on si (111)-(7× 7) by noncontact atomic force microscopy with a force sensor based on a quartz tuning fork. *Applied Physics Letters*, 76(11):1470–1472, 2000.

[50] A. Niguès, A. Siria, and P. Verlot. Dynamical backaction cooling with free electrons. *Nature Communications*, 6:1–7, 2015.

[51] Philippe Poncharal, Z L Wang, Daniel Ugarte, and Walt A De Heer. Full-Text. 283(March):1513–1516, 1999.

[52] Tengfei Miao, Sinchul Yeom, Peng Wang, Brian Standley, and Marc Bockrath. Graphene nanoelectromechanical systems as stochastic-frequency oscillators. *Nano Letters*, 14(6):2982–2987, 2014.

[53] J. Moser, J. Chaste, A. Eichler, R. Rurali, G. Ceballos, and A. Bachtold. A nanomechanical mass sensor with yoctogram resolution. *Nature Nanotechnology*, 7(5):301–304, 2012.

[54] David Tabor and RHS Winterton. The direct measurement of normal and retarded van der waals forces. *Proceedings of the Royal Society of London. A. Mathematical and Physical Sciences*, 312(1511):435–450, 1969.

[55] G. E. Israelachvili, J., Adams. Measurement of Forces between Two Mica Surfaces in Aqueous Electrolyte Solutions in the Range 0-100 nm. *J. Chem. Soc. Faraday Trans. I*, 1977.

[56] J. N. Israelachvili. Thin film studies using multiple-beam interferometry. *Journal of Colloid And Interface Science*, 44(2):259–272, 1973.

[57] Frédéric Restagno, Jérôme Crassous, Élisabeth Charlaix, Cécile Cottin-Bizonne, and Michel Monchanin. A new surface forces apparatus for nanorheology. *Review of Scientific Instruments*, 73(6):2292, 2002.

[58] F. Restagno, J. Crassous, E. Charlaix, and M. Monchanin. A new capacitive sensor for displacement measurement in a surface-force apparatus. *Measurement Science and Technology*, 12(1):16–22, 2001.

[59] P Frantz, N Agrait, and M Salmeron. Use of capacitance to measure surface forces. 1. measuring distance of separation with enhanced spatial and time resolution. *Langmuir*, 12(13):3289–3294, 1996.

[60] M Heuberger. The extended surface forces apparatus. part i. fast spectral correlation interferometry. *Review of Scientific Instruments*, 72(3):1700–1707, 2001.

[61] M Zäch, J Vanicek, and M Heuberger. The extended surface forces apparatus. part iii. high-speed interferometric distance measurement. *Review of scientific instruments*, 74(1):260–266, 2003.

[62] Michelle L. Gee, Patricia M. McGuiggan, Jacob N. Israelachvili, and Andrew M. Homola. Liquid to solidlike transitions of molecularly thin films under shear. *The Journal of Chemical Physics*, 93(3):1895–1906, 1990.

[63] Jacob Klein, Dvora Perahia, and Sharon Warburg. Forces between polymer-bearing surfaces undergoing shear. *Nature*, 352(6331):143–145, 1991.

[64] J. Israelachvili, Y. Min, M. Akbulut, A. Alig, G. Carver, W. Greene, K. Kristiansen, E. Meyer, N. Pesika, K. Rosenberg, and H. Zeng. Recent advances in the surface forces apparatus (SFA) technique. *Reports on Progress in Physics*, 73(3), 2010.

[65] Léo Garcia, Chloé Barraud, Cyril Picard, Jérôme Giraud, Elisabeth Charlaix, and Benjamin Cross. A micro-nano-rheometer for the mechanics of soft matter at interfaces. *Review of Scientific Instruments*, 87(11), 2016.

[66] Alexander M Smith, Kevin RJ Lovelock, and Susan Perkin. Monolayer and bilayer structures in ionic liquids and their mixtures confined to nano-films. *Faraday discussions*, 167:279–292, 2013.

[67] Jean Comtet, Antoine Niguès, Vojtech Kaiser, Benoit Coasne, Lydéric Bocquet, and Alessandro Siria. Nanoscale capillary freezing of ionic liquids confined between metallic interfaces and the role of electronic screening. *Nature Materials*, 16(6):634–639, 2017.

[68] Jean Comtet, Guillaume Chatté, Antoine Niguès, Alessandro Siria, Annie Colin, and Lydéric Bocquet. Pairwise frictional profile between particles determines discontinuous shear thickening transition in non-colloidal suspensions. *Nature Communications*, 8(May):15633, 2017.

[69] Omur E Dagdeviren, Jan Götzen, and Hendrik Hölscher. Robust high-resolution imaging and quantitative force measurement with tuned- oscillator atomic force microscopy. 2016.

[70] Allan J. Melmed. The art and science and other aspects of making sharp tips. *Journal of Vacuum Science & Technology B: Microelectronics and Nanometer Structures*, 9(2):601, 2002.

[71] M. Nowicki, M. Kulawik, H.-J. Freund, T. P. Pearl, P. S. Weiss, G. Thielsch, H.-P. Rust, and L. Cramer. A double lamellae dropoff etching procedure for tungsten tips attached to tuning fork atomic force microscopy/scanning tunneling microscopy sensors. *Review of Scientific Instruments*, 74(2):1027–1030, 2003.

[72] Franz J Giessibl. Advances in atomic force microscopy. *Reviews of modern physics*, 75(July), 2003.

[73] S. Leroy and E. Charlaix. Hydrodynamic interactions for the measurement of thin film elastic properties. *Journal of Fluid Mechanics*, 674:389–407, 2011.

[74] Samuel Leroy, Audrey Steinberger and1 Cecile Cottin-Bizonne, Frederic Restagno, Liliane Leger, and Elisabeth Charlaix. Hydrodynamic Interaction between a Spherical Particle and an Elastic Surface : A Gentle Probe for Soft Thin Films. 264501(June):1–5, 2012.

[75] Antoine Lainé, Laetitia Jubin, Luca Canale, Lydéric Bocquet, Alessandro Siria, Stephen H Donaldson Jr, and Antoine Niguès. MicroMegascope based dynamic surface force apparatus. *Nanotechnology*, 2019.

[76] Bharat Bhushan. Nanotribology and nanomechanics. *Wear*, 259(7-12):1507–1531, 2005.

[77] Bharat Bhushan, Jacob N Israelachvili, and Uzi Landman. Nanotribology: friction, wear and lubrication at the atomic scale. *Nature*, 374(6523):607, 1995.

[78] Robert W Carpick and Miquel Salmeron. Scratching the surface: Fundamental investigations of tribology with atomic force microscopy. *Chemical reviews*, 97(4):1163–1194, 1997.

[79] Martin Dienwiebel, Gertjan S Verhoeven, Namboodiri Pradeep, Joost WM Frenken, Jennifer A Heimberg, and Henny W Zandbergen. Superlubricity of graphite. *Physical review letters*, 92(12):126101, 2004.

[80] Jeong Young Park, DF Ogletree, M Salmeron, Cynthia J Jenks, Patricia A Thiel, J Brenner, and JM Dubois. Friction anisotropy: A unique and intrinsic property of decagonal quasicrystals. *Journal of Materials Research*, 23(5):1488–1493, 2008.

[81] R Bennewitz, T Gyalog, M Guggisberg, M Bammerlin, E Meyer, and H-J Güntherodt. Atomic-scale stick-slip processes on cu (111). *Physical Review B*, 60(16):R11301, 1999.

[82] R Bennewitz, E Gnecco, T Gyalog, and E Meyer. Atomic friction studies on well-defined surfaces. *Tribology letters*, 10(1-2):51–56, 2001.

[83] GA Tomlinson. Cvi. a molecular theory of friction. *The London, Edinburgh, and Dublin philosophical magazine and journal of science*, 7(46):905–939, 1929.

[84] JA Harrison, CT White, RJ Colton, and DW Brenner. Molecular-dynamics simulations of atomic-scale friction of diamond surfaces. *Physical Review B*, 46(15):9700, 1992.

[85] JB Sokoloff. Theory of dynamical friction between idealized sliding surfaces. *Surface Science*, 144(1):267–272, 1984.

[86] NT Garabedian, HS Khare, RW Carpick, and DL Burris. Afm at the macroscale: Methods to fabricate and calibrate probes for millinewton force measurements. *Tribology Letters*, 67(1):21, 2019.

[87] G Amontons. De la resistance causée dans les machines, tant par les frottements des parties qui les composent que par la roideur des cordes qu?on y employe, et la maniére de calculer l?un et l?autre. *Mém. Math. Phys. Hist. Acad. R. Sci.(1699) pp*, pages 206–227.

[88] Izabela Szlufarska, Michael Chandross, and Robert W Carpick. Recent advances in single-asperity nanotribology. *Journal of Physics D: Applied Physics*, 41(12):123001, 2008.

[89] Scott S Perry. Scanning probe microscopy measurements of friction. *MRS bulletin*, 29(7):478–483, 2004.

[90] Heinrich Hertz. On the contact of elastic solids. *Z. Reine Angew. Mathematik*, 92:156–171, 1881.

[91] JA Greenwood and JB Pl Williamson. Contact of nominally flat surfaces. *Proceedings of the royal society of London. Series A. Mathematical and physical sciences*, 295(1442):300–319, 1966.

[92] B Weber, T Suhina, T Junge, L Pastewka, AM Brouwer, and D Bonn. Molecular probes reveal deviations from amontons? law in multi-asperity frictional contacts. *Nature communications*, 9(1):888, 2018.

[93] Martin van Hecke. Jamming of soft particles: geometry, mechanics, scaling and isostaticity. *Journal of Physics: Condensed Matter*, 22(3):033101, 2009.

[94] Vanessa Magnanimo, Luigi La Ragione, James T Jenkins, P Wang, and Hernán A Makse. Characterizing the shear and bulk moduli of an idealized granular material. *EPL (Europhysics Letters)*, 81(3):34006, 2008.

[95] Ivana Agnolin and Jean-Noël Roux. Internal states of model isotropic granular packings. iii. elastic properties. *Physical Review E*, 76(6):061304, 2007.

[96] Jacques Duffy. Stress-strain relation and vibrations of a granular medium. *J. Appl. Mech., ASME*, 24:585–593, 1957.

[97] SN Domenico. Elastic properties of unconsolidated porous sand reservoirs. *Geophysics*, 42(7):1339–1368, 1977.

[98] Xiaoping Jia, C Caroli, and B Velicky. Ultrasound propagation in externally stressed granular media. *Physical Review Letters*, 82(9):1863, 1999.

[99] Hernan A Makse, Nicolas Gland, David L Johnson, and Lawrence Schwartz. Granular packings: Nonlinear elasticity, sound propagation, and collective relaxation dynamics. *Physical Review E*, 70(6):061302, 2004.

[100] S Aumaître, RP Behringer, A Cazaubiel, E Clément, Jérôme Crassous, DJ Durian, Eric Falcon, S Fauve, D Fischer, A Garcimartín, et al. An instrument for studying granular media in low-gravity environment. *Review of scientific instruments*, 89(7):075103, 2018.

[101] Bruno Andreotti, Yoël Forterre, and Olivier Pouliquen. *Granular media: between fluid and solid*. Cambridge University Press, 2013.

[102] Hernán A Makse, Nicolas Gland, David L Johnson, and Lawrence M Schwartz. Why effective medium theory fails in granular materials. *Physical Review Letters*, 83(24):5070, 1999.

[103] Lydéric Bocquet and Elisabeth Charlaix. Nanofluidics, from bulk to interfaces. *Chemical Society Reviews*, 39(3):1073–1095, 2010.

[104] Howard A Barnes. A review of the slip (wall depletion) of polymer solutions, emulsions and particle suspensions in viscometers: its cause, character, and cure. *Journal of Non-Newtonian Fluid Mechanics*, 56(3):221–251, 1995.

[105] Jan Vermant, Paula Moldenaers, Joannes Mewis, M Ellis, and R Garritano. Orthogonal superposition measurements using a rheometer equipped with a force rebalanced transducer. *Review of scientific instruments*, 68(11):4090–4096, 1997.

[106] Charles L Hosler, DC Jensen, and Leon Goldshlak. On the aggregation of ice crystals to form snow. *Journal of Meteorology*, 14(5):415–420, 1957.

[107] SC Colbeck. The kinetic friction of snow. *Journal of Glaciology*, 34(116):78–86, 1988.

[108] ME Kornienko, NL Sheiko, OM Kornienko, and T Yu Nikolaienko. Discrete properties of quasiliquid water film in the ice premelting range. 1. temperature dependences of water nanofilm thickness and viscoelastic properties of polycrystalline ice. *Ukrainian journal of physics*, (58):151–162, 2013.

[109] JS Wettlaufer. Impurity effects in the premelting of ice. *Physical Review Letters*, 82(12):2516, 1999.

[110] TH Oosterkamp, T Boudewijn, and JMJ van Leeuwen. Skating on slippery ice. *Europhysics News*, 50(1):28–32, 2019.

[111] Angelos Michaelides and Ben Slater. Melting the ice one layer at a time. *Proceedings of the National Academy of Sciences*, 114(2):195–197, 2017.

[112] Ronald G Larson. The structure and rheology of complex fluids (topics in chemical engineering). *Oxford University Press, New York Oxford*, 86:108, 1999.

[113] Benjamin Cross, Chloé Barraud, Cyril Picard, Liliane Léger, Frédéric Restagno, and Élisabeth Charlaix. Wall slip of complex fluids: Interfacial friction versus slip length. *Physical Review Fluids*, 3(6):062001, 2018.

[114] J Hallett. The temperature dependence of the viscosity of supercooled water. *Proceedings of the Physical Society*, 82(6):1046, 1963.

[115] Frank Philip Bowden. Friction on snow and ice. *Proceedings of the Royal Society of London. Series A. Mathematical and Physical Sciences*, 217(1131):462–478, 1953.

[116] Matthias Lessel, Oliver Bäumchen, Mischa Klos, Hendrik Hähl, Renate Fetzer, Michael Paulus, Ralf Seemann, and Karin Jacobs. Self-assembled silane monolayers: an efficient step-by-step recipe for high-quality, low energy surfaces. *Surface and Interface Analysis*, 47(5):557–564, 2015.

[117] Amandine Cuenca and Hugues Bodiguel. Submicron flow of polymer solutions: Slippage reduction due to confinement. *Physical review letters*, 110(10):108304, 2013.

[118] L Bureau, T Baumberger, and C Caroli. Rheological aging and rejuvenation in solid friction contacts. *The European Physical Journal E*, 8(3):331–337, 2002.

[119] Kiri Nichol and Martin van Hecke. Flow-induced agitations create a granular fluid: Effective viscosity and fluctuations. *Physical Review E*, 85(6):061309, 2012.

[120] James H Lever, Susan Taylor, Arnold J Song, Zoe R Courville, Ross Lieblappen, and Jason C Weale. The mechanics of snow friction as revealed by micro-scale interface observations. *Journal of Glaciology*, 64(243):27–36, 2018.

[121] François Boyer, Élisabeth Guazzelli, and Olivier Pouliquen. Unifying suspension and granular rheology. *Physical Review Letters*, 107(18):188301, 2011.

[122] JJ Petrovic. Review mechanical properties of ice and snow. *Journal of materials science*, 38(1):1–6, 2003.

[123] Abdoulaye Fall, B Weber, M Pakpour, Nicolas Lenoir, N Shahidzadeh, J Fiscina, C Wagner, and Daniel Bonn. Sliding friction on wet and dry sand. *Physical review letters*, 112(17):175502, 2014.

[124] Peder CF Møller and D Bonn. The shear modulus of wet granular matter. *EPL (Europhysics Letters)*, 80(3):38002, 2007.

[125] RW Liefferink, B Weber, and D Bonn. Ploughing friction on wet and dry sand. *Physical Review E*, 98(5):052903, 2018.

[126] Lydéric Bocquet. Friction : an introduction , with emphasis on some implications in winter sports. pages 1–10, 2013.

Annexe A: Additional methods on the stroke probe technique and the data analysis

In this annexe, we review a number of different checks on the experimental method (stroke-probe technique) and on the analysis of the data from the ice experiment.

5.4.1 Independence of the tangential and normal mode

In order to probe both the normal and tangential mechanical impedances, it is important to verify that the two modes are completely decoupled. The first check consists in increasing the amplitude of one mode and verify that it does not influence the force necessary to keep the amplitude of the other mode constant. In Fig. 5.5, we show that indeed, when the amplitude of the normal mode increases by a factor 20, no visible effect is seen on the tangential amplitude. Note that we chose for a_N and a_T an amplitude range that is in line with the amplitudes involved in the ice friction experiments.

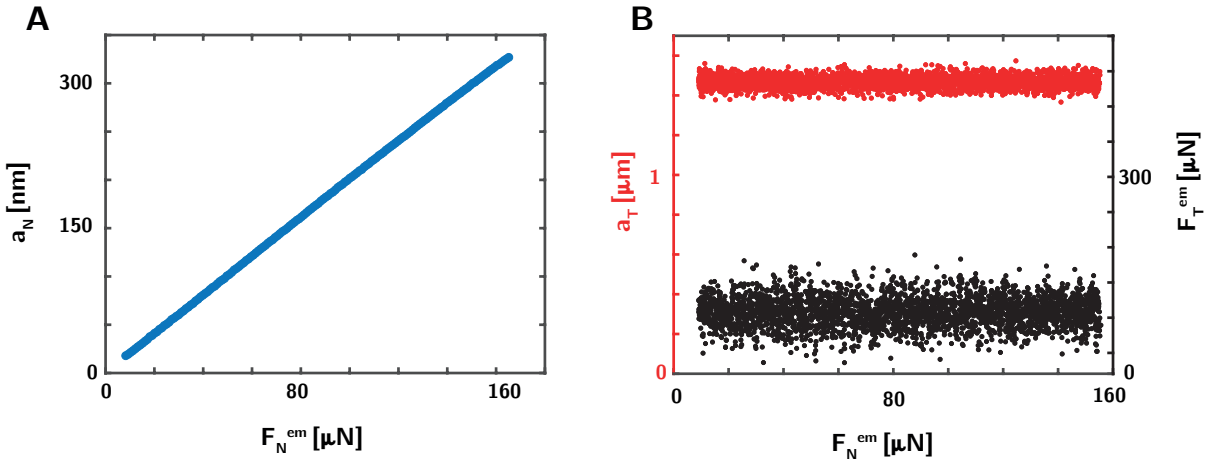

Figure 5.5: **(A)** Linear relation between the normal forcing and the corresponding normal oscillation a_N. **(B)** No effect of the increasing normal forcing and oscillation on the tangential mode is observed.

5.4.2 Analysis of the data from the ice experiment

Dependence on the normal amplitude

We verified that the normal mode oscillation does not influence the tangential mode and the friction measurement (Fig.5.6 A-B) and that the interfacial mechanical properties do not depend upon the normal oscillation amplitude. As shown below in Fig.5.6-C,D, when doubling the normal amplitude, we recover a difference in thickness (50nm) below the experimental error and a difference in viscosity (slope) of the order of 5%.

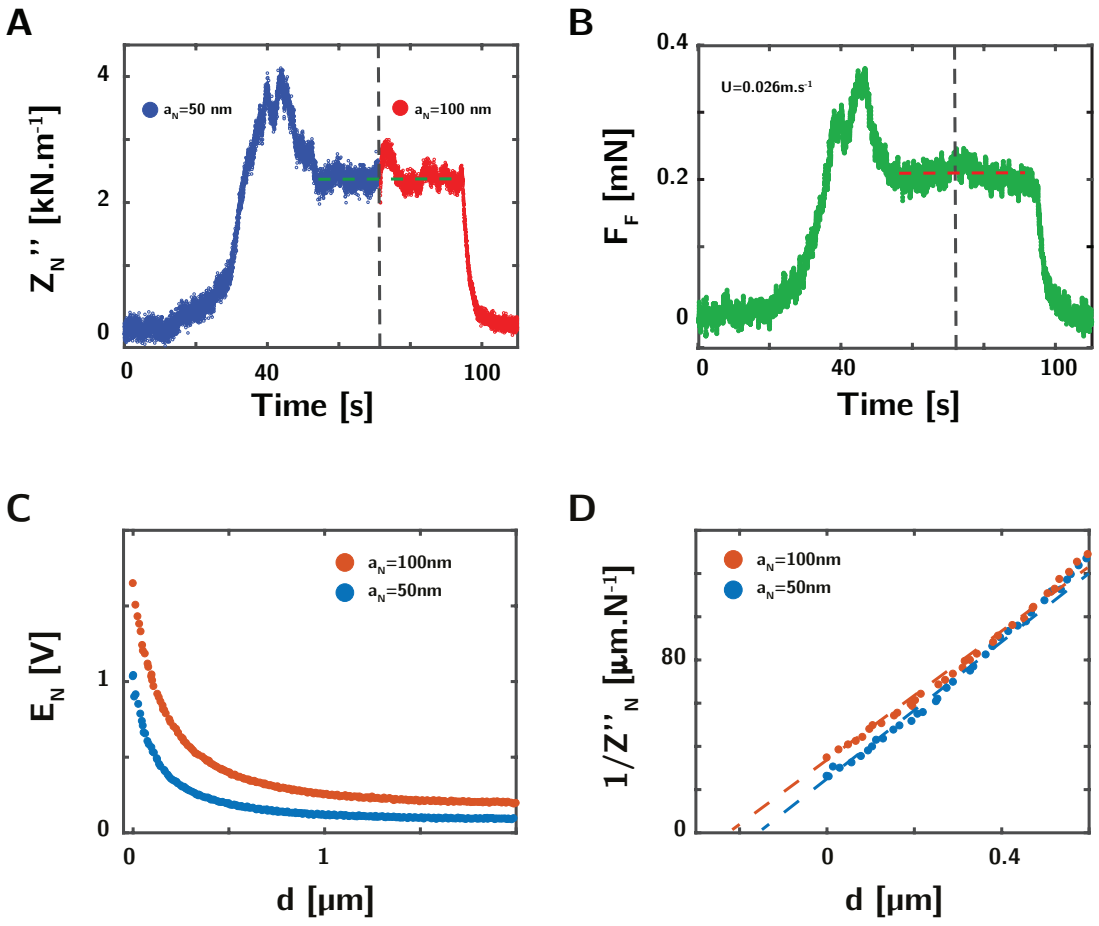

Figure 5.6: Evolution over an approach-retract of the normal dissipative impedance Z''_{N} **(A)** and tangential dissipative force F_{F}.**(B)**. When changing the normal oscillation amplitude from $a_{\mathrm{N}} = 50$ nm to $a_{\mathrm{N}} = 100$ nm, no change in the values of **(A)** normal impedance Z''_{N} nor **(B)** tangential friction force F_{F} is observed.**(C)-(D)**: Raw curves for two consecutive retracts at two different normal amplitudes a_N **(C)** and inverse of the normal dissipative impedance **(D)**.

Deviations from the linear regime during the retract

Only far from the contact (large d) a small deviation from this linear behavior can be observed. As shown in Fig.5.7-A,B, the linear regime is valid in the red region which corresponds to strong normal dissipations and strong normal interactions. As soon as the normal interaction vanishes, we observe an underdissipation as compared to what expected from the hydrodynamic fit. Against this background, one may be interested in understanding whether these viscosity dependences come from this nonlinearity. If we had a universal non linear curve which only depends on the indentation, then the viscosity variations may come from the fact that we would be taking the slope at different points of the same curve. However, this deviation is not universal: it depends on the previous steady state. As shown in Fig.5.7-C,D, when retracting from different steady state values of Z'_{N0}, we obtain different curves that cannot be superimposed. This means that we are not measuring the slope of the same universal curve at different points, but rather that the mechanical properties of the interface change with the imposed load.

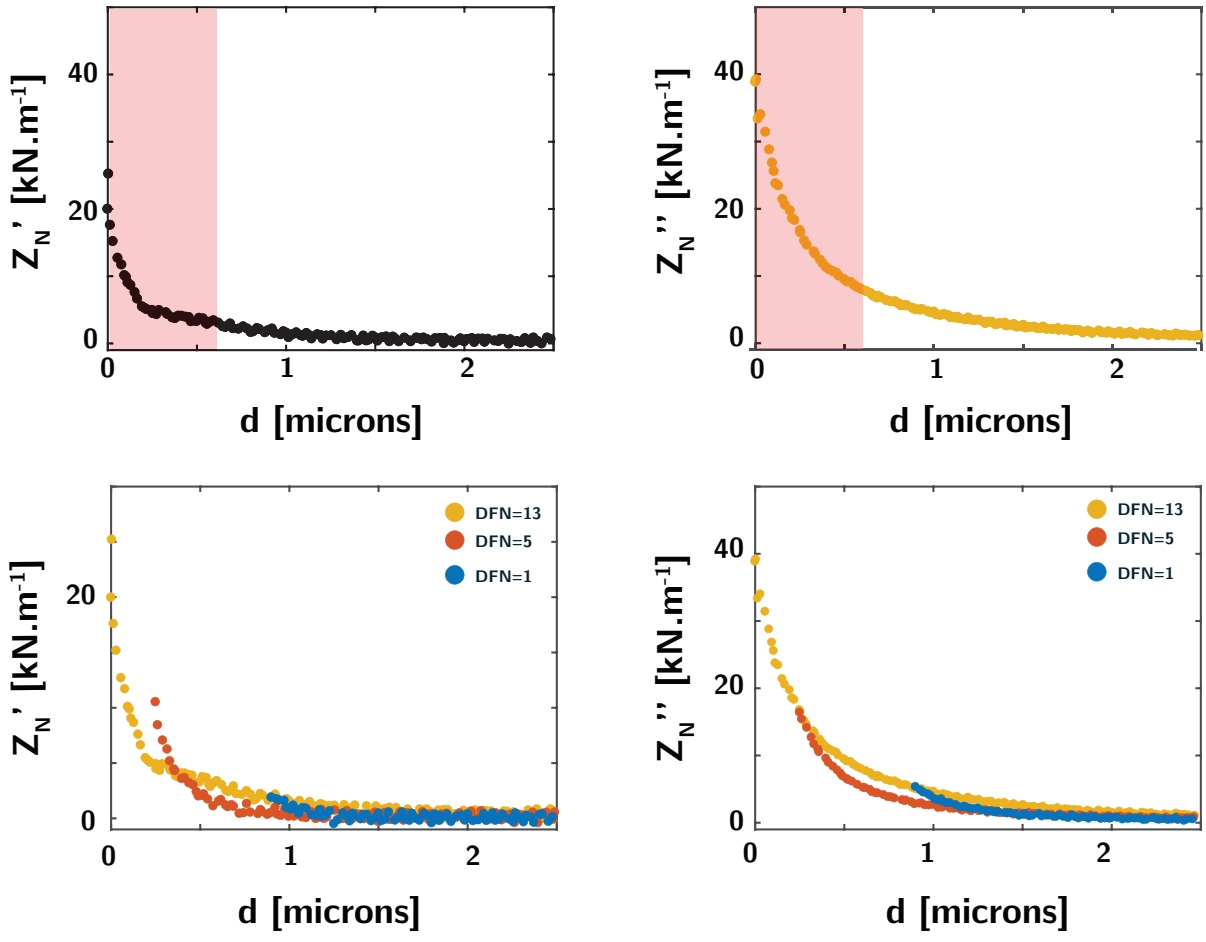

Figure 5.7: Region of validity (red) of the hydrodynamic fit for the normal elastic **(A)** and dissipative **(B)** impedance. This region corresponds to strong normal dissipations and strong normal interactions (**A**). As soon as the normal interaction vanishes, we observe an underdissipation as compared as to what expected from the hydrodynamic fit. **(C)-(D)** Retract curves from different regulating normal loads.

Retract speed

Another important check to perform is whether the local properties are independent from the retract speed. We observe that if the speed is too slow (typically below 300nm.s^{-1}), we obtain rough variations of the normal mechanical impedance Z''_N during the retract (Fig. 5.8A-B). The measurements are not reproducible and it is not possible to extract any rheological property. The most likely explanation for this is that if we retract too slowly the sytem evolves while we are retracting. Therefore, it is not possible to retrieve the properties of the interface during the steady state. Indeed, if the retract speed is above 300nm.s^{-1}, we obtain a smooth curve for the normal mechanical impedance that is independent of the retract speed (Fig. 5.9), which justifies that the measured properties are only inherent to the steady state.

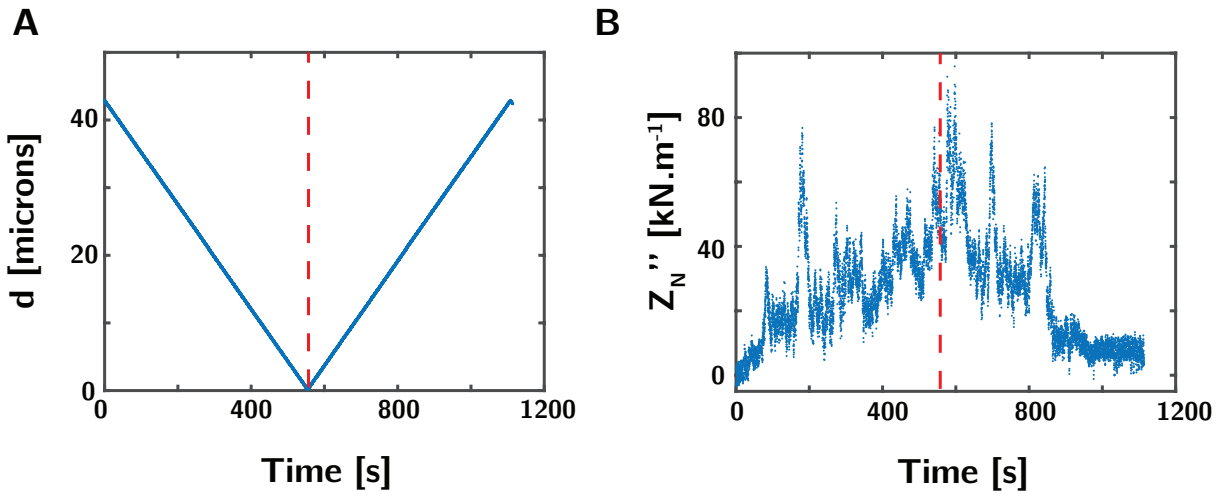

Figure 5.8: Time series for the indentation **(A)** and the normal dissipative mechanical impedance Z''_N **(B)** during an approach retract performed at a slow speed (70nm.s^{-1}).

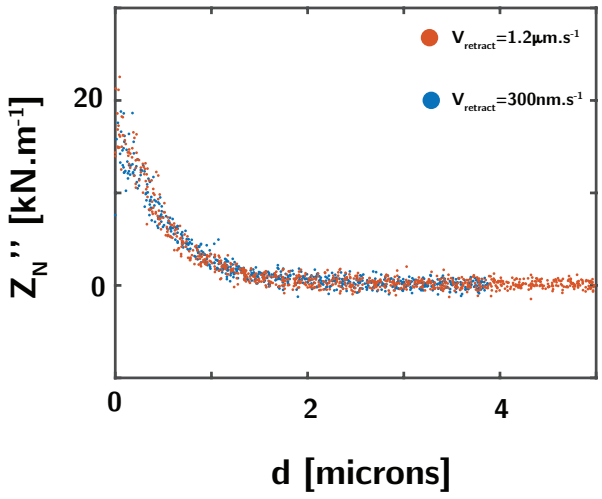

Figure 5.9: Normal dissipative mechanical impedance variation during the retract phase for two retract speeds above 300nm.s^{-1}.

Annexe B: Some investigations on the wetting properties of wax

To guarantee a good slip in cross-country skiing, it is essential to wax the sole of the skis. Without this treatment, according to professional skiers, the snow accumulates under the skis, creating heaps, and thereby strongly decreasing performance. Yet, the way in which these waxes yield this effect is not well understood. In this section, we study the wetting properties of waxes. We focus in particular on gliding waxes from the brand HWK. First, we study the general wetting properties of these waxes and their effect on the wetting properties of the sole, in particular looking at how they affect the advancing and receding contact angles and the hysteresis. Then, we try to quantify the wax stability over time and under shear.

5.5 Contact angle measurements

The contact angle is the angle where a liquid vapor interface meets a solid surface. It is determined by the Young-Dupre equation:

$$cos\theta = \frac{\gamma_{SV} - \gamma_{SL}}{\gamma_{LV}} \tag{5.13}$$

where each γ_{AB} is the interfacial energy between the phase A and B. The measurement of the contact angle allows to quantify the affinity of the liquid with the surface with respect to the affinity between the solid and a gas (air in general). An hydrophilic surface is completely wetted by water (θ =0°), while an hydrophobic one has a contact angle above 90°. Because surfaces are not perfectly smooth, and have defects (physical or chemical), the contact angle is not unique. Nonetheless, it varies between two extreme values: the advancing and receding angle. The advancing angle θ_A is the maximal angle that a drop takes before its surface moves on the substrate, while the receding contact angle θ_R is the minimal angle taken by the interface before moving. In practice, to measure these angles, we inject water into a drop via a syringe: the drop swells and the contact angle increases, then for a critical contact angle, the drop interface moves and that corresponds to the advancing angle. To measure the receding one, we suck water from a drop and measure the critical angle for which the interface moves. The difference $\theta_A - \theta_R$ is called the contact angle hysteresis and is directly related to the static friction force exerted by the liquid $F_T = \pi R_c \gamma_{LV} \left(cos\theta_R - cos\theta_A\right)$ when the drop moves.

Figure 5.10: **(A)** Ski sole with the different tested waxes. **(B)** Contact angle measurement.

5.5.1 First observations

In order to quantify the wax effect, we measure the advancing and receding contact angle on the ski sole throughout the waxing process: indeed, to wax the sole properly, we first melt it and deposit it on the sole and then, scratch it repeatedly with a plastic scraper and a metallic brush. We tested four different waxes:

- LFW2 for hot temperatures (-8 to 2°C)
- A1 Allround: universal paraffin wax for all types of snow.
- Racing-LF: -10°C to 10°C wax for all temperatures and humidities
- SP7 Polar: special glide wax for extremely cold and dry conditions (-30°C to -8 °C)

The results are shown in Fig.5.11:
the first striking result is that depositing the wax on the ski sole, increases notably both the advancing and receding contact angle (Fig. 5.11-A). Therefore where there is wax the average contact angle is higher, which leads in general to less adhesion, and can be important in understanding the possible mechanisms hypotesized in Chapter 5.
The second interesting result is that when we put the wax, we reduce the hysteresis, but at the same time the brushing leads to an increase of the hysteresis which is basically the same as for the bare ski sole. This can be interepreted as an effect of the increased roughness due to brushing. Indeed, when the wax is deposited, it covers completely the ski sole yielding to a smooth surface, whereas the further brushing exposes a much rougher surface. The Wenzel equation links the advancing and receding contact angles on a rough surface to the ones on the same smooth surface. If r is the ratio between the real surface and the apparent surface, then the measured contact angle on a rough surface is:

$$cos\theta^* = r \cdot cos\theta \tag{5.14}$$

Since $r > 1$, when $\theta < 90$°C, $\theta^* < \theta$ while the opposite occurs for $\theta > 90$. Hence, roughness tends to increase the advancing contact angle and decrease the receding contact angle,

leading to a higher hysteresis. This might be surprising at first since we would expect that wax would decrease the hysteresis to create smaller static friction force. In fact, one should also take into account that here, we measure macroscopic contacts, while when the ski slides on snow, the contacts are much smaller, and indeed, locally, we might be in the case where the wax is directly in contact with the liquid film, without any roughness effect.
It should also be noted that we do not observe major differences between the different waxes. One possible explanation is that the measurements are done at room temperature. A second one, is that for these waxes, the differences are more related to their mechanical properties than the wetting ones.

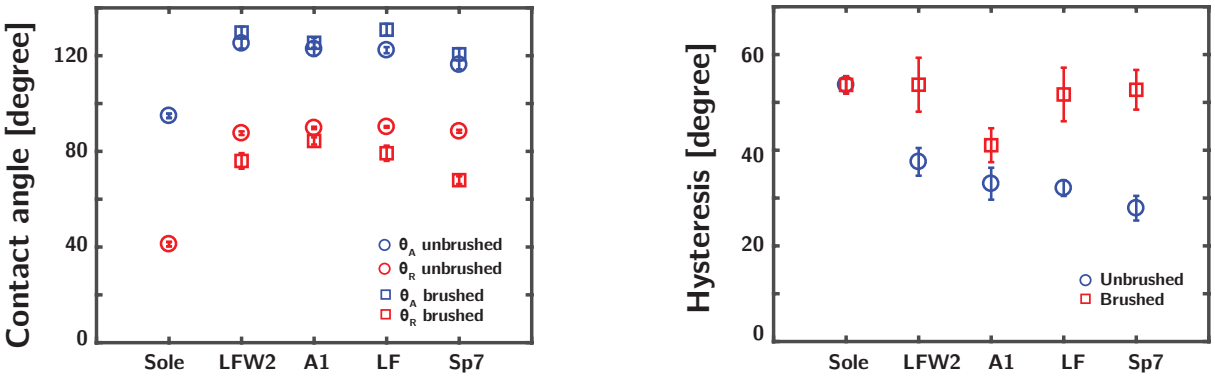

Figure 5.11: **(A)** Advancing and receding contact angle measured for each wax along with the resulting hysteresis **(B)**.

5.5.2 Wax stability

A major question that comes to mind with waxes is their stability over time and under effort: how does wax behaves after several friction episodes? Is wax still present below the ski at the end of a race? In fact, many professional skiers deposit the wax under the ski sole a few hours before a race, but then scratch it away just before the start. They do so under the impression that some kind of release occurs from the depth of the sole towards the exterior, and some time should pass between waxing and the maximal friction decrease. To answer these questions, and understand the effect of wear and of the waiting time, we have carried out two kinds of experiments. The results presented below relate to the A1 allround wax, but similar results were retrieved for the LFW2 wax as well.

Behavior under friction

To test how the hydrophobicity changes after frictional tests, we simulate them by scratching repeatedly the surface either with a plexiglass scraper or a metallic brush. We have tested two waxes (A1 and LFW2). Waxes are deposited in the evening before the tests. The next day, we proceed to a first measurement. Then, we scratch them 10 times in the same direction with the plexiglass scraper and make a measurement. We iterate the same process 5 times. For the metallic brush, we brush typically for 20seconds, make a measurement and iterate again. The results are shown in Figs.5.12-A,B, for the plexiglass scraper and metallic brush respectively. The main insight is that neither the angles nor

the hysteresis varies through the scratchings/brushings. Therefore, the wax seems quite resistent to wear.

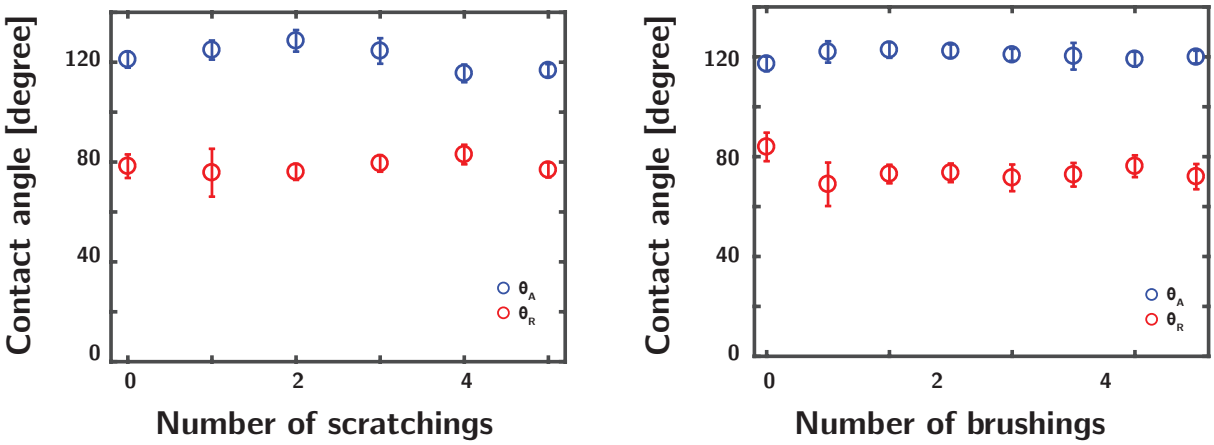

Figure 5.12: Advancing and receding contact angles evolution with the number of scratchings **(A)** and brushings**(B)** for the ax A1 Allround.

Temporal evolution

To account for the temporal evolution, we have adopted the following protocol: we take a sole waxed the evening before and measure the advancing and receding angles at different spots. Then, we scratch it once and measure over time the evolution of the contact angles. At each time step, we make ten measurements at ten different spots. We limit ourselves to a total of 3 hours of experiment, which correponds approximately to the time lapse of a race and also to the typical time that athletes consider between waxing and racing. As shown in Fig.5.13, we do not observe any temporal change.

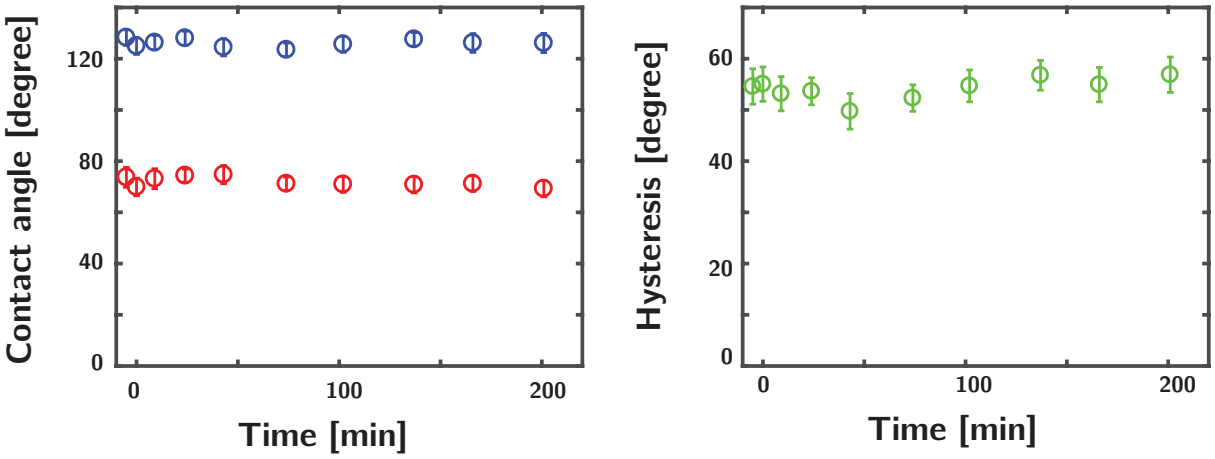

Figure 5.13: Temporal evolution taken at different spots for the contact angles **(A)** and hysteresis **(B)** with the wax A1 allround.

We have also proceeded to a slightly different experiment where we measure the contact angles at a same spot over time, but the results are the same (Fig.5.14).

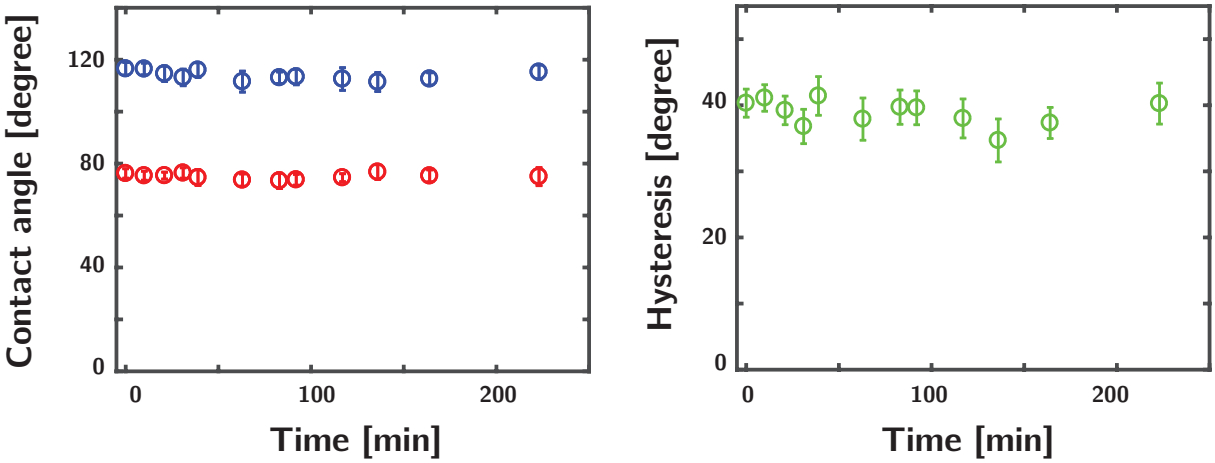

Figure 5.14: Temporal evolution taken at a same spot for the contact angles **(A)** and hysteresis **(B)** with the wax A1 allround.

In light of the experiments, it seems that wax is resistent to wear and abrasion and stable over time. Thus, we should think that it undergoes little change during races. The results seem also to deny the idea that some release occurs over time.

Résumé

Dans ce manuscript, nous présentons une étude expérimentale multi-échelles de la friction sur la glace et la neige. Ces deux matériaux sont connus depuis longtemps pour être extremement glissants. Cependant, le mécanisme physique derrière ce phénomène n'est pas encore compris aujourd'hui.
Dans un premier temps, nous présentons un tribomètre macroscopique qui permet de caractériser précisément le coefficient de friction d'un mobile glissant sur la glace et la neige. Nous montrons, cependant, qu'on ne peut pas inférer directement les propriétés locales du contact à partir de l'observation des propriétés macroscopiques.
Nous introduisons alors un nouvel instrument qui permet des mesures rhéologiques et tribologiques simultanées. Il s'agit d'un diapason macroscopique basé sur le principe de fonctionnement d'un microscope à force atomique.
Nos mesures montrent que le caractère glissant de la glace est du à un film lubrifiant nanométrique, créé sous l'effet du cisaillement. Cependant, ce film n'est pas fait d'eau liquide mais possède un comportement non newtonien: il s'agit d'un fluide à seuil, avec un comportement visco-élastique. Nous montrons que les propriétés tribologiques de la glace sont intimement liées aux propriétés rhéologiques de ce film. Nos mesures remettent donc en question les théories existantes sur la glace et posent les premières bases pour comprendre plus généralement la friction dans les systèmes à transition de phase .

Mots Clés

Microscopie à Force Atomique – Tribologie – Rhéologie – Matière Molle – Nanoscience-Glace-Neige

Abstract

In this manuscript, we present a multiscale experimental study of ice and snow friction. The slipperiness of ice and snow is a common knowledge, but the very mechanism behind this observation has been a fundamental mystery for more than 150 years. Here, we first present a macroscopic tribometer, which allows for a proper characterization of the friction coefficient on ice and snow. However, we show that the experimental macroscopic findings cannot reveal directly the local interfacial properties.
Hence, we introduce a novel instrument, which combines tribological and rheological capabilities with nanoscopic sensitivity. It is a macroscopic tuning fork, based on atomic force microscopy.
Our measurements show that ice slipperiness originates from a nanometric lubricating film due to ice melting under shear. More unexpected is that the interfacial meltwater is far from any "simple water". It has a yielding behavior and a visco-elastic one under flow. The tribological results are intimately related to such properties. Our findings ask for a fundamental overhaul of the existing framework describing ice friction. More generally, it is also a building block for a better understanding of friction mechanisms in phase changing materials.

Keywords

Atomic Force Microscopy – Tribology – Rheology – Soft Matter – Nanoscience-Ice-Snow